

# POLITECNICO DI TORINO

Corso di Laurea Magistrale  
in Ingegneria Civile

Tesi di Laurea Magistrale

COMPOSITE MATERIALS FOR NEW CONSTRUCTION  
SYSTEMS: EXPERIMENTAL AND NUMERICAL  
INVESTIGATIONS.



**Relatore**

prof. Alessandro Pasquale Fantilli

**Correlatore**

prof. Joaquim António Oliveira de Barros

**Candidato**

Daniele Fusi

Anno Accademico 2019/2020

# Abstract

The present thesis intended to contribute for the development of a new generation of high durable and sustainable reinforced concrete (RC) beam structures submitted to flexural loading, by combining the benefits that Glass Fiber Reinforced Polymers (GFRP).

The main benefit given by the GFRP bars is their corrosion immunity. Furthermore, the Fiber Reinforced Concrete (FRC) was developed to improve the ductility of structures and to provide greater shear strength.

One of the advantages of not being attacked by chemicals, is to have the possibility of using a very reduced concrete cover for greater structural functionality.

Although, conventional shear reinforcements were not used, they were totally replaced by FRC material and a new 3D positioning geometry of the GFRP bars allowed to help this resistance, even if it is not considered in the design calculations.

Due to the quite high post-cracking tensile strength and energy absorption capacity that this composite material attained, the system showed adequate bending resisting, and enhancement in the structural performance at serviceability.

The work started with the assessment to behaviour of GFRP and FRC through experimental tests and analytical investigation. The structural performance of this GFRP reinforced FRC was investigated by performing four-point bending tests on beams. Moreover, an extensive analytical formulation was developed in order to theoretically address to the main structural aspect of the tested beams.

The obtained experimental results were captured well using the respective results from the analytical study. Finally, finite element simulations were carried out, using well-known modelling approach available in the literature for elements in form of models.

# Contents

<b>Chapter 1</b> .....	<b>1</b>
1. Introduction .....	1
1.1. General Consideration.....	1
1.2. Objectives.....	2
1.3. Research steps .....	3
<b>Chapter 2</b> .....	<b>4</b>
2. State of the art on composite materials for new construction systems.....	4
2.1. Introduction .....	4
2.2.1. Fiber Reinforced Concrete (FRC) .....	5
2.2.2. Three-Dimensional System Reinforcement Textile (3D-SRT).....	6
2.2. Constitutive laws of FRC in tension .....	8
2.3. Shear resistance of FRC .....	17
<b>Chapter 3</b> .....	<b>23</b>
3. Experimental Program.....	23
3.1. Introduction .....	23
3.2. Tests carried out .....	23
3.2.1. Compression tests. ....	24
3.2.2. Tensile test .....	27
3.2.3. Three-point notched beam bending test (3PNBBT) .....	28
3.2.4. Four-point bending test (4PBT).....	30
3.3. Results .....	33
3.3.1. Compressive strength.....	33
3.3.2. Tensile strength.....	34
3.3.3. Crack patterns and failure modes.....	37
3.3.4. Flexural capacity .....	39

<b>Chapter 4.....</b>	<b>42</b>
4. Analytic Model.....	42
4.1. Model of 3D Timoshenko’s beam.....	42
4.1.1. Linear static analysis model.....	43
4.1.2. Stiffness matrix.....	53
4.1.3. Mass matrix.....	54
4.1.4. Nonlinear static analysis model.....	59
4.2. Software for design the element.....	61
4.2.1. Analysis of cross-sections.....	62
4.2.2. Analysis of the slab.....	66
4.3. Numerical Simulation.....	68
4.3.1. Comparison between numerical model and experimental results.....	68
4.3.2. Comparison between GFRP and steel reinforcement.....	72
<b>Chapter 5.....</b>	<b>76</b>
5. Conclusion.....	76
5.1. General Conclusion.....	76
5.2. Suggestions for future research.....	77
<b>References.....</b>	<b>78</b>

# List of figures

Figure 1 – Structure of a GFRP bar .....	7
Figure 2 - Structure of a manufactured 3D-SRT reinforcement.....	7
Figure 3 - Typical load (P) – deformation ( $\delta$ ) of FRC: a) Tensile strain-softening; b) Tensile strain-hardening [8]. .....	8
Figure 4 - Typical load-CMOD curve of FRC [8] (dimensions in mm). .....	9
Figure 5 - Tensile stress-strain relationship for plain concrete and FRC up to material tensile strength.....	10
Figure 6 - Stress-crack opening constitutive laws for ULS analysis: a) rigid-plastic model; b) linear model [8]. .....	11
Figure 7 - Example of determination of neutral axis position, $x$ , and $y$ for the evaluation of lcs. ....	12
Figure 8 - Stress-strain relationship of a strain softening FRC, for ULS analysis: (a) complete diagram; (b) simplified diagram. ....	14
Figure 9 - Stress-strain relationship for SLS analysis: (a) Case I; (b) Case II; (c) Case III [8]. .....	14
Figure 10 - SLS stress-strain case I model for situation where concrete matrix post-cracking contribution is disregarded.....	16
Figure 11 - Example of SLS stress-strain Case I model where point C is disregarded..	16
Figure 12 - Electric displacement transducers: a) $\pm 12.5$ mm; b) $\pm 2.5$ mm. ....	24
Figure 13 – Specimen for compression test and mechanic press. ....	25
Figure 14 – Dimension of the cylindric specimen and position of LVDTs. ....	25
Figure 15 – Loading in the time during the compression tests for the evaluation of Young’s module. ....	26
Figure 16 – Tensile test for a GFRP bar.....	27
Figure 17 – Schematic representation of position of LVDTs in the 3PNBBT (measures in mm).....	28
Figure 18 - Position of LVDT in a mid-span in the 3PNBBT.....	29
Figure 19 – Position of LVDT between the crack in the 3PNBBT.....	29
Figure 20 – Position of LVDT on the actuator in the 3PNBBT.....	29

Figure 21 - Sizes of the specimen for 4PBT.....	30
Figure 22 – Schematic representation of position of LVDTs in the 4PBT. ....	31
Figure 23 – Position of horizontal LVDT on the slab in the 4PBT.....	31
Figure 24 – Position of LVDT on the actuator.....	31
Figure 25 - Dimensions of textile reinforcement in GFRP: a) Top view; b) Frontal view. .....	32
Figure 26 – Results of compression test of the FRC specimens. ....	33
Figure 27 – Load-Deflection diagram: a) bars of Ø5; b) bars of Ø3.....	35
Figure 28 – Stress-Strain diagram for Ø3 bars in GFRP.....	35
Figure 29 - Stress-Strain diagram for Ø5 bars in GFRP. ....	36
Figure 30 – Diagram Load–crack opening.....	38
Figure 31 – Deflection – CMOD diagram.....	38
Figure 32 – Load-deflection diagram of FPBT. ....	39
Figure 33 - Load-deflection diagram during FPBT supplied by external LVDTs: a) Test n°1; b) Test N°2.....	40
Figure 34 - Load-deflection diagram during FPBT supplied by external LVDTs: a) Test n°3; b) Test N°4.....	41
Figure 35 - Specimens collapsed after 4PBT. ....	41
Figure 36 – Timoshenko beam in the space. ....	43
Figure 37 – Local coordinates. ....	44
Figure 38 - Tensions.....	46
Figure 39 - Stresses in the section of a Timoshenko element. ....	47
Figure 40 - Scheme for obtaining the stiffness matrix of an element [13].....	60
Figure 41 – Scheme for obtaining the internal forces of an element [13]. ....	61
Figure 42 – Simplified cross section of slab for analytic model (measure in mm).....	62
Figure 43 – Model of the constitutive law and post-cracking behaviour of FRC. ....	63
Figure 44 – Model of the constitutive law of GFRP. ....	65
Figure 45 – Static scheme of the beam subjected to 4PBT. ....	66
Figure 46 - Numerical approach to simulate the deformational behaviour of structural elements. [16].....	67
Figure 47 – Numerical simulation of top layer of cross-section (compression negative). .....	68

Figure 48 - Numerical simulation of GFRP bars.....	69
Figure 49 – Moment-Curvature diagram of the cross-section in the numerical model..	69
Figure 50 - Comparison of the numerical model with experimental results of the center beam. ....	70
Figure 51 - Comparison of the numerical model with experimental results of the LVDT 176621.....	70
Figure 52 - Comparison of the numerical model with experimental results of the LVDT 198379.....	71
Figure 53 - Model of the constitutive law of steel.....	72
Figure 54 - Numerical simulation of steel bars: a) 5Ø6; b) 5Ø8.....	73
Figure 55 - Moment-Curvature diagram of the cross-section in the numerical model with steel bars. ....	74
Figure 56 - Comparison of the numerical models, GFRP bars and 5Ø6 steel reinforcement, with experimental results in the mid span of the beam.....	74
Figure 57 - Comparison of the numerical models, GFRP bars and 5Ø8 steel reinforcement, with experimental results in the mid span of the beam.....	75

# List of tables

Table 1 - Value of $kG$ and $\alpha$ depending on prism bending test standard [6].....	21
Table 2 - Description of position of LVDTs on three-point bending test. ....	30
Table 3 – Description of position of LVDTs.....	32
Table 4 – Values of maximum compressive strength of the specimens.....	33
Table 5 - Values of Young’s module of the specimens.....	34
Table 6 - Values of tensile strength and Young’s module of $\varnothing 5$ bars in GFRP .....	36
Table 7 - Values of tensile strength and Young’s module of $\varnothing 3$ bars in GFRP .....	36
Table 8 – Geometric values of specimens in the 3PNBBT. ....	37
Table 9 – Relationship between CMOD and $\delta$ [10].....	37
Table 10 – values of post-cracking tensile strength. ....	39
Table 11 – Values of maximum capacity of the specimen in 4PBT. ....	40
Table 12 - Values of the geometry property used for designing the cross-section of the slab.....	63
Table 13 - Values for the compression behaviour of constitutive law of FRC. ....	64
Table 14 - Values for the tensile and post-cracking behaviour of FRC. ....	64
Table 15 - Values for the behaviour of GFRP.....	65
Table 16 - Values for the constitutive law of steel. ....	73
Table 17 – Values of tensile area used for the numerical models. ....	73

# Chapter 1

---

## 1. Introduction

### 1.1. General Consideration

Steel reinforcing bars in aggressive environmental conditions are generally affected by corrosion, which is often responsible for deterioration and damage processes developing in reinforced concrete (RC) members. This corrosion phenomenon can occur after carbonation of concrete cortical layers in members exposed to severe environmental conditions. Then, the possible oxidation of steel reinforcements causes the reduction of their cross-sectional area, concrete spalling and possibility to lose their bonding to the surrounding damaged concrete, which can compromise the functionality of RC structures, or even their structural stability. Since the rehabilitation of corroded RC structures is generally an expensive solution, demolition of such structures is a relatively frequent option, though resulting in several unfavourable impacts in terms of economic, social and environmental aspects.

Durability issues related to the possible oxidation of steel reinforcement in concrete structures have brought up the attention of civil engineers towards alternative materials for reinforcing systems.

Fiber Reinforced Polymers (FRPs), which were initially developed and employed in the aerospace, aeronautics, naval and automotive industries generally exhibit high mechanical and durability performance. Thus, the research of this thesis supports the publication of design guidelines on the use of FRP as internal reinforcement of cement-based composite members. FRP bars using Aramid, Carbon or Glass fibers, namely by AFRP, CFRP and GFRP, respectively, are the most widely reinforcing elements that are being used in construction industry.

A possible disadvantage of FRP bars comparing to steel bars is their cost in almost all cases. It is hard to compare the cost of FRP bars with those steel bars due to the many factors that may depend on. For instance, the delivery of FRP bars strongly depends on where they are ordered and from where they are supplied, and how much. Based on a rough analysis, it is expected to pay more FRP bars than steel. To this end, almost all FRP Reinforced Concrete (FRP-RC) applications are uneconomic, but the answer to this issue is considering a whole life cost of structures and not a first cost basis. The benefits of using FRP bars is to overcome the problem comes from the use of steel reinforcements. Thus, few amount of the cost spent for FRP-RCs refunds within the typical structure lifetime and many for much longer.

However, shear steel reinforcements need to be protected against corrosive agents, as they are more susceptible to corrosion due to the smaller concrete cover. For eliminating steel stirrups, a High-Performance Fiber Reinforced Concrete (HPFRC) might be a solution, as long as this material provides similar shear reinforcement effectiveness to the conventional steel reinforcement [1]. Due to the quite high postcracking tensile strength and energy absorption capacity that HPFRC can attain, this composite material can be used not only to assure the required shear capacity of RC elements, but also to enhance the structural performance at Serviceability and Ultimate Limit States (SLS and ULS).

## 1.2. Objectives

The objective of this thesis is the development of a nonlinear analytical model of three-dimensional structures. In order to experimental and numerical research. With the experimental tests it was intended to obtain a set of results that, on the one hand, would help to characterize the behaviour of spatial structures subject to multiaxial efforts and, on the other hand, it could be used for the calibration of the developed analytical model, finding the behaviour of these structures in the most correct way possible.

Furthermore, the present work is to develop high effective new reinforcing systems for the pre-fabrication industry of concrete beams. The beams are designed to support severe

environmental agents (e.g. in the coastline), in order to constitute a competitive alternative to the existing conventional structural solutions. The objective is achieved by developing a new generation material composed of Fiber Reinforced Concrete (FRC) with GFRP reinforcing bars.

### 1.3. Research steps

The main object of study in this work is the composite material realized by Fiber Reinforced Concrete (FRC) with Glass Fiber Reinforced Polymer (GFRP) bars.

In order to achieve the purpose of the study, the following steps were followed in the present research:

- Firstly, the study focused on evaluating the behaviour of the FRC and GFRP bars.
- Second, the study of flexural capacity of a slab composed of FRC with a three-dimensional textile reinforcement in GFRP (3D-SRT).
- Third step is to create a finite element model that simulate the non-linear behaviour of the slab subjected to bending moment.
- The last step is to compare the structural behaviour of FRC with 3D-SRT with the behaviour of FRC with traditional steel reinforcement.

# Chapter 2

---

## 2. State of the art on composite materials for new construction systems

### 2.1. Introduction

Concrete is a cement-based material that can exhibit a high compressive strength. Its main disadvantage consists in its brittleness, i.e. relatively low tensile strength and low tensile deformability. The use of tensile reinforcements in concrete structural elements improves their tensile and flexural response, limits the crack opening to acceptable values, and increases the stiffness of the structural elements after crack initiation. These reinforcements can be incorporated in a discrete manner, e.g. conventional steel or fiber reinforced polymer (FRP) in the form of bars or grids, or by dispersing fibers into the concrete matrix.

Although steel-reinforced concrete has high strength and stiffness, the major limitation of this material is its susceptibility to corrosion and subsequent deterioration. Textile materials can be used instead of steel to reinforce concrete. The outstanding durability of composites greatly extends the service life of the structure and reduces the inspection and maintenance costs, making them cost-effective. Some of the advantages of composites over traditional construction materials are high strength-to-weight ratio, ability to be manufactured in complex shapes, ability to tailor their mechanical properties according to specific needs, their noncorrosive nature, low thermal conductivity, and outstanding fatigue performance. One example is the use of GFRP and CFRP reinforcement in the Wotton Bridge's deck [11].

### 2.2.1. Fiber Reinforced Concrete (FRC)

The use of fiber reinforced concrete in the construction of structural systems has been progressively increasing in the last decades for new construction and repair operations of building's structural elements, shell type structures, pre-fabrication elements, tunnel linings, decks of bridges, marine structures, etc.

In the last decades, an extensive research has been conducted on FRC structures, mainly concerning the description of fiber reinforcement potentialities and experimental characterization from the material to the structural level.

In the market exist fibers of several types of materials geometric configurations. Although the employment of fiber reinforcements in concrete is dated to the beginning of the 1900's, it was majorly since its modern age development that fiber reinforced concrete (FRC) has been showing enormous potentialities for use in structural elements [2].

Fiber reinforcement is being also explored with appreciable success on the partial or integral replacement of transverse reinforcement, such in the shear reinforcement of beams or in the punching reinforcement of slabs; decreasing the construction time; and reducing maintenance costs. When used in structural elements, fiber reinforcement can: improve the tensile and flexural response; increase the shear and punching resistance of concrete; restrain the crack opening; decrease the tensile stress in conventional reinforcement; improve the bond performance of conventional reinforcement to surrounding concrete.

The use of short and randomly distributed fibers increases concrete post-cracking tensile capacity, its ductility, energy absorption capacity and impact resistance when compared to plain concrete. Additionally, the restraint to crack propagation, provided by the different fiber reinforcement mechanisms enhances the durability and integrity of cement based materials. The fundamental reinforcement mechanism of fibers consists in the capacity of ensuring relatively high stress transfer between the faces of cracks, by restraining the degeneration of micro-cracks in meso- and macrocracks, which increases the stiffness and load carrying capacity of concrete structures in their cracking stage, as well as their durability [3] – [5]. Fiber contribution after cracking depends mainly on the

content of fibers, their orientation and distribution towards the potential cracks, the material and geometric characteristics of the fibers, and the mechanical properties of the concrete, which are designated as the variables that mainly affect the fiber reinforcement mechanisms. Likewise, the compressive strength of FRC's is similar to plain concrete, while the post-peak load and deformation capacity increase with the variables that have a favourable influence on the fiber reinforcement mechanisms [6].

Generally, fibers with high modulus of elasticity and tensile strength can improve significantly the postcracking strength of cement based materials, like steel, carbon and PVA fibers, while low-modulus fibers are mostly used to control cracking shrinkage at early ages [2].

Although some design rules and codes have been developed, as is the case of the fib Model Code 2010 [8], in the designer's community there is still a lack of knowledge in the analysis of FRC structures, which avoids a faster use of this material, with economic and technical detrimental impact in the construction sector.

### 2.2.2. Three-Dimensional System Reinforcement Textile (3D-SRT)

Textile reinforcement is a composite material encompassing discrete textile reinforcement in the form of a grid or open mesh structure made of non-corrosive technical fibres embedded in a fine-grained cementitious matrix. A main aspect differentiating TRC from other types of cement-based composites, e.g. FRC, is that fibres are bundled and arranged in a discrete open structure which can be positioned according to the imposed tensile stresses similar to conventional RC thus increasing the load capacity and effectiveness of the fibers. A coverage material is typically applied to the filaments to provide surface protection and improve the interaction between them in an assembled group (Figure 1).

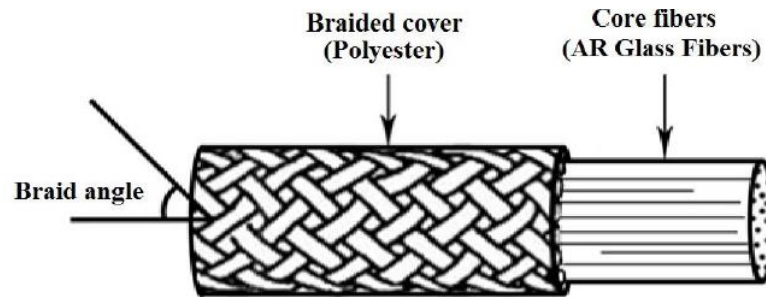


Figure 1 – Structure of a GFRP bar

The textile reinforcements are typically classified as being two-dimensional planar or conventional (2D), three-dimensional (3D) or hybrid structures. In the bi-axial case, the grid comprises two groups of yarns interconnected orthogonally. In tri and multi-axial cases, there are intermediate yarns diagonally placed in reference to the warp and weft directions.

The composite in two dimensional (2D) textiles is reinforced in directions parallel, but not orthogonal, to the fabric plane. If using 2D textiles to reinforce a composite, laminated composites should be prepared using several textile layers because are characterized by poor shear.

3D-SRT (3 Dimensional System Reinforcement Textile) are produced connecting two separate, independent 2D-SRT mesh together with a third set of glass fiber rods along the thickness of the fabric (Figure 2). The connecting glass fiber rods, referred to as spacer rods, provide both stabilization and shear reinforcement.

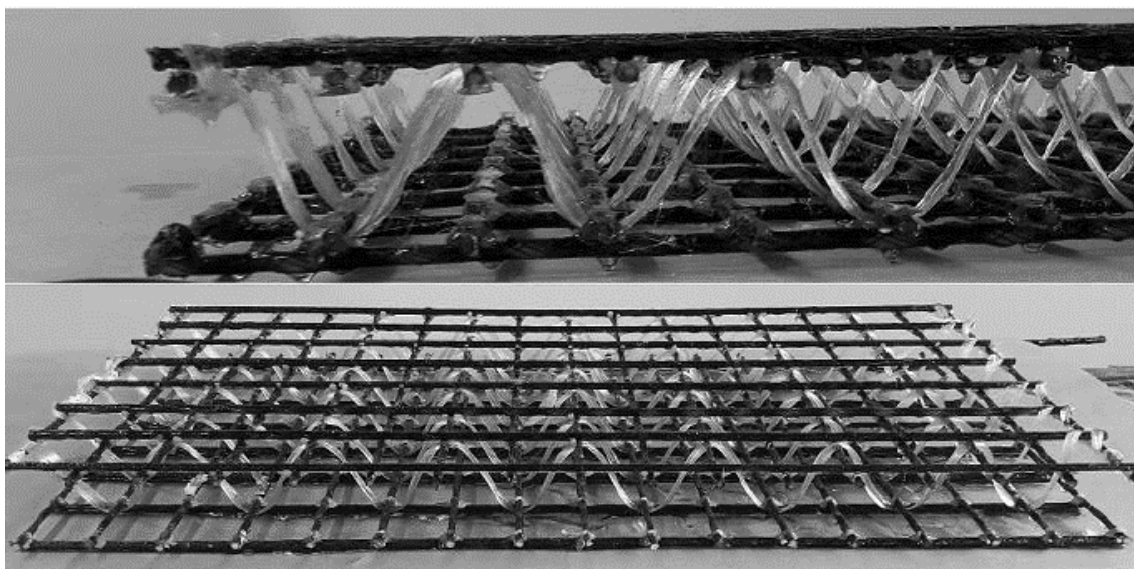


Figure 2 - Structure of a manufactured 3D-SRT reinforcement

## 2.2. Constitutive laws of FRC in tension

The FRC compressive behaviour is similar to the one observed in usual Concrete. Accordingly, the stress-strain relationships defined in Eurocode 2 [7] or MC2010 [8] for the concrete can also be used for characterizing the compressive behaviour of FRC.

On the other hand, the tensile behaviour of FRC has two types of responses can be obtained: strain-softening or strain-hardening. A FRC has a tensile strain-softening behaviour when a reduction of load carrying capacity with the increase of crack width opening occurs after the formation of the first crack (Figure 3a). Conversely, in a strain-hardening material the load carrying capacity increases with the material deformation (Figure 3b).

In strain-softening FRC a major failure crack is formed, while in strain-hardening a diffuse crack pattern is observed. Commonly, for usual volume contents of fibers, FRC's exhibit a tensile strain-softening behaviour, while for high performance matrix and high fiber contents ( $>1.5\%$  in volume of FRC) is possible to attain a strain-hardening behaviour [9].

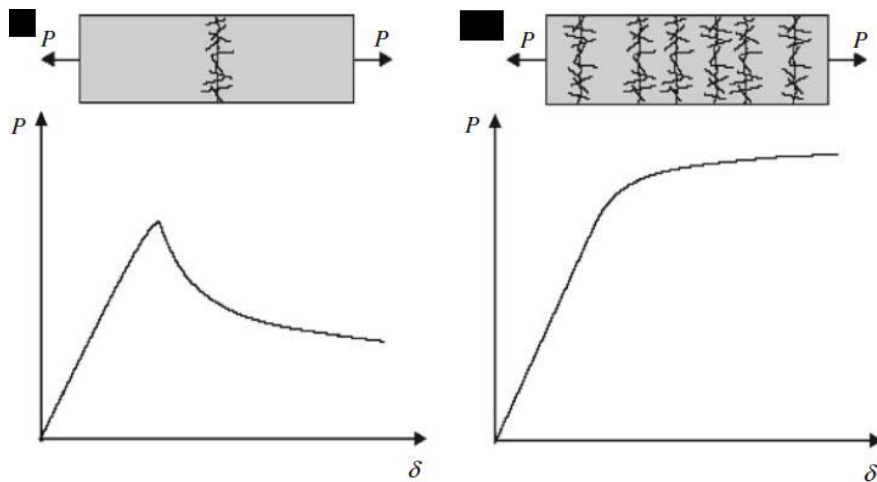


**Figure 3** - Typical load ( $P$ ) – deformation ( $\delta$ ) of FRC: a) Tensile strain-softening; b) Tensile strain-hardening [8].

For the characterization of FRC, 3-point notched beam bending tests (3PNBBT) are executed according to EN 14651 [10]. From the execution of 3PNBBT, it is possible to evaluate the post-cracking tensile strength of a FRC. The test setup and typical load vs. crack mouth opening displacement (CMOD) relationship are presented in Figure 4. Based

on the force values,  $F_j$  ( $j = 1,2,3,4$ ) corresponding to specific values of CMOD, the residual flexural tensile strength,  $f_{Rj}$ , is determined from the following expression:

$$f_{Rj} = \frac{3 \cdot F_j \cdot l}{2 \cdot b \cdot h_{sp}^2} \quad \text{Eq. (2.1)}$$

where  $l$  is the span length of the test beam;  $b$  is the width of the specimen's cross section; and  $h_{sp}$  is the distance between the notch tip and the beam top face. By specifying the values of the residual flexural strength, it is possible to compare the post-cracking behaviour of different FRC's compositions.

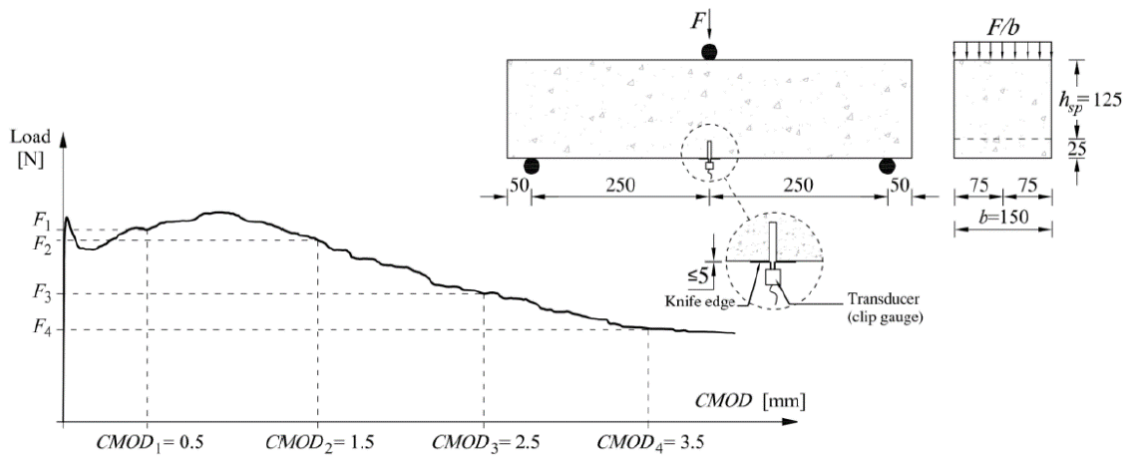


**Figure 4** - Typical load-CMOD curve of FRC [8] (dimensions in mm).

In fact, the MC2010 resorts to the residual flexural strength concept to classify the post-cracking performance of a FRC, by adopting a toughness class. The toughness class is determined from the characteristic values of the residual flexural tensile strength of FRC for serviceability,  $f_{R1k}$ , and ultimate limit state condition,  $f_{R3k}$ . The value of  $f_{R1k}$  corresponds to  $CMOD_1 = 0.5mm$  and  $f_{R3k}$  to  $CMOD_3 = 2.5mm$ .

For structural applications, MC2010 specifies that a minimum ratio between the residual tensile strength at  $CMOD = 2.5mm$  and  $CMOD = 0.5mm$  (Eq. (2.2)) should be verified in order to consider the tensile contribution of FRC in the ultimate limit state (ULS) resistance of a structural element [8].

$$\frac{f_{R3k}}{f_{R1k}} \geq 0.5 \quad \text{Eq. (2.2)}$$

An additional condition is also specified in MC2010, related with the ratio between the characteristic value of the limit of proportionality,  $f_{Lk}$ , and the residual

strength,  $f_{R1k}$  (Eq. (2.3)) [8]. The value of  $f_{Lk}$  is given by Eq. (2.1), considering the maximum load value,  $F_L$ , registered on the 3PNBBT up to  $CMOD = 0.05\text{mm}$  [10].

$$\frac{f_{R1k}}{f_{Lk}} > 0.4 \quad \text{Eq. (2.3)}$$

Contrarily to simple concrete where the tensile strength is usually neglected in the design process of structural elements, FRC can exhibit a significant post-cracking tensile capacity. In the pre-peak stage, it is possible to assume that FRC and concrete have similar response, and the existing stress-strain relationship used for concrete is also applicable to FRC until this stage [8], see Figure 5:

$$\left\{ \begin{array}{l} \sigma = E_c \cdot \varepsilon ; \\ \sigma = f_{ct} \cdot \left( 1 - 0.1 \cdot \frac{0.15 \times 10^{-3} - \varepsilon}{0.15 \times 10^{-3} - 0.9 \cdot \frac{f_{ct}}{E_c}} \right) ; \end{array} \right. \quad \begin{array}{l} 0 \leq \varepsilon \leq 0.9 \cdot \frac{f_{ct}}{E_c} \\ 0.9 \cdot \frac{f_{ct}}{E_c} < \varepsilon \leq (\varepsilon_p = 0.15\text{‰}) \end{array}$$

Eq. (2.4)

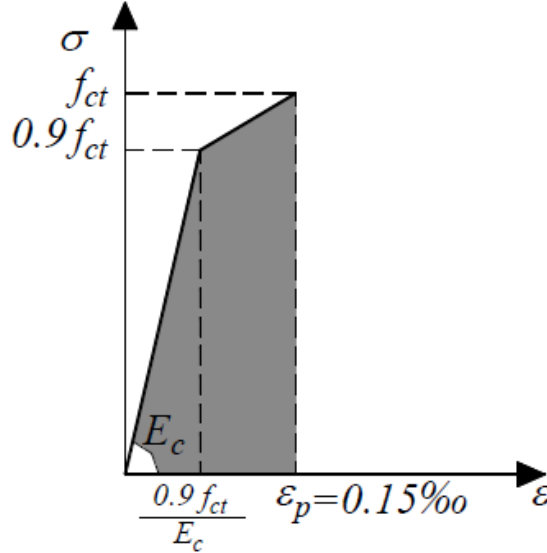


**Figure 5** - Tensile stress-strain relationship for plain concrete and FRC up to material tensile strength.

As the formation of cracks in concrete is a discrete phenomenon, a stress-crack opening relationship is the most suitable formulation to describe FRC post-cracking behaviour, mainly in FRC of tensile-softening nature, which is the most current in structural applications. In MC2010 different approaches are used to characterize the post-cracking tensile behaviour of FRC, depending on the type of limit state verification.

For the ULS analysis two models can be used: the (i) rigid-plastic model; and the (ii) linear model. Both models are schematically presented in Figure 6, where:  $w_u$  is the ultimate crack opening corresponding to the ULS criterion  $f_{Ftu}$ ;  $f_{Ftu}^h$  is the ultimate residual tensile strength; and  $f_{Fts}$  is the serviceability residual tensile strength. For FRC with a softening post-cracking behaviour (solid lines in Figure 6) the value  $f_{Ftu}$  is lower than  $f_{Fts}$ , while for a hardening post-cracking response (dashed lines in Figure 6) the value  $f_{Ftu}$  is higher than  $f_{Fts}$ .

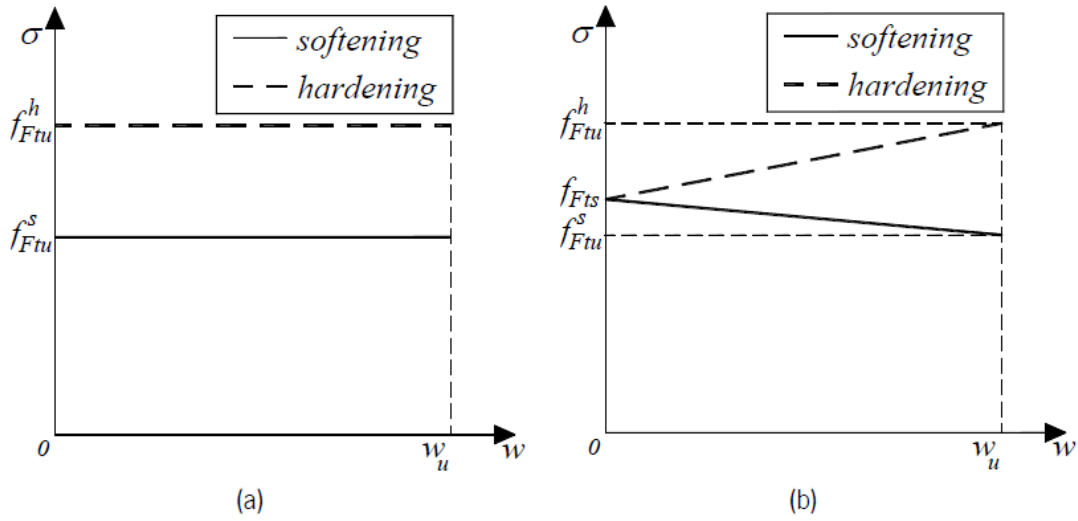


**Figure 6** - Stress-crack opening constitutive laws for ULS analysis: a) rigid-plastic model; b) linear model [8].

For the rigid-plastic model, the ultimate residual tensile strength is determined from [8]:

$$f_{Ftu} = \frac{f_{R3}}{3} \quad \text{Eq. (2.5)}$$

For the linear model, the serviceability and ultimate residual tensile strength are obtained from [8]:

$$f_{Fts} = 0.45 \cdot f_{R1} \quad \text{Eq. (2.6)}$$

$$f_{Ftu} = f_{Fts} - \frac{w_u}{CMOD_3} \cdot (f_{Fts} - 0.5 \cdot f_{R3} + 0.2 \cdot f_{R1}) \geq 0 \quad \text{Eq. (2.7)}$$

For the rigid-plastic model the value of the ultimate crack opening is equal to  $w_u = CMOD_3$ , while for the linear model it depends on the ductility required, namely:

$$w_u = \min(2.5 \text{ mm}; l_{cs}; \varepsilon_{Fu}) \quad \text{Eq. (2.8)}$$

where,  $\varepsilon_{Fu}$  is the ultimate tensile strain of FRC; and  $l_{cs}$  is the structural characteristic length.

According to the MC2010, the ultimate tensile strain,  $\varepsilon_{Fu}$ , depends on the strain distribution along the cross-section. For a constant tensile strain (section under pure normal tensile force),  $\varepsilon_{Fu} = 1\%$ . For variable strain distribution in the cross-section (section under pure bending or combined axial bending load),  $\varepsilon_{Fu} = 2\%$  [8].

In structural elements with steel bars reinforcement, the structural characteristic length is determined from [8]:

$$l_{cs} = \min(y; s_{rm}) \quad \text{Eq. (2.9)}$$

where,  $y$  is the distance between the neutral axis position and the tensile side of the cross-section (Figure 7); and  $s_{rm}$  is the mean crack spacing. In the evaluation of the neutral axis position,  $x$ , a loading situation corresponding to the cracking serviceability criteria is assumed, generally the quasi-permanent load combination; and the tensile contribution of FRC can be disregarded [8]. An example of stress-strain distribution in a cross-section for the calculation of the neutral axis is presented in Figure 7. For sections without traditional reinforcements, the value of the structural characteristic length,  $l_{cs}$ , is considered equal to the cross-section height,  $h$  [8].

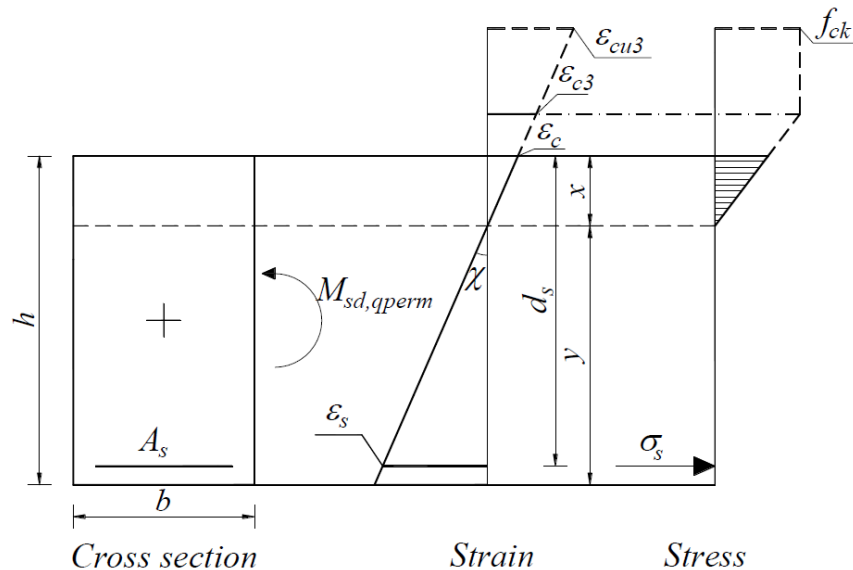


**Figure 7** - Example of determination of neutral axis position,  $x$ , and  $y$  for the evaluation of  $l_{cs}$ .

The mean crack spacing,  $s_{rm}$ , can be estimated from the bond transfer length,  $l_{s,max}$ . It is the length needed for concrete to reach its tensile strength,  $\sigma = f_{ctm}$ , due to

bond action. Therefore, new cracks cannot occur within the distance  $l_{s,max}$  from the cracks, as stress on concrete does not reach its tensile strength within this transition zone. The bond transfer length and the mean crack spacing can be determined through the following equation [6]:

$$l_{s,max} = \frac{f_{ctm}}{4 \cdot \tau_{bms}} \cdot \frac{\emptyset}{\rho} \quad \text{Eq. (2.10)}$$

$$s_{rm} = 1.5 \cdot l_{s,max} \quad \text{Eq. (2.11)}$$

where  $\tau_{bms}$  is the mean bond strength between the bar and concrete;  $\emptyset$  is the diameter of the bar; and  $\rho = A_c/A_s$  is the ratio of longitudinal reinforcement.

To transform the stress-crack opening relationship in a stress-strain diagram, the MC2010 [8] proposes to convert the concept of crack opening,  $w$ , in tensile strain,  $\varepsilon$ , by using the structural length parameter:

$$\varepsilon = \frac{w}{l_{cs}} \quad \text{Eq. (2.12)}$$

In Figure 8a is presented the complete stress-strain diagram for a strain softening FRC, assuming that  $f_{Fts} < f_{ct}$  and the FRC's post-cracking linear model (Figure 6b). However, for the usual cases where  $\varepsilon_{ULS} \gg \varepsilon_p$ , and for an analytical estimation of the cross-section flexural capacity, the pre-cracking contribution of FRC can be disregarded and the simplified stress-strain diagram presented in Figure 8b can be adopted without a significant loss of precision.

During the analysis of a cross-section, if  $\varepsilon > \varepsilon_{ULS}$  a stress cut-off is assumed. The complete tensile stress-strain diagram presented in Figure 8a is mathematical described by Eq. (2.13), while in Eq. (2.14) is presented the simplified model.

$$\left\{ \begin{array}{l} \sigma = E_c \cdot \varepsilon \\ \sigma = 0.9 \cdot f_{ct} + \left( \frac{f_{ct} - 0.9 \cdot f_{ct}}{\varepsilon_p - 0.9 \cdot \frac{f_{ct}}{E_c}} \right) \cdot \left( \varepsilon - 0.9 \cdot \frac{f_{ct}}{E_c} \right) \\ \sigma = f_{Fts} + \left( \frac{f_{Ftu} - f_{Fts}}{\varepsilon_{ULS} - \varepsilon_p} \right) \cdot (\varepsilon - \varepsilon_p) \\ \sigma = 0 \end{array} \right. \quad \begin{array}{l} ; 0 \leq \varepsilon \leq \frac{0.9 \cdot f_{ct}}{E_c} \\ ; \frac{0.9 \cdot f_{ct}}{E_c} < \varepsilon \leq \varepsilon_p \\ ; \varepsilon_p < \varepsilon \leq \varepsilon_{ULS} \\ ; \varepsilon > \varepsilon_{ULS} \end{array} \quad \text{Eq. (2.13)}$$

$$\left\{ \begin{array}{l} \sigma = f_{ts} + \left( \frac{f_{Ftu} - f_{Fts}}{\varepsilon_{ULS} - \varepsilon_p} \right) \cdot \varepsilon \\ \sigma = 0 \end{array} \right. \quad \begin{array}{l} ; 0 \leq \varepsilon \leq \varepsilon_{ULS} \\ ; \varepsilon > \varepsilon_{ULS} \end{array} \quad \text{Eq. (2.14)}$$

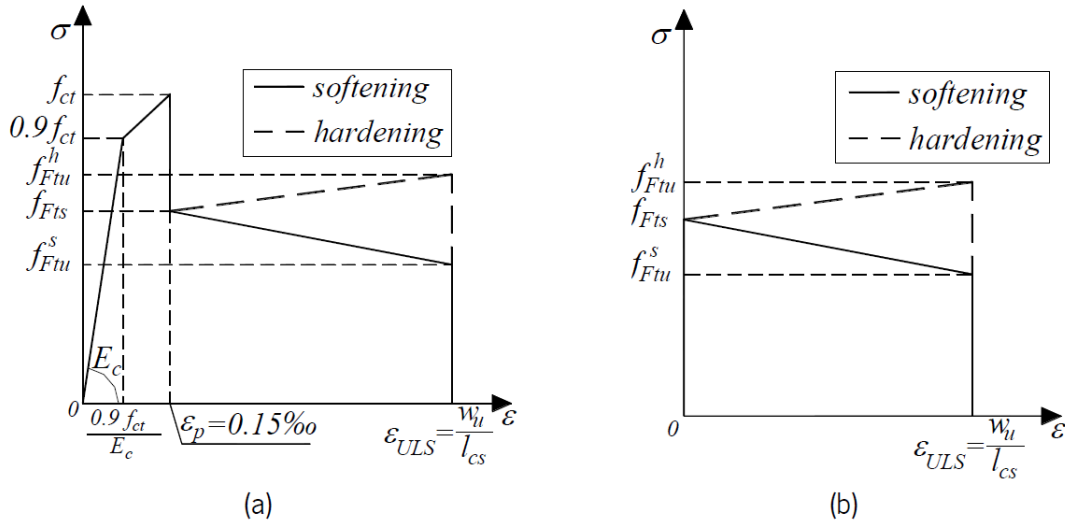


**Figure 8** - Stress-strain relationship of a strain softening FRC, for ULS analysis: (a) complete diagram; (b) simplified diagram.

For the verification of the serviceability limit states (SLS), one of the three stress-strain models presented in MC2010 (Figure 9) is applicable. The residual tensile strength  $f_{Fts}$  and  $f_{Ftu}$  are determined from Eq. (2.6) and Eq. (2.7), respectively.

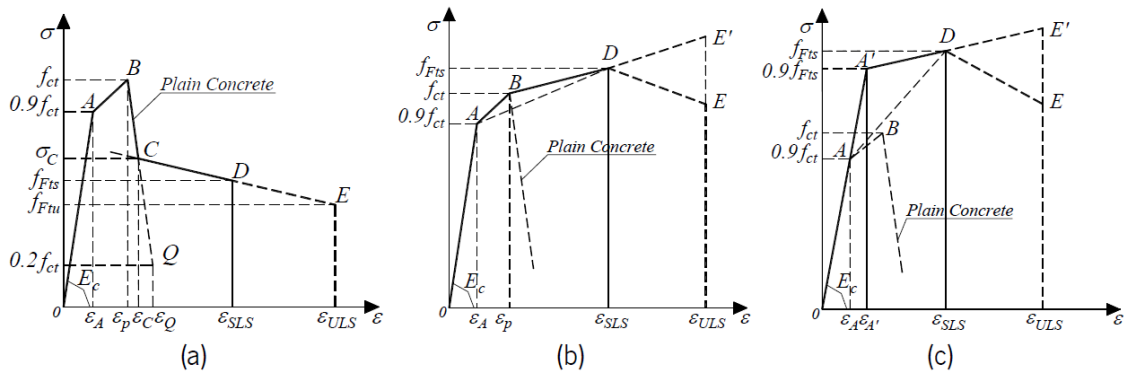


**Figure 9** - Stress-strain relationship for SLS analysis: (a) Case I; (b) Case II; (c) Case III [8].

The constitutive models presented in Figure 9 have common defining points, namely points A, B, D and E. Points A and B correspond to the stress and strain values defined for un-macro-cracked plain concrete (Figure 5). Point D and E correspond,

respectively, to the serviceability and ultimate deformation criteria of the material, which are determined by [8]:

$$\begin{cases} \varepsilon_{SLs} = \frac{CMOD_1}{l_{cs}} \\ \varepsilon_{ULs} = w_u/l_{cs} \end{cases} \quad \text{Eq. (2.15)}$$

where  $CMOD_1 = 0.5 \text{ mm}$  and  $l_{cs}$  is determined as previously described.

The first model, Case I (Figure 9a), is applicable for softening materials with  $f_{Fts} < f_{ct}$ . The stress of point Q is equal to  $\sigma_Q = 0.2 \cdot f_{ct}$ , and its corresponding strain is determined from the following equation [8]:

$$\varepsilon_Q = \frac{G_F}{f_{ct} \cdot l_{cs}} + \left( \varepsilon_p - \frac{0.8 \cdot f_{ct}}{E_c} \right) \quad \text{Eq. (2.16)}$$

where  $G_F$  represents the fracture energy of a plain concrete of the same strength class of the FRC, which can be estimated from the following expression [8]:

$$G_F = \frac{73 \cdot f_{cm}^{0.18}}{1000} \left[ \frac{N}{mm} \right] \quad \text{Eq. (2.17)}$$

where  $f_{cm}$  is the mean compressive strength of concrete, in MPa, that can be determined from the following expression [8]:

$$f_{cm} = f_{ck} + 8 \text{ Mpa} \quad \text{Eq. (2.18)}$$

Point C coordinates are determined from the intersection of lines BQ and DE, which represents the intersection of the concrete matrix post-cracking strength with the post-cracking residual strength of FRC. Due to the dependence of  $\varepsilon_Q$  on the values of  $f_{ct}$  and  $l_{cs}$ , the application of Eq. (2.16) can result a value of strain lower than that for the tensile strength,  $\varepsilon_Q < \varepsilon_p$ , which has no physical meaning. In this situation, the concrete matrix post-cracking contribution is discarded, and it is assumed that  $\varepsilon_Q = \varepsilon_p = 0.15\%$ , as presented in Figure 10.

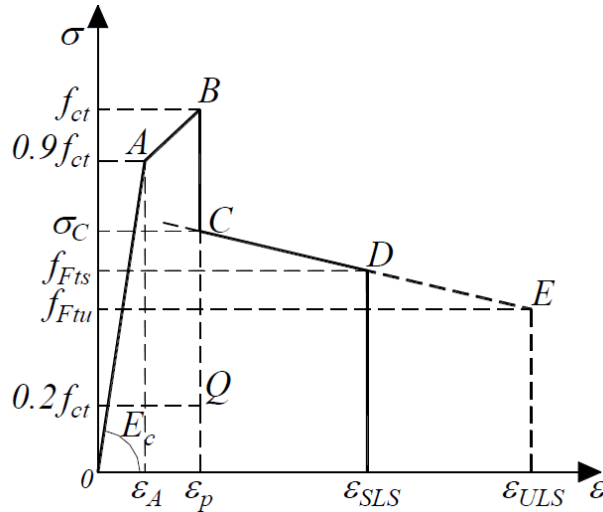


**Figure 10** - SLS stress-strain case I model for situation where concrete matrix post-cracking contribution is disregarded.

Additionally, the present formulation can also result in a situation where the intersection of both lines yields  $\varepsilon_C < \varepsilon_P$  (Figure 11). In this circumstance, point C is disregarded, and point D is connected to point B.

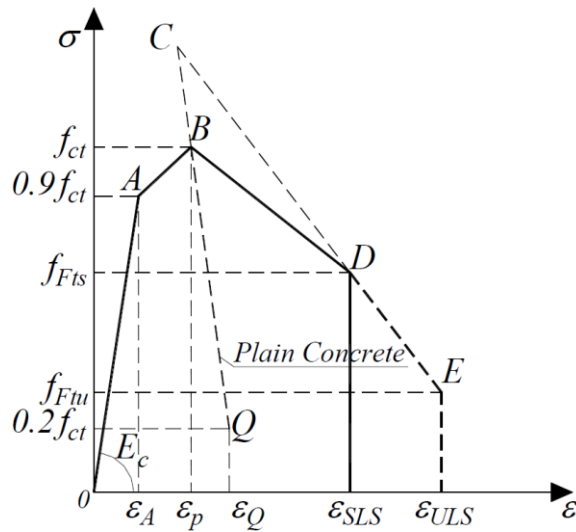


**Figure 11** - Example of SLS stress-strain Case I model where point C is disregarded.

Cases II and III are applicable for materials exhibiting a stable crack propagation up to  $\varepsilon_{SLS}$ , with  $f_{Fts} > f_{ct}$ . Case II is applicable when:

$$\frac{\sigma_D - \sigma_A}{\varepsilon_{SLS} - \varepsilon_A} \leq \frac{\sigma_B - \sigma_A}{\varepsilon_P - \varepsilon_A} \Leftrightarrow \frac{f_{Fts} - 0.9 \cdot f_{ct}}{\varepsilon_{SLS} - 0.9 \cdot \frac{f_{ct}}{E_c}} < \frac{f_{ct} - 0.9 \cdot f_{ct}}{\varepsilon_P - 0.9 \cdot \frac{f_{ct}}{E_c}} \quad \text{Eq. (2.19)}$$

otherwise Case III is adopted. The equation Eq. (2.19) compares the slope of lines AD and AB. If the slope of line AD is lower than the slope of line AB, Case II is applied, otherwise Case III should be chosen. Case III has an additional point, A', which stress value is  $\sigma_{A'} = 0.9 \cdot f_{Fts}$  and corresponding strain is  $\varepsilon_{A'} = 0.9 \cdot \frac{f_{Fts}}{E_c}$ .

In the safety assessment of a member at SLS, the principal tensile strain cannot exceed  $\varepsilon_{SLS}$ , where a stress cut-off is admitted.

Similarly, to the consideration adopted for the ULS stress-strain diagram, in the common situation where  $\varepsilon_{SLS} \gg \varepsilon_p$ , for analytical calculation of the cross-section flexural capacity, the pre-cracking contribution of FRC can be disregarded without a significant loss of precision.

### 2.3. Shear resistance of FRC

Fiber reinforcement enhances the shear capacity of concrete and allows a partial or total replacement of steel stirrups in structural elements [6]. According to MC2010, the design value of the shear resistance of an FRC structural element with longitudinal bars and without shear reinforcement,  $V_{Rd,F}$ , can be evaluated by employing the expression [8]:

$$V_{Rd,F} = \left( \frac{0.18}{\gamma_c} \cdot k \cdot \left( 100 \cdot \rho_{sl} \cdot \left( 1 + 7.5 \cdot \frac{f_{Ftuk}}{f_{ctk}} \right) \cdot f_{ck} \right)^{\frac{1}{3}} + 0.15 \cdot \sigma_{cp} \right) \cdot b_w \cdot d \quad \text{Eq. (2.20)}$$

where:

- $\gamma_c = 1.5$  is the partial safety factor for concrete without fibers;
- $k = 1 + \sqrt{\frac{200}{d}} \leq 2$  is a factor that considers the size effect;
- $d$  is the effective depth of the cross section [mm];
- $\rho_{sl} = \frac{A_{sl}}{(b_w \cdot d)}$  is the longitudinal reinforcement ratio;

- $A_{sl}$  is the cross-sectional area of the longitudinal reinforcement;
- $f_{Ftuk}$  is the characteristic value of the ultimate residual tensile strength of the FRC that is computed from Eq. (2.7) considering the characteristic values of the residual flexural strength of FRC and  $w_u = 1.5 \text{ mm}$ ;
- $f_{ctk}$  is the characteristic tensile strength for the concrete without fibers;
- $f_{ck}$  is the characteristic compressive strength;
- $\sigma_{cp} = \frac{N_{ed}}{A_c} < 0.2 \cdot f_{cd}$  is the average axial stress acting in the cross-section (considered positive in compression);
- $b_w$  is the smallest width of the tensile zone of the cross-section.

The previous equation is based on the one proposed by Eurocode 2 [7] for shear contribution of plain concrete members without transverse reinforcements, by adding the contribution of FRC residual flexural strength. The effect of the dispersed fibers to shear resistance provided by the increased post-cracking toughness and crack-opening restriction is empirically considered by multiplying the longitudinal reinforcement ratio by the factor  $\left(1 + 7.5 \cdot \frac{f_{Ftuk}}{f_{ctk}}\right)$ . Therefore, the contribution of fiber reinforcement is regarded as an extra flexural reinforcement, whose favourable mechanism for the shear capacity derives from the dowel effect.

It should be noticed that in Eurocode 2 is considered an upper limit of to the value of the longitudinal reinforcement ratio  $\rho_{sl} \leq 0.02$  to be used in the calculation of the shear resistance of plain concrete members.

The applicability of Eq. (2.20) is limited to elements where shear diagonal failure is expected and arch action is insignificant, namely for elements with ratio  $\frac{a}{d} \geq 2.5$ , being  $a$  the shear span [6].

The shear resistance,  $V_{Rd,F}$ , is assumed to be not smaller than the minimum value,  $V_{Rd,F,min}$ , obtained from:

$$V_{Rd,F,min} = (v_{min} + 0.15 \cdot \sigma_{cp}) \cdot b_w \cdot d \quad \text{Eq. (2.21)}$$

$$v_{min} = 0.035 \cdot k^{\frac{3}{2}} \cdot f_{ck}^{\frac{1}{2}} \quad \text{Eq. (2.22)}$$

In MC2010, for structural members with transverse reinforcements is considered the following relation:

$$V_{Rd} = V_{Rd,s} + V_{Rd,F} \leq V_{Rd,max} \quad \text{Eq. (2.23)}$$

where,  $V_{Rd,s}$  is the shear resistance provided by the transversal reinforcement and  $V_{Rd,max}$  is the maximum shear capacity without concrete crushing.

The shear reinforcement resistance,  $V_{Rd,s}$ , is determined according to the following expression [8]:

$$V_{Rd,s} = \frac{A_{sw}}{s_w} \cdot z \cdot f_{ywd} \cdot (\cot \theta + \cot \alpha) \cdot \sin \alpha \quad \text{Eq. (2.24)}$$

where  $A_{sw}$  is the shear reinforcement area;  $s_w$  is the longitudinal spacing between shear reinforcement bars; and  $f_{ywd}$  is design value of the yield strength of the shear reinforcement.

The FRC shear resistance,  $V_{Rd,F}$ , is the result of the added shear resistance of the concrete matrix,  $V_{Rd,c}$ , and fiber reinforcements bridging the shear cracks,  $V_{Rd,f}$ , and is determined from [8]:

$$V_{Rd,F} = V_{Rd,c} + V_{Rd,f} = \frac{1}{\gamma_F} \cdot (v_{Rd,c} + v_{Rd,f}) \cdot z \cdot b_w \quad \text{Eq. (2.25)}$$

where,  $z$  is the internal lever arm, that can be estimated as  $z = 0.9 \cdot d$  [8]. The concrete matrix shear strength is provided by the aggregate interlock, which is dependent on the concrete compressive strength, size of aggregate particles and on the shear crack width, namely [8]:

$$v_{Rd,c} = k_v \cdot \sqrt{f_{ck}} \quad \text{Eq. (2.26)}$$

where  $k_v$  is the parameter that determines the contribution of the aggregate interlock mechanism for the shear strength of the cross section (Eq. (2.27)). The parameter  $k_v$  is function of the parameter that considers the aggregate size influence (Eq. (2.28)),  $k_{dg}$ , and of the longitudinal strain at the mid depth of the effective shear area,  $\epsilon_x$ .

$$k_v = \begin{cases} \frac{0.4}{1 + 1500 \cdot \varepsilon_x} \cdot \frac{1300}{1000 + z \cdot k_{dg}} & \text{for } \rho_w < 0.08 \cdot \sqrt{f_{ck}/f_{yk}} \\ \frac{0.4}{1 + 1500 \cdot \varepsilon_x} & \text{for } \rho_w \geq 0.08 \cdot \sqrt{f_{ck}/f_{yk}} \end{cases} > 0 \quad \text{Eq. (2.27)}$$

$$k_{dg} = \begin{cases} \frac{32}{16 \cdot d_g} \geq 0.75 & \text{for } f_{ck} \leq 70 \text{ Mpa} \\ 2.0 & \text{for } f_{ck} > 70 \text{ Mpa} \end{cases} \quad \text{Eq. (2.28)}$$

In Eq. (2.27), the term  $\rho_w$  represents the transverse reinforcement ratio of the cross-section, that is given by [8]:

$$\rho_w = \frac{A_{sw}}{b_w \cdot s_w \cdot \sin \alpha} \quad \text{Eq. (2.29)}$$

where,  $A_{sw}$  is the shear reinforcement area;  $s_w$  is the longitudinal spacing between shear reinforcement bars; and  $\alpha$  is the inclination of the transverse reinforcements with the element longitudinal axis. In Eq. (2.28) the term  $d_g$  is the maximum aggregate dimension in the concrete matrix.

The strain,  $\varepsilon_x$ , at mid-depth of the effective shear depth can be defined as:

$$\varepsilon_x = 0 \leq \frac{1}{2 \cdot E_s \cdot A_{sl}} \cdot \left( \frac{M_{Ed}}{z} + V_{ed} + N_{ed} \cdot \left( \frac{1}{2} \pm \frac{\Delta e}{z} \right) \right) \leq 0.03 \quad \text{Eq. (2.30)}$$

MC2010 presents the following conditions for application of Eq. (2.30):

- $A_{sl}$  comprises the main longitudinal reinforcement in the tensile chord, while any other distributed longitudinal reinforcement must be disregarded;
- If longitudinal reinforcement bars do not respect the required development length,  $l_p$ , (§6.1.8.6 MC2010) from the section under consideration, the value of  $A_{sl}$  must be reduced proportionally to the lack of development length;
- If the strain  $\varepsilon_x$  is negative (compression), it must be taken as zero;
- When analysing sections within a distance  $z/2$  of a significant rebar curtailment, the value  $\varepsilon_x$  must be multiplied by 1.5;
- If the axial tension is large enough to crack the flexural compression face of the section, the value of  $\varepsilon_x$  must be multiplied by 2.

The shear strength provided by the fiber reinforcements bridging the shear diagonal cracks is obtained from [8]:

$$v_{Rd,f} = k_{df} \cdot f_{Tk}(w_u) \cdot \cot \theta \quad \text{Eq. (2.31)}$$

where,  $k_{df}$  is a fiber dispersion reduction factor, assuming the value of  $k_{df} = 0.8$  [8];  $f_{Tk}(w_u)$  is the characteristic value of the post-cracking tensile capacity of FRC, evaluated at the ultimate crack width,  $w_u$ , that can be determined from direct tensile tests. As the execution of direct tensile tests is quite cumbersome, alternatively,  $f_{Tk}(w_u)$  can be estimated according to Eq. (2.32), considering  $w = w_u$  [6]:

$$f_{Tk}(w) = k_G \cdot \min (0.4 \cdot f_{R2k} + 1.2 \cdot (f_{R4k} - f_{R2k}) \cdot \xi(w) \quad \text{Eq. (2.32)}$$

$$\xi(w) = \alpha \cdot w - 0.25 \quad \text{Eq. (2.33)}$$

The value of  $k_G$  is presented in Table 1, considering the different prism bending test standards. The value of factor  $\alpha$  also depends on the prism bending test configuration and is presented in the same table.

**Table 1** - Value of  $k_G$  and  $\alpha$  depending on prism bending test standard [6].

Prism bending test normative	$k_G$	$\alpha$
ASTM 1609 [62]	0.70	1/3
EN 14651 [34]	0.60	5/12
RILEM TC 162-TDF [35]	0.60	5/12
UNI 11039 [63]	0.60	43/84

The residual flexural strength  $f_{R2k}$  and  $f_{R4k}$ , can be estimated from analysis of the results of 3PNBBT.

According to MC2010, the value of  $\theta$  can be freely chose in the interval of  $\theta_{min} \leq \theta \leq 45^\circ$ , while the value of  $\theta_{min}$  is related with the longitudinal strain level in the mid-depth of the cross-section,  $\varepsilon_x$ , which can be obtained from [8]:

$$\theta_{min} = (29^\circ + 7000 \cdot \varepsilon_x) \quad \text{Eq. (2.34)}$$

The design shear resistance cannot exceed the crushing capacity of concrete in the web, determined as [8]:

$$V_{Rd,max} = k_c \cdot \frac{f_{ck}}{\gamma_c} \cdot b_w \cdot z \cdot \frac{\cot \theta \cdot \cot \alpha}{1 + \cot^2 \theta} \quad \text{Eq. (2.35)}$$

where,  $k_c$  is a strength reduction factor, defined by:

$$k_c = k_\varepsilon \cdot \eta_{fc} \quad \text{Eq. (2.36)}$$

where  $k_\varepsilon$  is a factor that takes into account the strain in the web of the structural element, and is determined according to the level approximation defined in MC2010 (level of approximation I:  $k_\varepsilon = 0.55$ ; level of approximation II and III : Eq. (2.37));  $\eta_{fc}$  is a factor to consider the effect of more brittle failure for high strength concrete compositions, and is determined from Eq. (2.39); and  $\theta$  is the inclination of the principal compressive stress in the web, relative to the longitudinal axis of the member.

$$k_\varepsilon = \frac{1}{1.2 + 55 \cdot \varepsilon_1} \leq 0.65 \quad \text{Eq. (2.37)}$$

$$\varepsilon_1 = \varepsilon_x \cdot (\varepsilon_x + 0.002) \cdot \cot^2 \theta \quad \text{Eq. (2.38)}$$

$$\eta_{fc} = \left( \frac{30}{f_{ck}} \right)^{1/3} \leq 1.0 \quad (f_{ck} \text{ in Mpa}) \quad \text{Eq. (2.39)}$$

# Chapter 3

---

## 3. Experimental Program

### 3.1. Introduction

The tasks associated with the design of fiber reinforced concrete beams (FRC) are described in previous chapter. The experimental program carried out with these beams is presented in this chapter. These beams were subjected to compression, bending and shear tests. With these tests, intended to make a contribution to the knowledge of non-linear behaviour of reinforced concrete bar elements subjected to multiaxial stress states. The results obtained were used in the calibration of the developed numerical model, described in chapter 4.

Reinforced concrete structures, when subjected to multiaxial loads, have a nonlinear behaviour, especially after cracking starts. The characterization, either experimental or numerical, of the post-cracking behaviour of the elements that constitute such structures is still scarce.

In the first part of this chapter, the test system used is presented, describing the equipment, as well as the procedures adopted. The second part of this chapter is dedicated to the presentation and analysis of the results obtained.

### 3.2. Tests carried out

Different types of tests have been conducted.

- Compression tests, for the characterization of the compressive strength and Young's module of concrete.
- Tensile tests, for the characterization of the tensile strength of GFRP bars.

- Three-point notched beam bending tests (3PNBBT), for the characterization of the shear capacity and post cracking behaviour of fiber reinforced concrete (FRC).
- Four-point bending tests (4PBT) of a slab, for the characterization of the load – displacement diagram and consequently, bending resistance.

To control the displacement of the barycentric axis of the specimens during the tests, it's used two types of electric displacement transducers (LVDT's – Linear Voltage Displacement Transducer), which differ in the reading field: amplitude linear  $\pm 12.5$  mm and  $\pm 2.5$  mm, as shown in Figure 12.

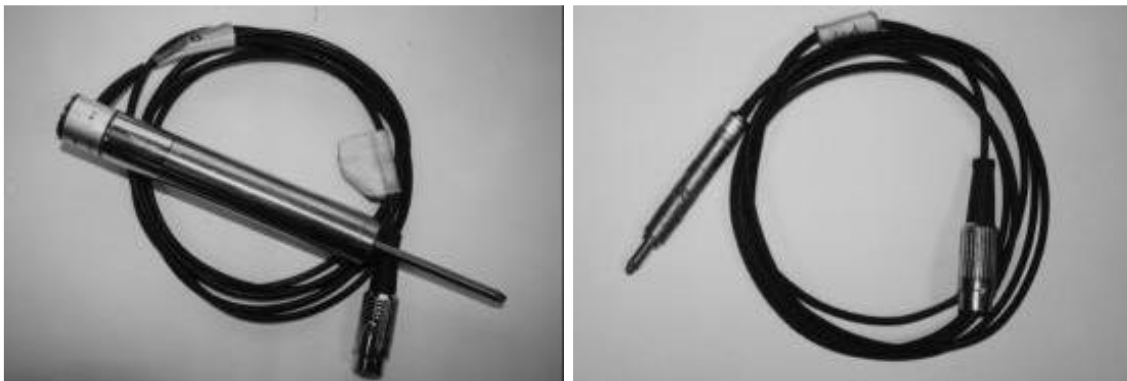


**Figure 12** - Electric displacement transducers: a)  $\pm 12.5$  mm; b)  $\pm 2.5$  mm.

### 3.2.1. Compression tests.

The compressive strength of the concrete is evaluated by the crushing with the press of standard specimens (cubic or cylindrical) obtained from the same material used for the other specimens during the casting (Figure 13).

In any case, before the test, the sample must be prepared by mechanical rectification. It consists in making the two surfaces of the cylinder perfectly flat, so that the applied compression is homogeneous on the whole surface of the specimen.



**Figure 13** – Specimen for compression test and mechanic press.

The specimen adopted for the test are cylindric and the dimension are 150x300, where the first number indicate the diameter of the specimen and the second one is the height (Figure 14). The total number of specimens tested are 5.

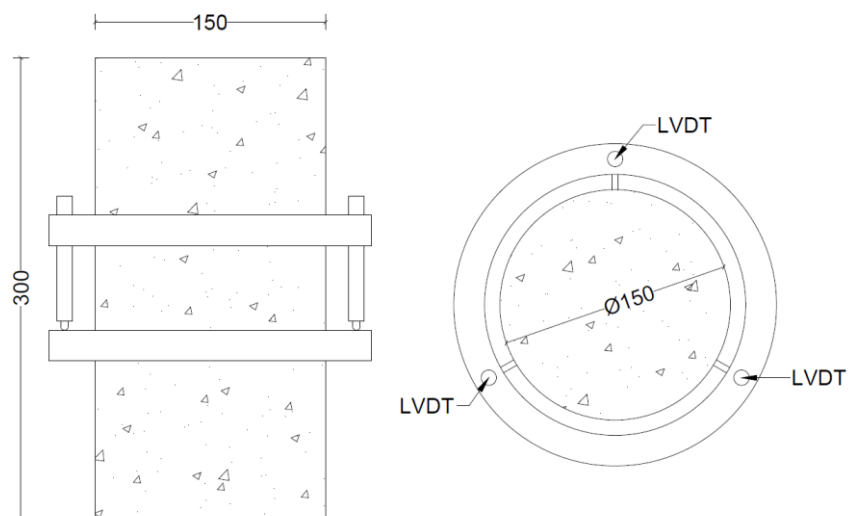


**Figure 14** – Dimension of the cylindric specimen and position of LVDTs.

The test is in displacement control and the results provided by them are the trend of the load during the test and the displacement associated with it. For these tests are not necessary to use the LVDTs, but is enough the displacement rated by the press.

The compressive strength value,  $f_c$ , is obtained after breaking the specimen using the Eq. (3.1).

$$f_c = \frac{F_{max}}{A_c} \quad \text{Eq. (3.1)}$$

where  $f_c$  is expressed in Mpa;  $F_{max}$  is the breaking load and  $A_c = 17662 \text{ mm}^2$  is the cross-section area of the specimen.

The LVDTs presented in these tests (Figure 14) are necessary for find the value of the Young's module. In this test a cyclic load is applied up to about the 30% of the maximum capacity of the specimen for 5 cycles (Figure 15).

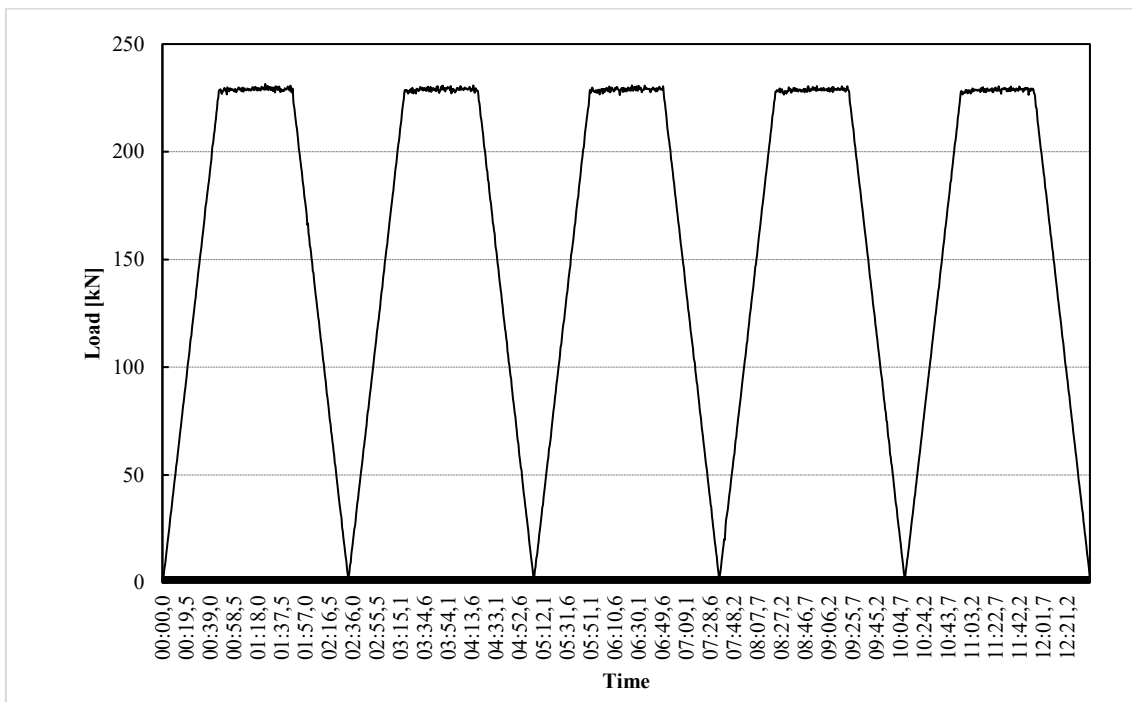


**Figure 15** – Loading in the time during the compression tests for the evaluation of Young's module.

The Young's module,  $E$ , is calculated as the ratio between the increases in tension,  $\Delta\sigma$ , and deformation,  $\Delta\varepsilon$ , both in loading and unloading phase recorded at the third cycle.

$$E = \frac{\Delta\sigma}{\Delta\varepsilon} \quad \text{Eq. (3.2)}$$

### 3.2.2. Tensile test

The tensile test on GFRP bars consists in subjecting the specimen to a tensile load applied with a certain amount speed of increase until it breaks, in order to determine the strength, elasticity and deformability (Figure 16).

In this test all the components of the 3D-SRT were examined, in particular bars of Ø5 and Ø3. The main properties that can be obtained from the test are the Young's module and the tensile strength of the bars.

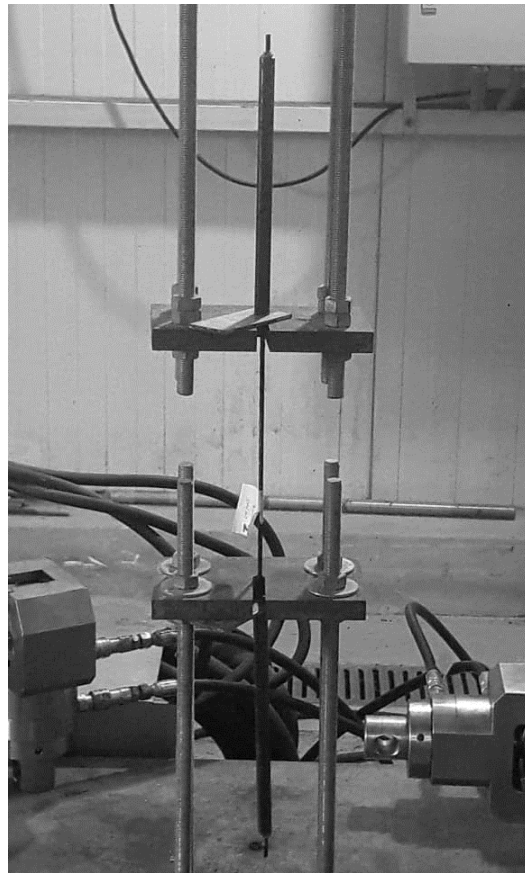


**Figure 16** – Tensile test for a GFRP bar.

The test is in displacement control and the results provided by them are the trend of the load during the test and the displacement associated with it. Adopting Eq. (3.3) can be obtained the tensile stress,  $\sigma$ , during the test.

$$\sigma = \frac{F}{A_{GFRP}} \quad \text{Eq. (3.3)}$$

where  $A_{GFRP}$  is the section area of the bar and F is the load applied.

Instead, the Eq. (3.4) is used to obtain the strain,  $\varepsilon$ .

$$\varepsilon = \frac{\Delta L}{L_0} \quad \text{Eq. (3.4)}$$

where  $\Delta L$  is the displacement of the bar during the test and  $L_0$  is the initial length of the specimen.

### 3.2.3. Three-point notched beam bending test (3PNBBT)

The specimens adopted for this test have dimensions 600x150x150 mm, in according to RILEM 162 TDF [12]. It has the configuration shown in Figure 17. The beam specimens were subjected to a three-point bending test configuration by using a servo-hydraulic actuator of 150 kN loading capacity under monotonic loading condition. The notch at the bottom of the specimen have dimension 5x25x150 and is situated in the middle of the span.

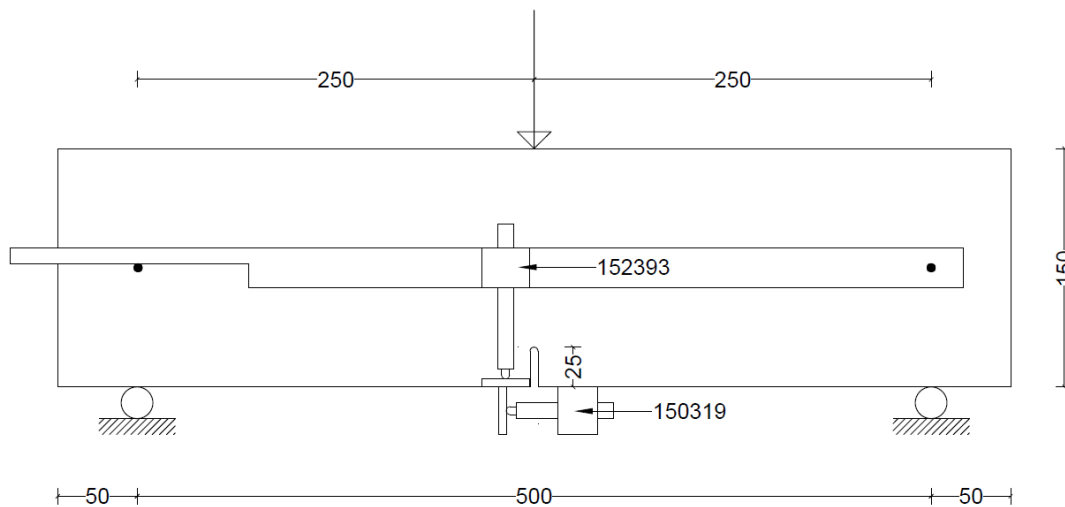


**Figure 17** – Schematic representation of position of LVDTs in the 3PNBBT (measures in mm).

The tests are displacement-controlled by imposing a speed of 0.01 mm/sec to the piston of the actuator. Three linear variable differential transducers (LVDTs) were installed on the specimen, according to the schematic representation in Table 2.



**Figure 18** - Position of LVDT in a mid-span in the 3PNBBT.



**Figure 19** – Position of LVDT between the crack in the 3PNBBT.

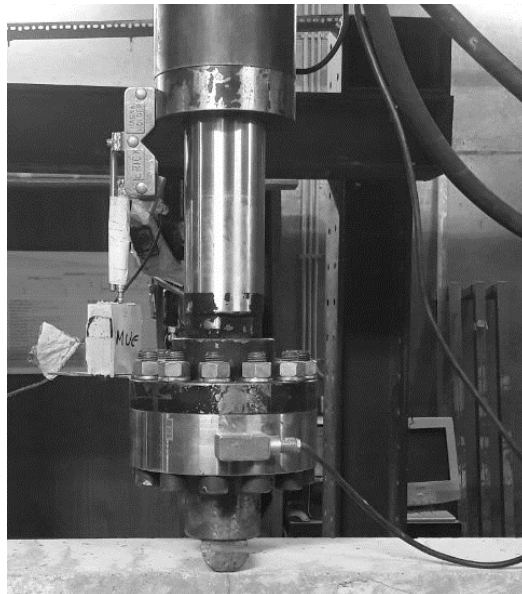


**Figure 20** – Position of LVDT on the actuator in the 3PNBBT.

**Table 2** - Description of position of LVDTs on three-point bending test.

<i>Serial number</i>	<i>Position</i>	<i>Main purpose</i>	<i>Figure</i>
152393	Mid span, vertical	Vertical displacement of mid span point	18
150319	Mid span, bottom, between the crack	Crack opening	19
176600	On the actuator	Vertical displacement of the press	20

### 3.2.4. Four-point bending test (4PBT)

For this test the specimen adopted is a slab of dimensions 700x350x100 mm (Figure 21). The beam specimens were subjected to a four-point bending test configuration using a servo-hydraulic actuator of 250 kN loading capacity under monotonic loading condition.

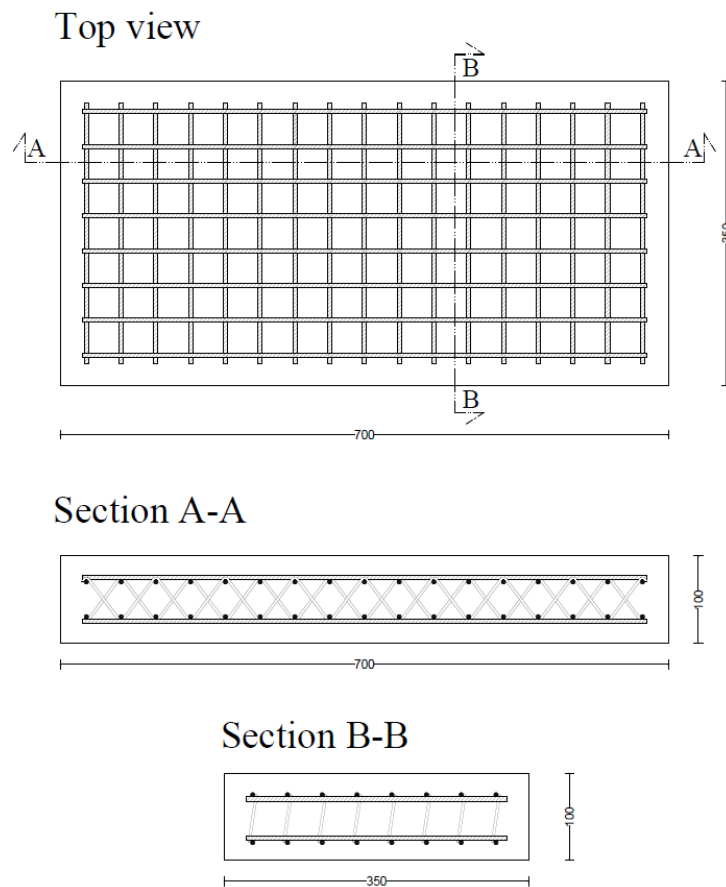


**Figure 21** - Sizes of the specimen for 4PBT.

The tests are displacement-controlled by imposing a speed of 0.01 mm/sec to the piston of the actuator. Four linear variable differential transducers (LVDTs) were installed along the span length of the slab and one LVDT was installed on the actuator, according to the schematic representation in Table 3.

In Figure 22 is shown the disposition of the LVDT's installed on the materials for measuring the strain during loading. The distance between the two loading points is 150 mm.

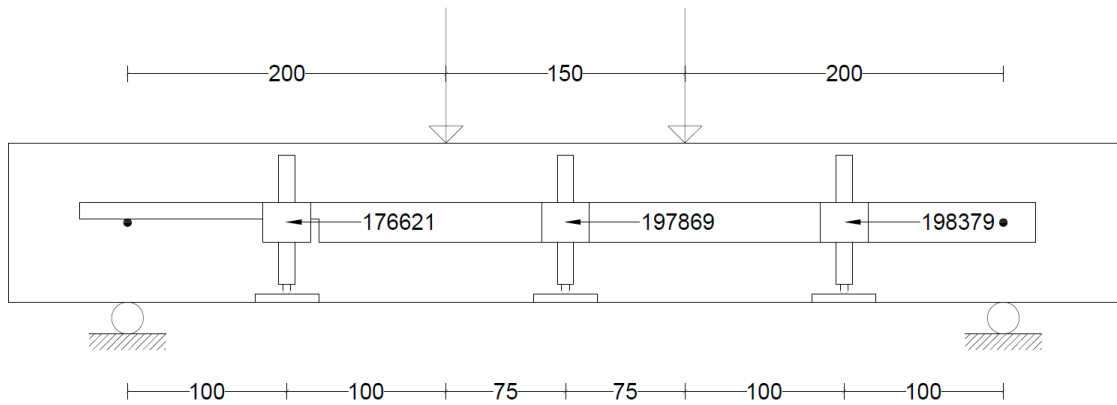


**Figure 22** – Schematic representation of position of LVDTs in the 4PB.

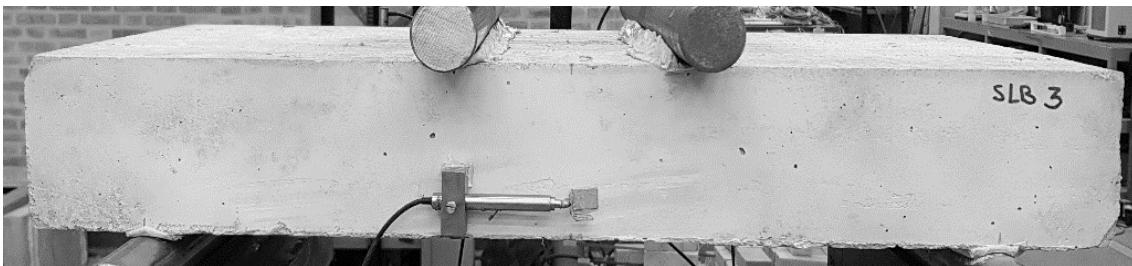


**Figure 23** – Position of horizontal LVDT on the slab in the 4PB.

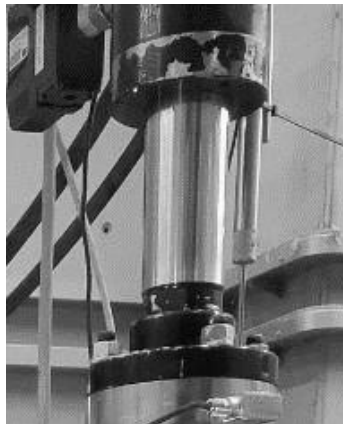


**Figure 24** – Position of LVDT on the actuator.

**Table 3** – Description of position of LVDTs.

<i>Serial number</i>	<i>Position</i>	<i>Main purpose</i>	<i>Figure</i>
197869	Mid span, vertical	Vertical displacement of mid span point	22
176621	Between the left support and force, vertical	Vertical displacement of left point	22
198379	Between the right support and force, vertical	Vertical displacement of right point	22
152466	Mid span, horizontal, 25 mm from bottom	Horizontal displacement of point	23
147586	On the actuator	Vertical displacement of the press	24

The three-dimensional reinforcement is composed in 3 main parts: the top grid, the bottom grid and the central bars. The top and the bottom grid are composed by GFRP bars with diameter of 5 mm and 35 mm distance between them, in both the directions (Figure 25). The central bars aim to confine all the reinforcement system, joining top and bottom grid.

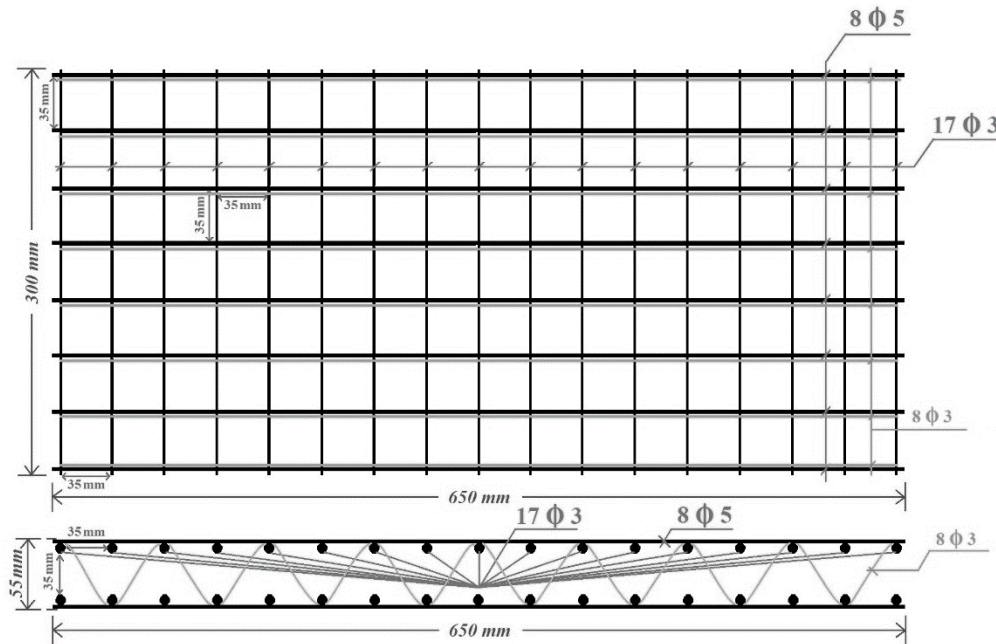


**Figure 25** - Dimensions of textile reinforcement in GFRP: a) Top view; b) Frontal view.

### 3.3. Results

#### 3.3.1. Compressive strength

For the characterization of the constitutive law of FRC, compression tests are executed as described in chapter 3.2.1. The number of tested specimens is 5, they have all the same size and come from the same casting used also to create the specimens for the other tests. The results of these tests are shown in Figure 26.

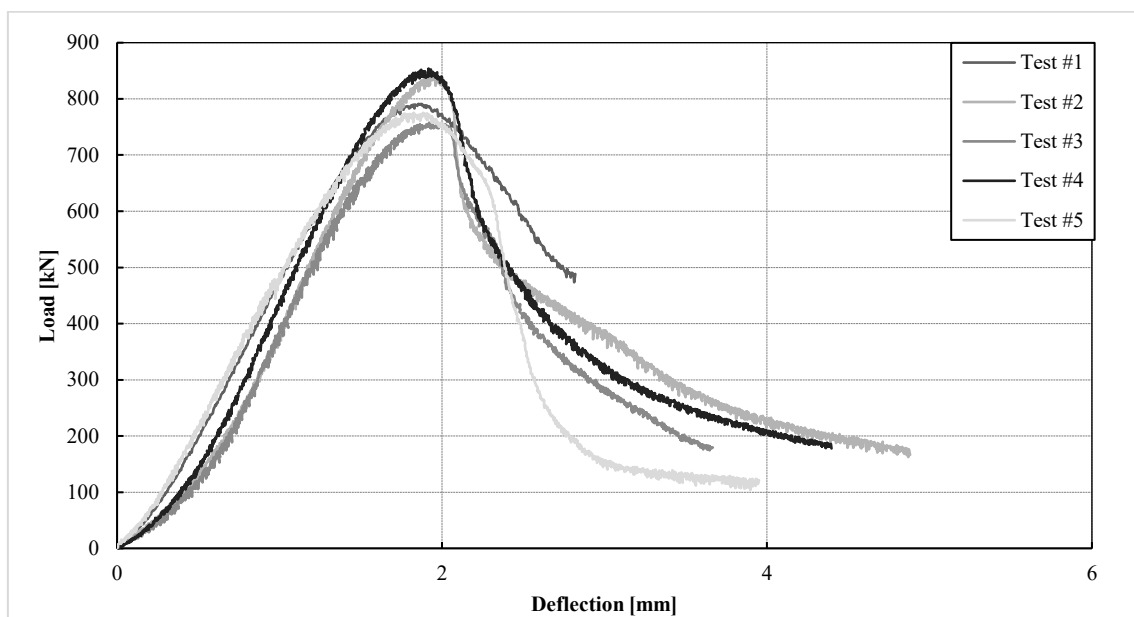


**Figure 26** – Results of compression test of the FRC specimens.

From the results obtained in this way it is possible to obtain the maximum compressive strength using Eq. (3.1) The values thus obtained are shown in table 4.

**Table 4** – Values of maximum compressive strength of the specimens.

<i>Test Number</i>	<i>F<sub>max</sub> [kN]</i>	<i>f<sub>c</sub> [Mpa]</i>
1	796.6	45.078
2	843.4	47.727
3	757.6	42.871
4	855.4	48.406
5	783	44.309

The medium compressive strength of the FRC was obtained from the values in table 4, as described in Eq. (3.5).

$$f_{cm} = \frac{\sum_{i=1}^n f_c}{n} = 45.68 \text{ Mpa} \quad \text{Eq. (3.5)}$$

where  $n$  is the number of the specimens tested.

For the determination of the modulus of young, the tested specimens are 4 because the first one was used to get an idea of the maximum compressive strength, in order to be able to reach 30% of it to carry out the tests correctly.

Through suitable software, it is possible to extrapolate the value of Young's module. Table 5 shows the average values of the modulus of elasticity obtained in the tests.

**Table 5** - Values of Young's module of the specimens.

<i>Test Number</i>	<i>E<sub>c</sub> [Mpa]</i>
1	34563
2	35160
3	34046
4	34385

The medium Young's module of the FRC was obtained from the values in table 5, as described in Eq. (3.6).

$$E_{cm} = \frac{\sum_{i=1}^n E_c}{n} = 34700 \text{ Mpa} \quad \text{Eq. (3.6)}$$

where  $n$  is the number of the specimens tested.

### 3.3.2. Tensile strength

For the characterization of the constitutive law of GFRP bars, tensile tests are executed as described in chapter 3.2.2.

The samples tested are 4 with a diameter of 5 (Ø5) mm and 4 with a diameter of 3 mm (Ø3). The results of these tests are shown in Figure 27.

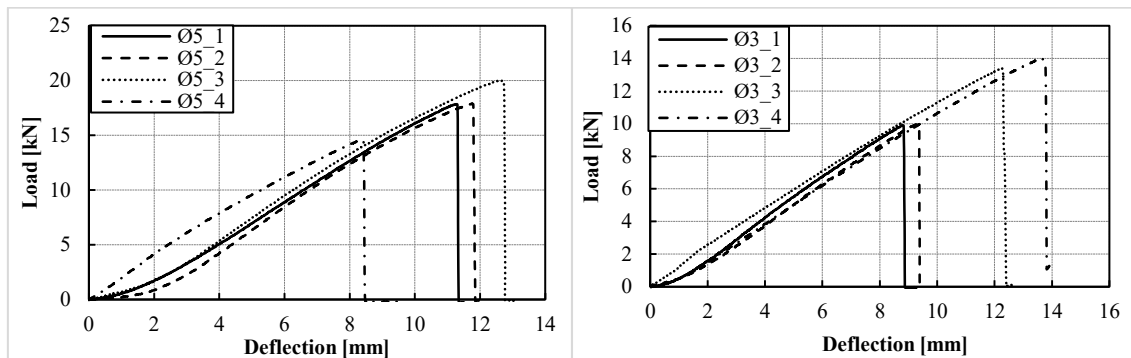


**Figure 27** – Load-Deflection diagram: a) bars of Ø5; b) bars of Ø3.

From the results obtained, using Eq. (3.3) and Eq. (3.4) is possible to find stress and strain respectively. Therefore, it is possible to create the stress-strain diagram of the specimens for the bars Ø5 and Ø3, as shown in Figure 28 and Figure 29, respectively.

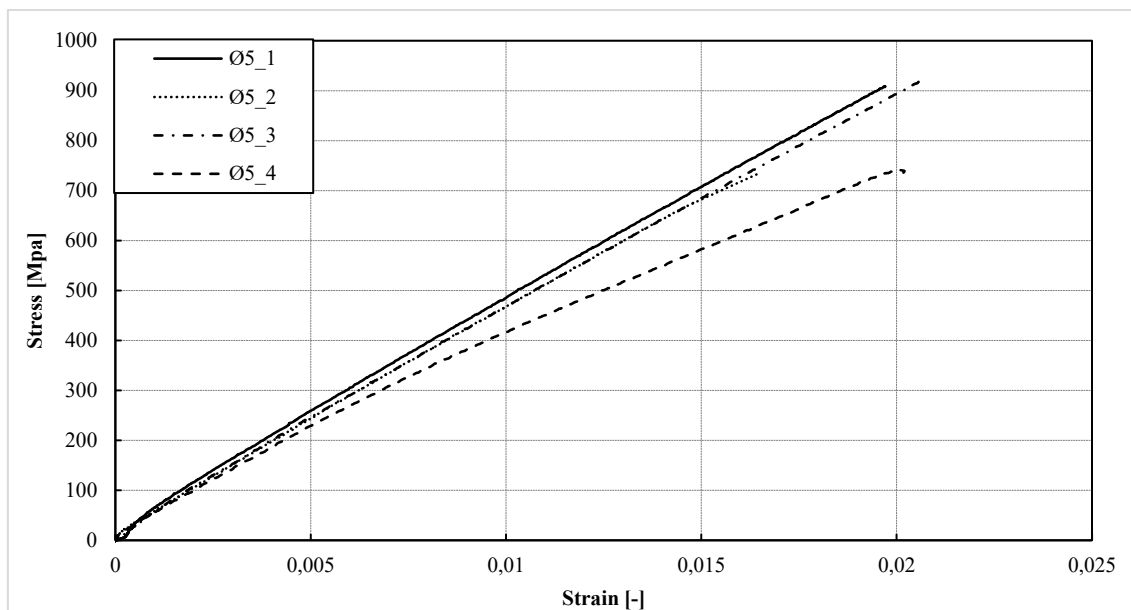


**Figure 28** – Stress-Strain diagram for Ø3 bars in GFRP.

Table 6 shows the values of the tensile strength and the elastic modulus of each specimen regarding Ø5 bars.

**Table 6** - Values of tensile strength and Young's module of Ø5 bars in GFRP

<i>Test Number</i>	$\sigma_{max}$ [Mpa]	<i>E</i> [Mpa]
1	908.76	45660
2	732.49	44620
3	917.57	44200
4	741.31	35610
Average	825.03	42520

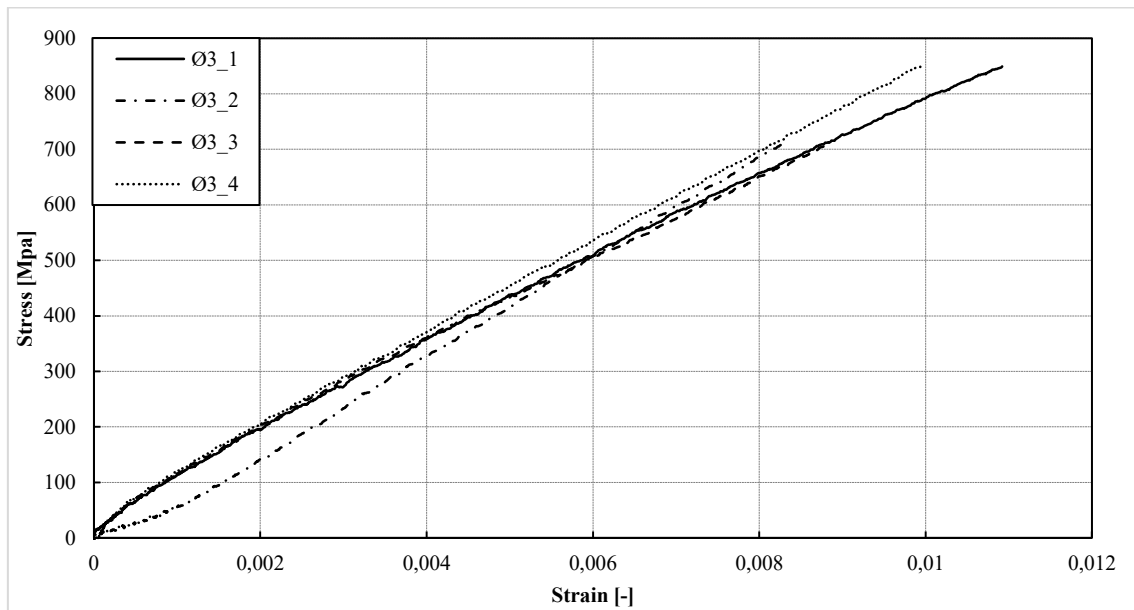


**Figure 29** - Stress-Strain diagram for Ø5 bars in GFRP.

Table 7 shows the values of the tensile strength and the elastic modulus of each specimen regarding Ø3 bars.

**Table 7** - Values of tensile strength and Young's module of Ø3 bars in GFRP

<i>Test Number</i>	$\sigma_{max}$ [Mpa]	<i>E</i> [Mpa]
1	849.29	77590
2	708.05	91030
3	708.50	75050
4	850.23	81990
Average	825.03	42520

### 3.3.3. Crack patterns and failure modes

For the characterization of FRC, 3-point notched beam bending tests (3PNBBT) are executed according to EN 14651 [10]. From the execution of 3PNBBT, it is possible to evaluate the post-cracking tensile strength of FRC. The test setup and typical load vs. crack mouth opening displacement (CMOD) relationship are presented in Figure 4. Based on the force values,  $F_j (j = 1,2,3,4)$  corresponding to specific values of CMOD, the residual flexural tensile strength,  $f_{Rj}$ , is determined from Eq. (3.7).

$$f_{Rj} = \frac{3 \cdot F_j \cdot l}{2 \cdot b \cdot h_{sp}^2} \quad \text{Eq. (3.7)}$$

where  $l$  is the span length of the test beam;  $b$  is the width of the specimen's cross section; and  $h_{sp}$  is the distance between the notch tip and the beam top face. In the Table 8 are showed the geometric values adopted.

**Table 8** – Geometric values of specimens in the 3PNBBT.

$l$	500 mm
$b$	150 mm
$h_{sp}$	125 mm

In the execution of 3PNBBT the midspan deflection ( $\delta$ ) of the beams is, usually, also recorded, and the following average relationship between  $\delta$  and CMOD can be used in the post-peak region of the load-CMOD curve [10].

$$\delta [mm] = 0.85 \cdot CMOD + 0.04 \quad \text{Eq. (3.8)}$$

In the Table 9 is presented the conversion of the  $CMOD_j = (j = 1,2,3,4)$  to  $\delta$ .

**Table 9** – Relationship between CMOD and  $\delta$  [10]

$j$	CMOD [mm]	$\delta$ [mm]
1	0.50	0.47
2	1.50	1.32
3	2.50	2.17
4	3.50	3.02

The LVDT number 150319 in the 3PNBBT have the purpose to measure the crack opening during the tests (Figure 19).

In the Figure 30 is shown the diagram load – crack opening of the specimen during the 3PNBBT.

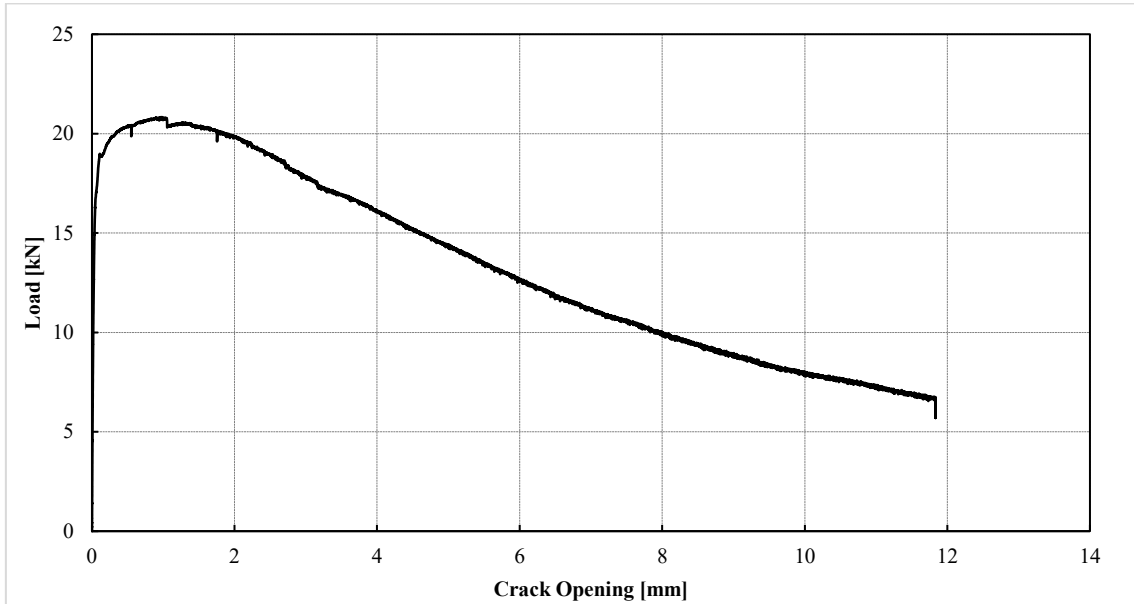


**Figure 30** – Diagram Load–crack opening.

Is possible to compare the displacement at the mid span (LVDT 152393) with the crack opening due to LVDT 150319 and the CMOD obtained inverting the Eq. (3.8).

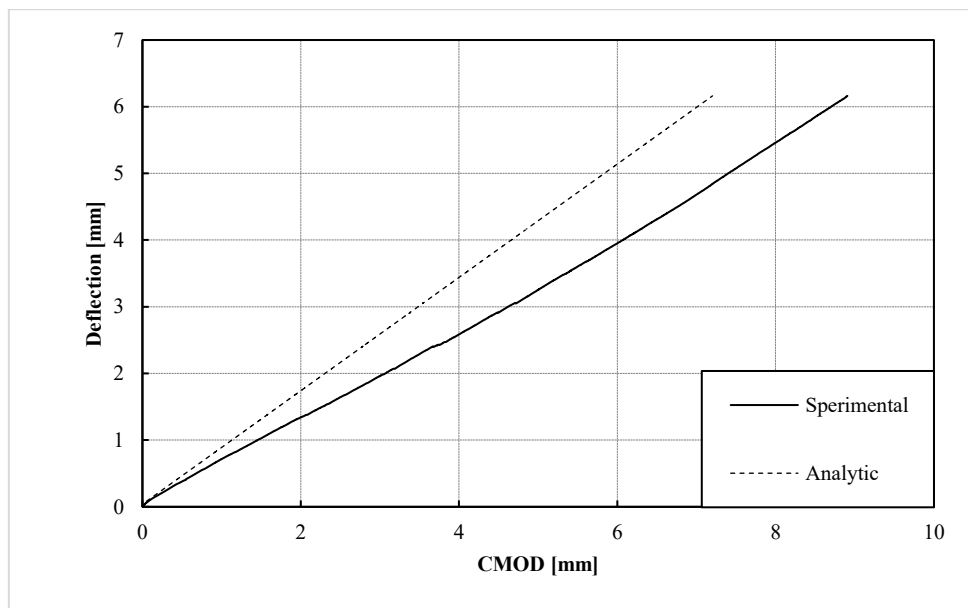


**Figure 31** – Deflection – CMOD diagram.

Using Eq. (3.7), it's possible to find the residual flexural tensile strength,  $f_{Rj}$ . The results are shown in Table 10.

**Table 10** – values of post-cracking tensile strength.

$f_{R1}$	6.56 Mpa
$f_{R2}$	6.35 Mpa
$f_{R3}$	5.50 Mpa
$f_{R4}$	4.78 Mpa

### 3.3.4. Flexural capacity

For evaluate the flexural capacity it was tested 4 specimens with the four-point bending test (4PBT). By this test is possible to obtain the Load-deflection diagram shown in Figure 32.

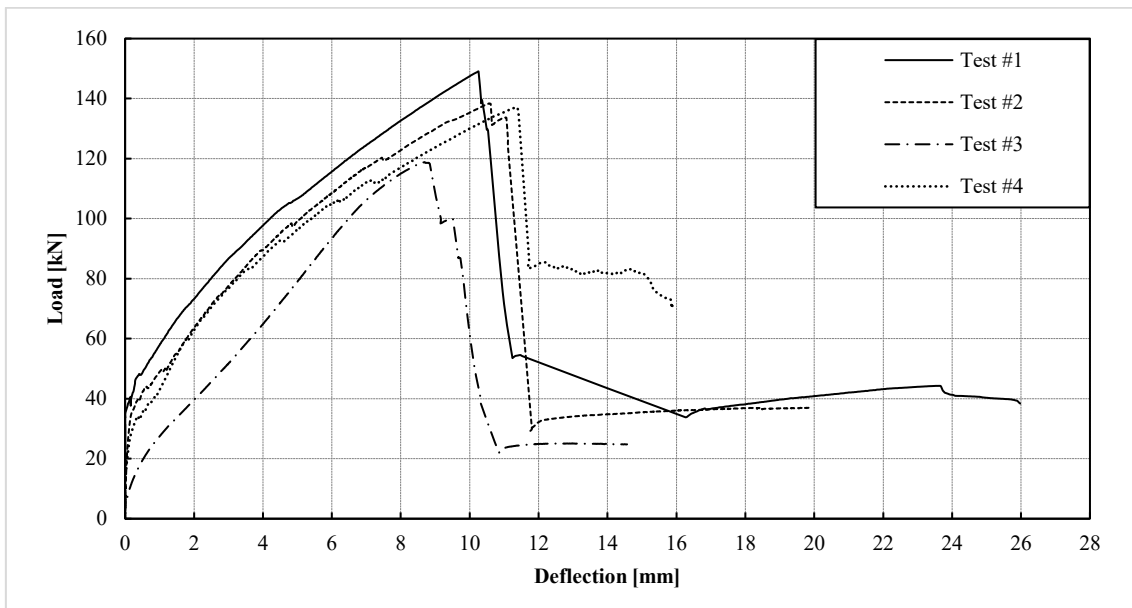


**Figure 32** – Load-deflection diagram of FPBT.

With this graphic is possible to obtain the following values:

- Maximum force applied,  $F_{max}$ ;
- Peak displacement,  $d_F$ , associated at the maximum force applied;
- Maximum bending resistance,  $M_{max}$ , calculated through Eq. (3.9);

$$M_{max} = \frac{F_{max}}{2} \cdot b \quad \text{Eq. (3.9)}$$

where  $b$  is the distance from the force and the support, equal to 200 mm.

- Maximum shear applied,  $V_{max}$ , calculated through Eq. (3.10);

$$V_{max} = \frac{F_{max}}{2} \quad \text{Eq. (3.10)}$$

In Table 11 are shown all the main values previously listed.

**Table 11** – Values of maximum capacity of the specimen in 4PBT.

Test number	$F_{max}$ [kN]	$d_F$ [mm]	$M_{max}$ [kNm]	$V_{max}$ [kN]
1	149.05	10.25	14.90	74.52
2	138.40	10.57	13.84	69.20
3	118.80	8.68	11.88	59.4
4	137.10	11.36	13.71	68.55
Average	135.84	10.21	13.58	67.92

To have an idea if the test was performed correctly, i.e. with loads and geometry as symmetrical as possible in order to cancel the presence of cutting in the central part of the specimen, it is possible to compare the left and right LVDTs, number 176621 and 19379 respectively (Figure 22). Figures 33 and 34 show the responses of the two LVDTs during the tests.

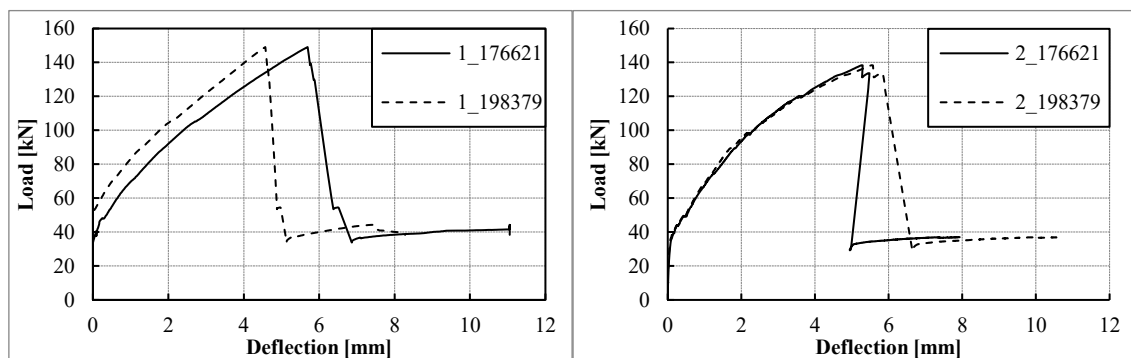


**Figure 33** - Load-deflection diagram during FPBT supplied by external LVDTs: a) Test n°1; b) Test N°2.

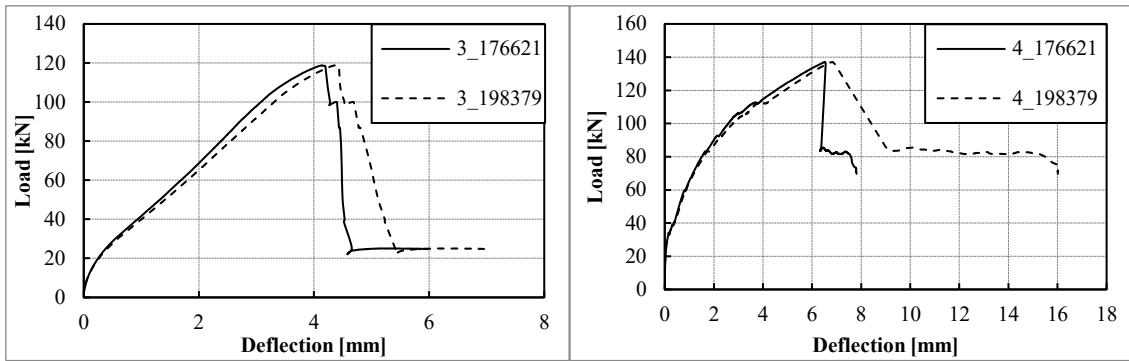


**Figure 34** - Load-deflection diagram during FPBT supplied by external LVDTs: a) Test n°3; b) Test N°4.

In the four-point bending test (4PBT) is not possible to evaluate the crack opening by a LVDT because it's not known where will appear the cracks during the test, but it's possible to sign the moment and where they will appear (Figure 35).

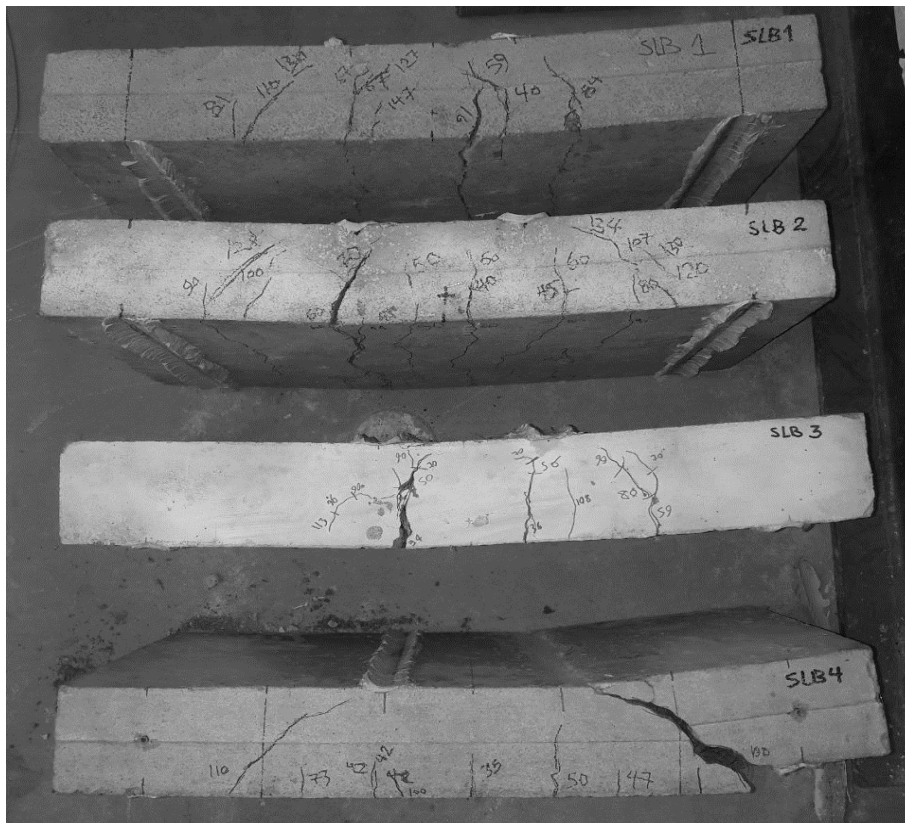


**Figure 35** - Specimens collapsed after 4PBT.

# Chapter 4

---

## 4. Analytic Model

### 4.1. Model of 3D Timoshenko's beam

The structures, when subjected to certain series of stresses, show a non-linear behaviour after a certain level of strain. This non-linear behaviour derives from the consideration of second order deformations and/or the fact that the materials have not linear constitutive laws, designating nonlinear geometric behaviour as the first case and material nonlinear behaviour the second.

Timoshenko's prismatic model based on the finite element method (FEM). This model considers the behaviour of the various materials that constitute the section as it is discretized into that each mesh is given a law that characterizes material behaviour of this element.

Considering a curved part defined in a global axis system  $g_i(g_1, g_2, g_3)$ , by its guideline  $e$  and the geometry of the different planar cross sections of area  $A^{(e)}$  and orthogonal to  $e$  (Figure 36). First, it is necessary to define the various systems coordinates:

- Global coordinates system  $g_i(g_1, g_2, g_3)$ : cartesian coordinate system used to define structure geometry in the space, node displacements, stiffness matrix and nodal force vector of the structure.
- Normalized coordinates system -  $s_1$ : coordinate system that underpins the definition of element shape functions. The normalized coordinate  $s_1$  ranges from  $-1$  to  $+1$  along the axis of the element, which coincides with the line containing the centres of gravity of the part sections.
- Local coordinates system  $l_i(l_1, l_2, l_3)$ : cartesian coordinate system defined locally in any section of the element. The definition of this referential at numerical

integration points (sampling points) serves as a reference for defining stress and strain states.

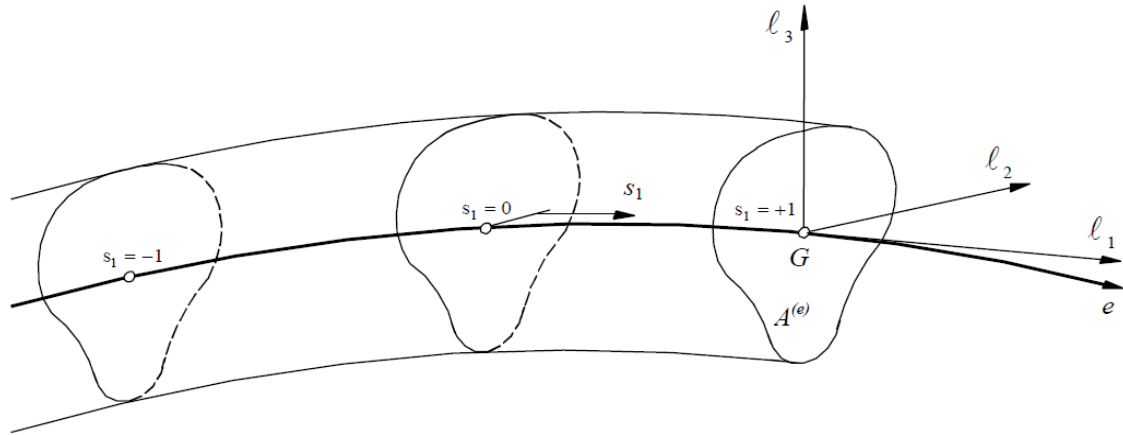


**Figure 36** – Timoshenko beam in the space.

#### 4.1.1. Linear static analysis model

The displacement field of a generic point in the section is defined by the following expressions:

$$\begin{cases} u_1^l(x_1^l, x_2^l, x_3^l) = u_{1G}^l(x_1^l) + x_3^l \cdot \theta_2^l(x_1^l) - x_2^l \cdot \theta_3^l(x_1^l) \\ u_2^l(x_1^l, x_2^l, x_3^l) = u_{2G}^l(x_1^l) - x_3^l \cdot \theta_1^l(x_1^l) \\ u_3^l(x_1^l, x_2^l, x_3^l) = u_{3G}^l(x_1^l) + x_2^l \cdot \theta_1^l(x_1^l) \end{cases} \quad \text{Eq. (4.1)}$$

where the centre of shear coincides with the barycentre [13].  $u_{iG}^l$  is the  $i$ -th local displacement of the barycentre of the section;  $x_i^l$  are the  $i$ -th coordinates of the generic point  $P$  of the section and  $\theta_i^l$  are the rotations around the  $i$ -th axis (Figure 37).

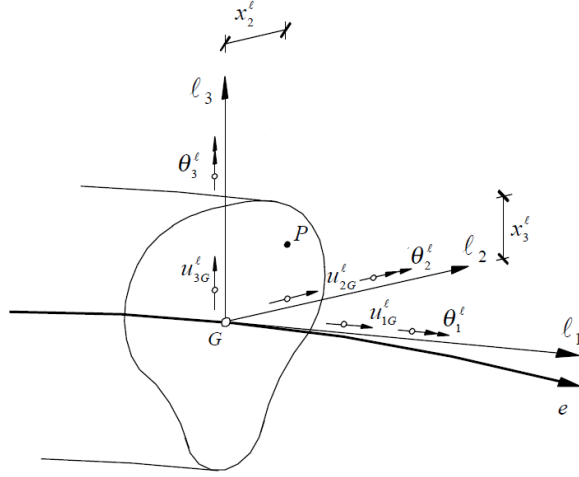


Figure 37 – Local coordinates.

In fact, the local and global displacement vectors are, respectively, the following components.

$$\{U^l\} = [u_{1G}^l \ u_{2G}^l \ u_{3G}^l \ \theta_1^l \ \theta_2^l \ \theta_3^l]^T \quad \text{Eq. (4.2)}$$

$$\{U^g\} = [u_{1G}^g \ u_{2G}^g \ u_{3G}^g \ \theta_1^g \ \theta_2^g \ \theta_3^g]^T \quad \text{Eq. (4.3)}$$

Consequently, the local and global vector of velocity are defined in Eq. (4.3) and Eq. (4.4), respectively.

$$\{\dot{U}^l\} = \left[ \frac{du_{1G}^l}{dt} \ \frac{du_{2G}^l}{dt} \ \frac{du_{3G}^l}{dt} \ \frac{d\theta_1^l}{dt} \ \frac{d\theta_2^l}{dt} \ \frac{d\theta_3^l}{dt} \right]^T = [\dot{u}_{1G}^l \ \dot{u}_{2G}^l \ \dot{u}_{3G}^l \ \dot{\theta}_1^l \ \dot{\theta}_2^l \ \dot{\theta}_3^l]^T \quad \text{Eq. (4.3)}$$

$$\{\dot{U}^g\} = \left[ \frac{du_{1G}^g}{dt} \ \frac{du_{2G}^g}{dt} \ \frac{du_{3G}^g}{dt} \ \frac{d\theta_1^g}{dt} \ \frac{d\theta_2^g}{dt} \ \frac{d\theta_3^g}{dt} \right]^T = [\dot{u}_{1G}^g \ \dot{u}_{2G}^g \ \dot{u}_{3G}^g \ \dot{\theta}_1^g \ \dot{\theta}_2^g \ \dot{\theta}_3^g]^T \quad \text{Eq. (4.4)}$$

The local and global vector of acceleration are defined in Eq. (4.5) and Eq. (4.6), respectively.

$$\{\ddot{U}^l\} = \left[ \frac{d\dot{u}_{1G}^l}{dt} \ \frac{d\dot{u}_{2G}^l}{dt} \ \frac{d\dot{u}_{3G}^l}{dt} \ \frac{d\dot{\theta}_1^l}{dt} \ \frac{d\dot{\theta}_2^l}{dt} \ \frac{d\dot{\theta}_3^l}{dt} \right]^T = [\ddot{u}_{1G}^l \ \ddot{u}_{2G}^l \ \ddot{u}_{3G}^l \ \ddot{\theta}_1^l \ \ddot{\theta}_2^l \ \ddot{\theta}_3^l]^T \quad \text{Eq. (4.5)}$$

$$\{\ddot{U}^g\} = \left[ \frac{d\dot{u}_{1G}^g}{dt} \ \frac{d\dot{u}_{2G}^g}{dt} \ \frac{d\dot{u}_{3G}^g}{dt} \ \frac{d\dot{\theta}_1^g}{dt} \ \frac{d\dot{\theta}_2^g}{dt} \ \frac{d\dot{\theta}_3^g}{dt} \right]^T = [\ddot{u}_{1G}^g \ \ddot{u}_{2G}^g \ \ddot{u}_{3G}^g \ \ddot{\theta}_1^g \ \ddot{\theta}_2^g \ \ddot{\theta}_3^g]^T \quad \text{Eq. (4.6)}$$

The Eq. (4.1) can be written in the matrix formulation.

$$\{u^l\} = \begin{bmatrix} u_1^l \\ u_2^l \\ u_3^l \end{bmatrix} = \begin{bmatrix} 1 & 0 & 0 & 0 & x_3^l & -x_2^l \\ 0 & 1 & 0 & -x_3^l & 0 & 0 \\ 0 & 0 & 1 & x_2^l & 0 & 0 \end{bmatrix} \begin{bmatrix} u_{1G}^l \\ u_{2G}^l \\ u_{3G}^l \\ \theta_1^l \\ \theta_2^l \\ \theta_3^l \end{bmatrix} = [R]\{U^l\} \quad \text{Eq. (4.7)}$$

The matrix  $[R]$  does not depend on the time. Therefore, the field of velocity and the field of acceleration are defined in Eq. (4.8) and Eq. (4.9), respectively.

$$\{\dot{u}^l\} = \begin{bmatrix} \dot{u}_1^l(x_1^l, x_2^l, x_3^l) \\ \dot{u}_2^l(x_1^l, x_2^l, x_3^l) \\ \dot{u}_3^l(x_1^l, x_2^l, x_3^l) \end{bmatrix} = [R]\{\dot{U}^l\} \quad \text{Eq. (4.8)}$$

$$\{\ddot{u}^l\} = \begin{bmatrix} \ddot{u}_1^l(x_1^l, x_2^l, x_3^l) \\ \ddot{u}_2^l(x_1^l, x_2^l, x_3^l) \\ \ddot{u}_3^l(x_1^l, x_2^l, x_3^l) \end{bmatrix} = [R]\{\ddot{U}^l\} \quad \text{Eq. (4.9)}$$

Is possible switch from the local to the global reference of the displacements, through the transformation matrix,  $[T^{lg}]$  (Eq. 4.10).

$$\{U^g\} = [T^{lg}]\{U^l\} \quad \text{Eq. (4.10)}$$

The vector of the deformations in the local system is defined by Eq. (4.11) [13].

$$\{\varepsilon^l\} = \begin{bmatrix} \varepsilon_1^l \\ \gamma_{12}^l \\ \gamma_{13}^l \end{bmatrix} = \begin{bmatrix} 1 & 0 & 0 & 0 & x_3^l & -x_2^l \\ 0 & 1 & 0 & -x_3^l & 0 & 0 \\ 0 & 0 & 1 & x_2^l & 0 & 0 \end{bmatrix} \begin{bmatrix} \frac{\partial u_{1G}^l}{\partial x_1^l} \\ \frac{\partial u_{2G}^l}{\partial x_1^l} - \theta_3^l \\ \frac{\partial u_{3G}^l}{\partial x_1^l} + \theta_2^l \\ \frac{\partial \theta_1^l}{\partial x_1^l} \\ \frac{\partial \theta_2^l}{\partial x_1^l} \\ \frac{\partial \theta_3^l}{\partial x_1^l} \end{bmatrix} = [R]\{\bar{\varepsilon}^l\} \quad \text{Eq. (4.11)}$$

The relationship between the stress and strain is established by means of the constitutive matrix,  $D$  defined in Eq. (4.12), in the local system (Figure 38).

$$\{\sigma^l\} = \begin{bmatrix} \sigma_1^l \\ \tau_{12}^l \\ \tau_{13}^l \end{bmatrix} = [D]\{\varepsilon^l\} = \begin{bmatrix} E & 0 & 0 \\ 0 & G_{12} & 0 \\ 0 & 0 & G_{13} \end{bmatrix} \begin{bmatrix} \varepsilon_1^l \\ \gamma_{12}^l \\ \gamma_{13}^l \end{bmatrix} \quad \text{Eq. (4.12)}$$

where  $E$  is the longitudinal elastic modulus of the material;  $G_{12}$  and  $G_{13}$  are the modules of transversal elasticity of the material in the  $l_1l_2$  and  $l_1l_3$  planes, respectively.

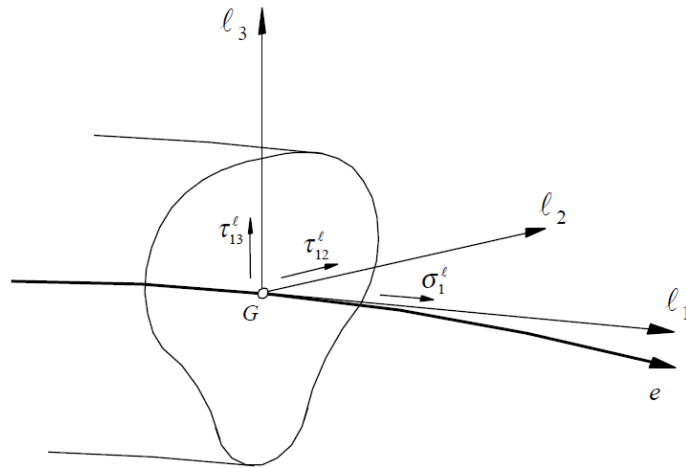


**Figure 38 - Tensions**

The components of stresses in a section of the element, in the local system, are the following (Figure 39).

$$\{\bar{\sigma}^l\} = [N^l \ V_2^l \ V_3^l \ M_1^l \ M_2^l \ M_3^l]^T \quad \text{Eq. (4.13)}$$

where  $N^l$  is the axial force;  $V_2^l$  and  $V_3^l$  are the cutting force according to the  $l_2$  axis and  $l_3$  axis;  $M_1^l$  is the torsional moment;  $M_2^l$  and  $M_3^l$  are the bending moment according to the  $l_2$  and  $l_3$  axis; defined by Eq. (4.14).

$$N^l = \int_A \sigma_1^l dA \quad \text{Eq. (4.14a)}$$

$$V_2^l = \int_A \tau_{12}^l dA \quad \text{Eq. (4.14b)}$$

$$V_3^l = \int_A \tau_{13}^l dA \quad \text{Eq. (4.14c)}$$

$$M_1^l = \int_A (-\tau_{12}^l \cdot x_3^l + \tau_{13}^l \cdot x_2^l) dA \quad \text{Eq. (4.14d)}$$

$$M_2^l = \int_A \sigma_1^l \cdot x_3^l dA \quad \text{Eq. (4.14e)}$$

$$M_3^l = - \int_A \sigma_1^l \cdot x_2^l dA \quad \text{Eq. (4.14f)}$$

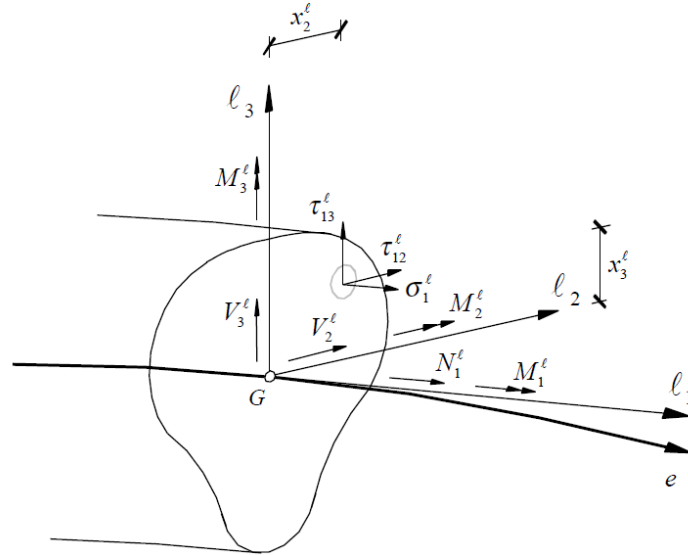


**Figure 39** - Stresses in the section of a Timoshenko element.

The Eq. (4.14) can be write in the following form.

$$\{\bar{\sigma}^l\} = \int_A \begin{bmatrix} 1 & 0 & 0 \\ 0 & 1 & 0 \\ 0 & 0 & 1 \\ 0 & -x_3^l & x_2^l \\ x_3^l & 0 & 0 \\ -x_2^l & 0 & 0 \end{bmatrix} \begin{bmatrix} \sigma_1^l \\ \tau_{12}^l \\ \tau_{13}^l \end{bmatrix} dA = \int_A [R]^T \{\sigma^l\} dA \quad \text{Eq. (4.15)}$$

Replacing Eq. (4.11) and Eq. (4.12) into Eq. (4.15) it results the following expression.

$$\{\bar{\sigma}^l\} = \int_A [R]^T [D] \{\varepsilon^l\} dA = \int_A [R]^T [D] [R] \{\bar{\varepsilon}^l\} dA \quad \text{Eq. (4.16)}$$

where the matrix product is:

$$[\bar{D}^l] = \int_A [R]^T [D] [R] dA = \quad \text{Eq. (4.17a)}$$

$$= \int_A \begin{bmatrix} E & 0 & 0 & 0 & x_3^l E & -x_2^l E \\ 0 & G_{12} & 0 & -x_3^l G_{12} & 0 & 0 \\ 0 & 0 & G_{13} & x_2^l G_{13} & 0 & 0 \\ 0 & -x_3^l G_{12} & x_2^l G_{13} & x_3^{l^2} G_{12} + x_2^{l^2} G_{13} & 0 & 0 \\ x_3^l E & 0 & 0 & 0 & x_3^{l^2} E & -x_2^l x_3^l E \\ -x_2^l E & 0 & 0 & 0 & -x_2^l x_3^l E & x_2^{l^2} E \end{bmatrix} dA \quad \text{Eq. (4.17b)}$$

Starting from the hypothesis that the material of element is isotropic ( $E = Cost.$ ), solving the integral separately, it obtained the results in Eq. (4.18).

$$\int_A E dA = EA \quad \text{Eq. (4.18a)}$$

$$\int_A G_{12} dA = \alpha_{12} GA = GA_2^* \quad \text{Eq. (4.18b)}$$

$$\int_A G_{13} dA = \alpha_{13} GA = GA_3^* \quad \text{Eq. (4.18c)}$$

$$\int_A x_3^l E dA = ES_2^l \quad \text{Eq. (4.18d)}$$

$$\int_A x_2^l E dA = ES_3^l \quad \text{Eq. (4.18e)}$$

$$\int_A x_3^l G_{12} dA = GS_2^* \quad \text{Eq. (4.18f)}$$

$$\int_A x_2^l G_{13} dA = GS_3^* \quad \text{Eq. (4.18g)}$$

$$\int_A (x_3^{l_2^2} G_{12} + x_2^{l_2^2} G_{13}) dA = GI_1^l \quad \text{Eq. (4.18h)}$$

$$\int_A x_3^{l_2^2} E dA = EI_2^l \quad \text{Eq. (4.18i)}$$

$$\int_A x_2^{l_2^2} E dA = EI_3^l \quad \text{Eq. (4.18l)}$$

$$\int_A x_2^l x_3^l E dA = EI_{23}^l \quad \text{Eq. (4.18m)}$$

where  $A_2^*$  and  $A_3^*$  are the reduced areas of shear;  $S_2^*$  and  $S_3^*$  are the statics moment around the  $l_2$  and  $l_3$  axes;  $I_1^l$ ,  $I_2^l$  and  $I_3^l$  are the moment of inertia around the  $l_1$ ,  $l_2$  and  $l_3$  respectively;  $I_{23}^l$  is the centrifugal moment of inertia of the section. If the section is doubly symmetrical  $S_2 = S_3 = 0$  and  $I_{23} = 0$ . Then the matrix  $\bar{D}$  is defined by Eq. (4.19).

$$[\bar{D}^l] = \int_A [R]^T [D] [R] dA = \begin{bmatrix} EA & 0 & 0 & 0 & 0 & 0 \\ 0 & GA_2^* & 0 & 0 & 0 & 0 \\ 0 & 0 & GA_3^* & 0 & 0 & 0 \\ 0 & 0 & 0 & GI_1^l & 0 & 0 \\ 0 & 0 & 0 & 0 & EI_2^l & 0 \\ 0 & 0 & 0 & 0 & 0 & EI_3^l \end{bmatrix} \quad \text{Eq. (4.19)}$$

The matrix in the Eq. (4.19) can be subdivided in submatrix according to the structural behaviour.

$$[\bar{D}^l] = \begin{bmatrix} \bar{D}_a & 0 & 0 & 0 \\ 0 & [\bar{D}_s] & 0 & 0 \\ 0 & 0 & \bar{D}_t & 0 \\ 0 & 0 & 0 & [\bar{D}_f] \end{bmatrix} \quad \text{Eq. (4.20)}$$

where  $\bar{D}_a$ ,  $[\bar{D}_s]$ ,  $\bar{D}_t$ ,  $[\bar{D}_f]$ , are the submatrix associated to axial, shear, torsion and flexural stiffness, respectively.

$$\bar{D}_a = EA \quad \text{Eq. (4.21a)}$$

$$[\bar{D}_s] = \begin{bmatrix} GA_2^* & 0 \\ 0 & GA_3^* \end{bmatrix} \quad \text{Eq. (4.21b)}$$

$$\bar{D}_t = GI_1^l \quad \text{Eq. (4.21c)}$$

$$[\bar{D}_f] = \begin{bmatrix} EI_2^l & 0 \\ 0 & EI_3^l \end{bmatrix} \quad \text{Eq. (4.21d)}$$

In the Timoshenko formulation, the distribution of shear stresses  $\tau_{12}$  and  $\tau_{13}$  is considered constant through the cross section. This fact stems from the assumption that the sections the cross sections remain flat after deformation, which in reality does not happen distortions occur in the section. So, to take these distortions into account, and consequently a non-constant distribution of the stresses throughout the section, the section area is multiplied by coefficients  $\alpha_{12}$  and  $\alpha_{13}$  respectively. These coefficients are called shape or distortion coefficients. The achievement for each direction,  $l_2$  and  $l_3$ , is done by applying the principle of virtual works, so that the deformation work of the constant tangential stress coincides with the exact radius theory [14]. The resulting areas are called small cutting areas,  $A_2^*$  and  $A_3^*$ .

The coordinates of a point in the space of the element, in the normalized coordinates, is obtained by the Eq. (4.22).

$$\{x^g(s_1)\} = \sum_{k=1}^n N_k(s_1) \cdot \{x^g\}_k \quad \text{Eq. (4.22)}$$

where  $n$  is the number of elements;  $N_k(s_1)$  is a shape function of the node number  $k$ , valuated in the position of the normalized coordinate  $s_1$ ;  $\{x^g\}_k$  is the vector of global coordinates of  $k$ -th node. The Eq. (4.22) can be write in the matrix form.

$$\{x^g(s_1)\} = \begin{bmatrix} x_1^g \\ x_2^g \\ x_3^g \end{bmatrix} = [N_x(s_1)]\{X^g\} \quad \text{Eq. (4.23)}$$

where  $[N_x]$  is the matrix of the shape functions defined in Eq. (4.24).

$$[N_x] = \begin{bmatrix} N_1(s_1) & 0 & 0 & \cdots & N_n(s_1) & 0 & 0 \\ 0 & N_1(s_1) & 0 & \cdots & 0 & N_n(s_1) & 0 \\ 0 & 0 & N_1(s_1) & \cdots & 0 & 0 & N_n(s_1) \end{bmatrix} \quad \text{Eq. (4.24)}$$

and  $\{X^g\}$  is the vector of global coordinates of all the nodes of the element.

$$\{X^g\} = [x_{1G,1}^g \quad x_{2G,1}^g \quad x_{3G,1}^g \quad \cdots \quad x_{1G,n}^g \quad x_{2G,n}^g \quad x_{3G,n}^g]^T \quad \text{Eq. (4.25)}$$

Known the displacement of the element in the global reference system,  $\{U^g\}$ , it's possible to obtain the displacement of generic point of the element, in the normalized coordinates.

$$\{U^g(s_1)\} = \sum_{k=1}^n N_k(s_1) \cdot \{\bar{U}^g\}_k \quad \text{Eq. (4.26)}$$

where  $\{\bar{U}^g\}_k$  is the vector of displacement of  $k$ -th node. The Eq. (4.26) can be write in the matrix form.

$$\{U^g(s_1)\} = \begin{bmatrix} u_{1G}^g \\ u_{2G}^g \\ u_{3G}^g \\ \theta_1^g \\ \theta_2^g \\ \theta_3^g \end{bmatrix} = [N_u(s_1)]\{\bar{U}^g\} \quad \text{Eq. (4.27)}$$

where  $[N_u]$  is the matrix of the shape functions defined in Eq. (4.28).

$$[N_u] = \begin{bmatrix} N_1(s_1) & 0 & 0 & 0 & 0 & 0 & \cdots & N_n(s_1) & 0 & 0 & 0 & 0 & 0 \\ 0 & N_1(s_1) & 0 & 0 & 0 & 0 & \cdots & 0 & N_n(s_1) & 0 & 0 & 0 & 0 \\ 0 & 0 & N_1(s_1) & 0 & 0 & 0 & \cdots & 0 & 0 & N_n(s_1) & 0 & 0 & 0 \\ 0 & 0 & 0 & N_1(s_1) & 0 & 0 & \cdots & 0 & 0 & 0 & N_n(s_1) & 0 & 0 \\ 0 & 0 & 0 & 0 & N_1(s_1) & 0 & \cdots & 0 & 0 & 0 & 0 & N_n(s_1) & 0 \\ 0 & 0 & 0 & 0 & 0 & N_1(s_1) & \cdots & 0 & 0 & 0 & 0 & 0 & N_n(s_1) \end{bmatrix} \quad \text{Eq. (4.28)}$$

and  $\{\bar{U}^g\}$  is the vector of displacement of all the nodes of the element.

$$\{\bar{U}^g\} = [u_{1G,1}^g \quad u_{2G,1}^g \quad u_{3G,1}^g \quad \theta_{1,1}^g \quad \theta_{2,1}^g \quad \theta_{3,1}^g \quad \cdots \quad x_{1G,n}^g \quad x_{2G,n}^g \quad u_{3G,n}^g \quad \theta_{1,n}^g \quad \theta_{2,n}^g \quad \theta_{3,n}^g]^T \quad \text{Eq. (4.29)}$$

The strains at a point of the element, in the normalized coordinates  $s_1$ , can be obtained from the displacement of the nodes, by the Eq. (4.30).

$$\{\bar{\varepsilon}^l(s_1)\} = \sum_{k=1}^n [B_k(s_1)]\{U^l\}_k \quad \text{Eq. (4.30)}$$

where  $[B_k]$  is the strain matrix of  $k$ -th node, in the normalized coordinates;  $\{U^l\}_k$  is the vector of displacement of  $k$ -th node in the local coordinates. Considering the Eq. (4.10), the Eq. (4.30) can be write in the following matrix form.

$$\{\varepsilon^l(s_1)\} = \begin{bmatrix} \frac{\partial u_{1G}^l}{\partial x_1^l} \\ \frac{\partial u_{2G}^l}{\partial x_1^l} - \theta_3^l \\ \frac{\partial u_{3G}^l}{\partial x_1^l} + \theta_2^l \\ \frac{\partial \theta_1^l}{\partial x_1^l} \\ \frac{\partial \theta_2^l}{\partial x_1^l} \\ \frac{\partial \theta_3^l}{\partial x_1^l} \end{bmatrix} = [B(s_1)]\{\bar{U}^l\} = [B(s_1)][T^{lg}]\{\bar{U}^g\} = [\bar{B}(s_1)]\{\bar{U}^g\} \quad \text{Eq. (4.31)}$$

where  $[\bar{B}]$  is the strain matrix. This matrix, with the hypothesis that the barycentre coincides with the shear centre, is represented in the Eq. (4.33) [13].

$$[\bar{B}_k] = \begin{bmatrix} \frac{dN_k(s_1)}{dx_1^l} & 0 & 0 & 0 & 0 & 0 \\ 0 & \frac{dN_k(s_1)}{dx_1^l} & 0 & 0 & 0 & -N_k(s_1) \\ 0 & 0 & \frac{dN_k(s_1)}{dx_1^l} & 0 & N_k(s_1) & 0 \\ 0 & 0 & 0 & \frac{dN_k(s_1)}{dx_1^l} & 0 & 0 \\ 0 & 0 & 0 & 0 & \frac{dN_k(s_1)}{dx_1^l} & 0 \\ 0 & 0 & 0 & 0 & 0 & \frac{dN_k(s_1)}{dx_1^l} \end{bmatrix} \quad \text{Eq. (4.32)}$$

$$[\bar{B}] = \begin{bmatrix} \frac{dN_1(s_1)}{dx_1^l} & 0 & 0 & 0 & 0 & 0 & \dots & \frac{dN_n(s_1)}{dx_1^l} & 0 & 0 & 0 & 0 & 0 \\ 0 & \frac{dN_1(s_1)}{dx_1^l} & 0 & 0 & 0 & -N_1(s_1) & \dots & 0 & \frac{dN_n(s_1)}{dx_1^l} & 0 & 0 & 0 & -N_n(s_1) \\ 0 & 0 & \frac{dN_1(s_1)}{dx_1^l} & 0 & N_1(s_1) & 0 & \dots & 0 & 0 & \frac{dN_n(s_1)}{dx_1^l} & 0 & N_n(s_1) & 0 \\ 0 & 0 & 0 & \frac{dN_1(s_1)}{dx_1^l} & 0 & 0 & \dots & 0 & 0 & 0 & \frac{dN_n(s_1)}{dx_1^l} & 0 & 0 \\ 0 & 0 & 0 & 0 & \frac{dN_1(s_1)}{dx_1^l} & 0 & \dots & 0 & 0 & 0 & 0 & \frac{dN_n(s_1)}{dx_1^l} & 0 \\ 0 & 0 & 0 & 0 & 0 & \frac{dN_1(s_1)}{dx_1^l} & \dots & 0 & 0 & 0 & 0 & 0 & \frac{dN_n(s_1)}{dx_1^l} \end{bmatrix} \quad \text{Eq. (4.33)}$$

and  $\{\bar{U}^g\}$  is the vector of displacement of all nodes of the element defined in Eq. (4.29).

In order to evaluate the term  $\frac{dN_k(s_1)}{dx_1^l}$  of the matrix  $[\bar{B}]_k$  it's possible to adopt the Eq. (4.29) [13].

$$\frac{dN_k(s_1)}{dx_1^l} = \frac{dN_k(s_1)}{ds_1} \frac{ds_1}{dx_1^l} \quad \text{Eq. (4.34)}$$

where the term  $\frac{ds_1}{dx_1^l}$ , which is the jacobian respect to the normalized coordinates  $s_1$ , is calculated according to Eq. (4.35).

$$\frac{ds_1}{dx_1^l} = \left\{ \left[ \sum_{k=1}^n \frac{dN_k(s_1)}{ds_1} x_{1G,k}^g \right]^2 + \left[ \sum_{k=1}^n \frac{dN_k(s_1)}{ds_1} x_{2G,k}^g \right]^2 + \left[ \sum_{k=1}^n \frac{dN_k(s_1)}{ds_1} x_{3G,k}^g \right]^2 \right\}^{1/2} = J \quad \text{Eq. (4.35)}$$

Then, by replacing Eq. (4.35) into Eq. (4.34), the following equation is obtained.

$$\frac{dN_k(s_1)}{dx_1^l} = \frac{dN_k(s_1)}{ds_1} \frac{1}{J} \quad \text{Eq. (4.36)}$$

#### 4.1.2. Stiffness matrix

Considering a beam element of volume  $V$  subjected to generalized forces distributed along the volume,  $\{q_V^g\}$ , generalized forces distributed along the surface,  $\{q_S^g\}$ , and generalized forces applied to the nodal points of the structure,  $\{Q^g\}$ . The element is subjected to virtual strains and displacements,  $\delta\{\varepsilon\}$  and  $\delta\{U\}$ , therefore, applying the principle of virtual works, the internal work is equal to work given by external forces.

$$\delta W_{int} = \delta W_{ext} \quad \text{Eq. (4.37)}$$

The work given by the external forces is defined by Eq. (4.38).

$$\delta W_{ext} = \int_V \delta\{U^g\}^T \{q_V^g\} dV + \int_S \delta\{U^g\}^T \{q_S^g\} dS + \delta\{U^g\}^T \{Q^g\} \quad \text{Eq. (4.38)}$$

While, the work given by the internal forces is defined by Eq. (4.39).

$$\delta W_{int} = \int_V \delta\{\varepsilon^l\}^T \{\sigma^l\} dV + \int_V \delta\{u^g\}^T \rho \{\ddot{u}^g\} dV = \delta W_{i,st} + \delta W_{i,din} \quad \text{Eq. (4.39)}$$

The static part of the internal work is defined by Eq. (4.40).

$$\delta W_{i,st} = \int_V \delta\{\varepsilon^l\}^T \{\sigma^l\} dV = \int_V (\delta\varepsilon_1^l \sigma_1^l + \delta\gamma_{12}^l \tau_{12}^l + \delta\gamma_{13}^l \tau_{13}^l) dV \quad \text{Eq. (4.40)}$$

Taking into account the Eq. (4.11), Eq. (4.12), Eq. (4.17), is possible to obtain the following expression of the static internal work.

$$\begin{aligned} \delta W_{i,st} &= \int_V \delta\{\varepsilon^l\}^T \{\sigma^l\} dV = \int_V \delta\{\bar{\varepsilon}^l\}^T [R]^T [D] \{\varepsilon^l\} dV = \\ &= \int_L \delta\{\bar{\varepsilon}^l\}^T [R]^T [D] [R] \{\bar{\varepsilon}^l\} dL = \int_L \delta\{\bar{\varepsilon}^l\}^T [\bar{D}] \{\bar{\varepsilon}^l\} dL \end{aligned} \quad \text{Eq. (4.41)}$$

Considering the Eq. (4.33), The Eq. (4.41) could be modified in the Eq. (4.42).

$$\delta W_{i,st} = \int_L \delta\{\bar{\varepsilon}^l\}^T [\bar{D}] \{\bar{\varepsilon}^l\} dL = \int_L \delta\{\bar{U}^g\}^T [\bar{B}]^T [\bar{D}] [\bar{B}] \{\bar{U}^g\} dL \quad \text{Eq. (4.42)}$$

Converting the Eq. (4.42) in normalized coordinates, it results the following expression.

$$\delta W_{i,st} = \delta\{\bar{U}^g\}^T \left( \int_{-1}^{+1} [\bar{B}]^T [\bar{D}] [\bar{B}] J ds_1 \right) \{\bar{U}^g\} \quad \text{Eq. (4.43)}$$

where

$$[K] = \int_{-1}^{+1} [\bar{B}]^T [\bar{D}] [\bar{B}] J ds_1 \quad \text{Eq. (4.44)}$$

is the stiffness matrix of the element. Applying the numerical integration of Gauss-Legendre to calculation of the stiffness matrix [14] is obtained the Eq. (4.45).

$$[K] = \sum_{p=1}^{N_{s1}} ([\bar{B}]^T [\bar{D}] [\bar{B}] J)_{s_1^p} W_p \quad \text{Eq. (4.45)}$$

where  $N_{s1}$  is the number of the integration points in the direction  $s_1$ ;  $W_p$  is the weight associated with the integration point of coordinates  $s_1^p$ . In case of element with two or three nodes, the value of  $J$  is equal to half length of the element ( $J = L/2$ ).

### 4.1.3. Mass matrix

Considering a beam element of volume  $V$  subjected to generalized forces distributed along the volume,  $\{q_V^g\}$ , generalized forces distributed along the surface,  $\{q_S^g\}$ ,

and generalized forces applied to the nodal points of the structure,  $\{Q^g\}$ . The element is subjected to virtual strains and displacements,  $\delta\{\varepsilon\}$  and  $\delta\{U\}$ , therefore, applying the principle of virtual works, the internal work is equal to work given by external forces (Eq. (4.37)).

Starting from the internal work in Eq. (4.39), the dynamic component is defined by Eq. (4.46).

$$\delta W_{i,din} = \int_V \delta\{u^g\}^T \rho \{\ddot{u}^g\} dV \quad \text{Eq. (4.46)}$$

Taking into account the Eq. (4.7), Eq. (4.9), Eq. (4.10), Eq. (4.27), is possible to obtain the following expression of the dynamic internal work.

$$\begin{aligned} \delta W_{i,din} &= \int_V \delta\{u^g\}^T \rho \{\ddot{u}^g\} dV = \int_V \delta\{U^g\}^T [R]^T \rho [R] \{\ddot{U}^g\} dV = \\ &= \int_V \delta\{U^l\}^T [T^{lg}]^T [R]^T \rho [R] [T^{lg}] \{\ddot{U}^l\} dV \end{aligned} \quad \text{Eq. (4.47)}$$

The nodal displacement vector  $\{U^l\}$  remains constant along the volume of integration, therefore, the Eq. (4.47) can be written in the Eq. (4.48).

$$\begin{aligned} \delta W_{i,din} &= \delta\{U^l\}^T \int_V [N]^T [T^{lg}]^T [R]^T \rho [R] [T^{lg}] [N] dV \{\ddot{U}^l\} = \\ &= \delta\{U^l\}^T \int_L [N]^T [\tilde{m}] [N] dL \{\ddot{U}^l\} \end{aligned} \quad \text{Eq. (4.48)}$$

where  $[\tilde{m}]$  is the mass matrix of the section, defined by Eq. (4.49).

$$[\tilde{m}] = \int_A [T^{lg}]^T [R]^T \rho [R] [T^{lg}] dA \quad \text{Eq. (4.49a)}$$

$$[\tilde{m}] = \int_A \begin{bmatrix} 1 & 0 & 0 & 0 & x_3^l & -x_2^l \\ 0 & 1 & 0 & -x_3^l & 0 & 0 \\ 0 & 0 & 1 & x_2^l & 0 & 0 \\ 0 & -x_3^l & x_2^l & (x_3^l)^2 + (x_2^l)^2 & 0 & 0 \\ x_3^l & 0 & 0 & 0 & (x_3^l)^2 & -x_2^l x_3^l \\ -x_2^l & 0 & 0 & 0 & -x_2^l x_3^l & (x_2^l)^2 \end{bmatrix} \rho dA \quad \text{Eq. (4.49b)}$$

Solving the integral separately, it obtained the results in Eq. (4.50).

$$\int_A \rho dA = \rho A = m \quad \left[ \frac{kg}{m} \right] \quad \text{Eq. (4.50a)}$$

$$\int_A \rho x_3^l dA = S_{x_2} \quad \left[ \frac{kg \cdot m}{m} \right] \quad \text{Eq. (4.50b)}$$

$$\int_A \rho x_2^l dA = S_{x_3} \quad \left[ \frac{kg \cdot m}{m} \right] \quad \text{Eq. (4.50c)}$$

$$\int_A \rho [(x_3^l)^2 + (x_2^l)^2] dA = I_{x_1 x_1} \quad \left[ \frac{kg \cdot m^2}{m} \right] \quad \text{Eq. (4.50d)}$$

$$\int_A \rho (x_3^l)^2 dA = I_{x_2 x_2} \quad \left[ \frac{kg \cdot m^2}{m} \right] \quad \text{Eq. (4.50e)}$$

$$\int_A \rho (x_2^l)^2 dA = I_{x_3 x_3} \quad \left[ \frac{kg \cdot m^2}{m} \right] \quad \text{Eq. (4.50f)}$$

$$\int_A -\rho x_2^l x_3^l dA = I_{x_2 x_3} \quad \left[ \frac{kg \cdot m^2}{m} \right] \quad \text{Eq. (4.50g)}$$

Therefore, the mass matrix in the Eq. (4.49b) can be expressed as in Eq. (4.51).

$$[\tilde{m}^l] = \int_A [R]^T \rho [R] dA = \begin{bmatrix} m & 0 & 0 & 0 & S_{x_2}^l & -S_{x_3}^l \\ 0 & m & 0 & -S_{x_2}^l & 0 & 0 \\ 0 & 0 & m & S_{x_3}^l & 0 & 0 \\ 0 & -S_{x_2}^l & S_{x_3}^l & I_{x_1 x_1}^l & 0 & 0 \\ S_{x_2}^l & 0 & 0 & 0 & I_{x_2 x_2}^l & I_{x_2 x_3}^l \\ -S_{x_3}^l & 0 & 0 & 0 & I_{x_2 x_3}^l & I_{x_3 x_3}^l \end{bmatrix} \quad \text{Eq. (4.51)}$$

Converting in normalized coordinates, we obtain the Eq. (4.52).

$$\delta W_{i,din} = \delta \{U^l\}^T \left( \int_{-1}^{+1} [N]^T [\tilde{m}^l] [N] J ds_1 \right) \{\dot{U}^l\} \quad \text{Eq. (4.52)}$$

Therefore, the mass matrix of the element is defined by Eq. (4.53).

$$[M] = \int_{-1}^{+1} [N]^T [\tilde{m}^l] [N] J ds_1 \quad \text{Eq. (4.53)}$$

Applying Gauss-Legendre Numerical Integration to calculation of the mass matrix, the Eq. (4.53) become the following.

$$[M] = \sum_{p=1}^{N_{s1}} \{[N]^T [\tilde{m}^l] [N] J\}_{s_1^p} W_p \quad \text{Eq. (4.54)}$$

Considering that the element, in its thickness, is discretized in fibers, and applying Gauss-Legendre numerical integration, the mass sub-matrices are obtained according to the following expressions.

- The axial component;

$$[M]_a^b = \sum_{p=1}^{N_{s1}^a} \{N_a^T \tilde{m}_a^b N_a J\}_{s_1^p} W_p \quad \text{Eq. (4.55)}$$

where  $\tilde{m}_a^b$  is axial component of the mass sub-matrix of the section of integration point, Eq. (4.56).

$$\tilde{m}_a^b = \sum_{i=1}^{NG_{sect}} \rho_i^b A_{GP,i} \quad \text{Eq. (4.56)}$$

- The shear component;

$$[M]_c^b = \sum_{p=1}^{N_{s1}^c} \{[N]_c^T [\tilde{m}_c^b] [N]_c J\}_{s_1^p}^{(e)} W_p \quad \text{Eq. (4.57)}$$

where  $[\tilde{m}_c^b]$  is the shear component of the mass sub-matrix of the section of integration point, Eq. (4.58).

$$[\tilde{m}_c^b] = \sum_{i=1}^{NG_{sect}} \begin{bmatrix} \rho_i^b A_{GP,i} & 0 \\ 0 & \rho_i^b A_{GP,i} \end{bmatrix} \quad \text{Eq. (4.58)}$$

- The torsion component;

$$[M]_t^b = \sum_{p=1}^{N_{s_1}^t} \{N_t^T \tilde{m}_t^b N_t J\}_{s_1^p}^{(e)} W_p \quad \text{Eq. (4.59)}$$

where  $\tilde{m}_t^b$  is the torsion component of the mass sub-matrix of the section of integration point, Eq. (4.60).

$$\tilde{m}_t^b = \sum_{i=1}^{NG_{sect}} \rho_i^b [(x_{3,i}^l)^2 + (x_{2,i}^l)^2] A_{GP,i} \quad \text{Eq. (4.60)}$$

- The bending component;

$$[M]_f^b = \sum_{p=1}^{N_{s_1}^f} \{[N]_f^T [\tilde{m}_f^b] [N]_f J\}_{s_1^p}^{(e)} W_p \quad \text{Eq. (4.61)}$$

where  $[\tilde{m}_f^b]$  is the bending component of the mass sub-matrix of the section of integration point, Eq. (4.62).

$$[\tilde{m}_f^b] = \sum_{i=1}^{NG_{sect}} \begin{bmatrix} \rho_i^b (x_{3,i}^l)^2 A_{GP,i} & -\rho_i^b x_{3,i}^l x_{2,i}^l A_{GP,i} \\ -\rho_i^b x_{3,i}^l x_{2,i}^l A_{GP,i} & \rho_i^b (x_{2,i}^l)^2 A_{GP,i} \end{bmatrix} \quad \text{Eq. (4.62)}$$

- The interaction axial-bending component;

$$[M]_{af}^b = \sum_{p=1}^{N_{s_1}^{af}} \{N_a^T [\tilde{m}_{af}^b] [N]_f J\}_{s_1^p}^{(e)} W_p = [[M]_{fa}^{(e)}]^T \quad \text{Eq. (4.63)}$$

where  $[\tilde{m}_{af}^b]$  is the interaction axial-bending component of the mass sub-matrix of the section of integration point, Eq. (4.64).

$$[\tilde{m}_{af}^b] = \sum_{i=1}^{NG_{sect}} \begin{bmatrix} \rho_i^b x_{3,i}^l A_{GP,i} & -\rho_i^b x_{2,i}^l A_{GP,i} \end{bmatrix} \quad \text{Eq. (4.64)}$$

- The interaction shear-torsion component;

$$[M]_{ct}^b = \sum_{p=1}^{N_{s_1}^{ct}} \{[N]_c^T [\tilde{m}_{ct}^b] N_t\}^T J_{s_1}^{(e)} W_p = [[M]_{tc}^{(e)}]^T \quad \text{Eq. (4.65)}$$

where  $[\tilde{m}_{ct}^b]$  is the interaction shear-torsion component of the mass sub-matrix of the section of integration point, Eq. (4.66).

$$[\tilde{m}_{ct}^b] = \sum_{i=1}^{N_{G_{sect}}} \begin{bmatrix} -\rho_i^b x_{3,i}^l A_{GP,i} \\ \rho_i^b x_{2,i}^l A_{GP,i} \end{bmatrix} \quad \text{Eq. (4.66)}$$

#### 4.1.4. Nonlinear static analysis model

The behaviour of reinforced concrete elements is clearly non-linear. Not this one linearity results, fundamentally, from the fact that the constitutive laws of materials are nonlinear.

An element is discretized in a 3D Timoshenko beam with two nodes, with six degrees of freedom per node. Deformations and stresses are evaluated in the Gauss points through the constitutive laws of the materials of each finite element. Longitudinal reinforcement is also taken into consideration, being discretized by finite elements. The behaviour of the transverse reinforcement is governed by constitutive laws no linear.

The solution of the non-linear equilibrium system of equations was obtained through the application of the Newton-Raphson method [13].

Taking into account the division of the section into finite elements, the stiffness matrix is obtained unlike what is described in section 4.1.1.

When the response of the elements of a structure becomes nonlinear, stiffness begins depending on the state of deformation to which these elements are subject. The state of deformation in a section of a structural element can be different at each point, which also leads to different stress states. Since the constitutive laws of materials are non-linear, the contribution to the stiffness matrix of each section is different. The stiffness matrix obtained in this way is a tangent stiffness matrix.

The relationship between the stress state and the deformation state established in Eq. (4.12) is rewritten in incremental mode to analyse the nonlinear behaviour of material, as in Eq. (4.67).

$$[\Delta\sigma] = [D_T][\Delta\varepsilon] \quad \text{Eq. (4.67)}$$

where  $[D_T]$  is the tangent stiffness matrix.

The calculation of the stiffness matrix on each element is carried out using the following procedure (Figure 40):

- Evaluation of generalized displacements  $\{U\}$  in the integration points of each 3D element.
- Known generalized displacements in the nodes, calculation of deformations  $\{\varepsilon\}$  at the level of each Gauss point of the finite elements that discretizes the section;
- Calculation of the tangent stiffness matrix  $[D_T]$  at the level of each Gauss point of the section, taking into account the constitutive laws of the materials;
- Calculation of the stiffness matrix of the 3D element,  $[K_T]$ .

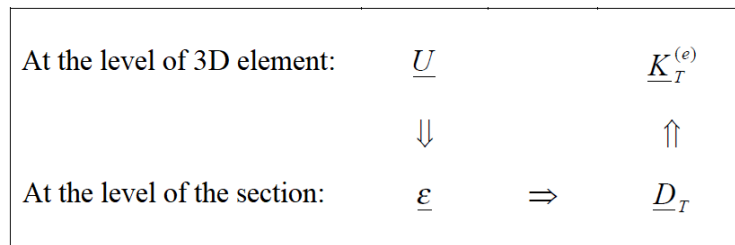


**Figure 40** - Scheme for obtaining the stiffness matrix of an element [13].

The evaluation process of the nodal forces equivalent to the stress state of the structure is identical to the calculation of the stiffness matrix.

To calculate these internal forces in each element, the following procedure is performed (Figure 41):

- Evaluation of generalized displacements  $\{U\}$  in the integration points of each 3D element.

- Known the generalized displacements in the nodes, calculation of deformations  $\{\varepsilon\}$  at the level of each Gauss point of the finite elements that discretizes the section;
- Calculation of the stresses  $\{\sigma\}$  at the Gauss point of each section, taking into account the constitutive laws of the intervening materials;
- Integration of tensions throughout the section to obtain efforts generalized respondent  $\{F\}$ ;
- Calculation of the internal forces of the 3D element,  $\{f_{int}\}$ .

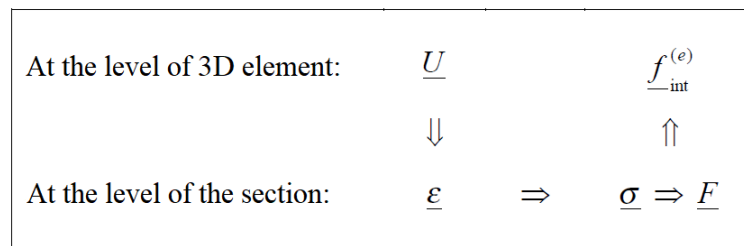


**Figure 41** – Scheme for obtaining the internal forces of an element [13].

## 4.2. Software for design the element

This chapter is dedicated to the presentation of the software used to simulate the behaviour of the slab element in fiber reinforced concrete (FRC) with 3D-SRT reinforcement subjected to the four-point bending tests.

To model the test, explained in chapter 3, the software called *Docros (Design Of CROSS Section)* and the program with finished elements *DefDocros* were used. For the design of this model, the guidelines described in chapter 2 were followed and the data obtained from the experimental tests described in chapter 3 were used.

The first software, *Docros*, uses the constitutive laws and the geometry of the section to derive the trend of internal stresses with the increase of internal deformations. The second one, *DefDocros*, takes the data concerning the section from *Docros* and with them, once the geometry of the beam and the boundary conditions have been set, it provides the displacement of each node for each increase of load.

A main feature of the software is the possibility to perform a comparative analysis between GFRP reinforcements and steel reinforcements of cross sections, to evaluate the different behaviour provided by the two materials.

#### 4.2.1. Analysis of cross-sections

An essential requirement of an analysis and design software is the development of a versatile calculation module to perform analysis of cross-sections. In the present section is presented the methodology adopted in *Docros* to conduct analysis of cross-sections submitted to bending with or without axial force. The main purpose of this software is to provide the section moment-curvature diagram.

The available cross-section geometry to be adopted is limited to rectangular shapes.

The input data that the software needs are the following:

- Geometry of the cross section.
- Constitutive law of the fiber reinforced concrete.
- Constitutive law of the GFRP bars.

The geometry of the cross-section considered is represented in Figure 42. The transverse and diagonal elements have been neglected as they do not offer bending resistance. Also the longitudinal bars in the top of the section are neglected, because the GFRP offer tensile strength only. In fact, the reinforcement is simulated as 8Ø5 at the bottom of the section.

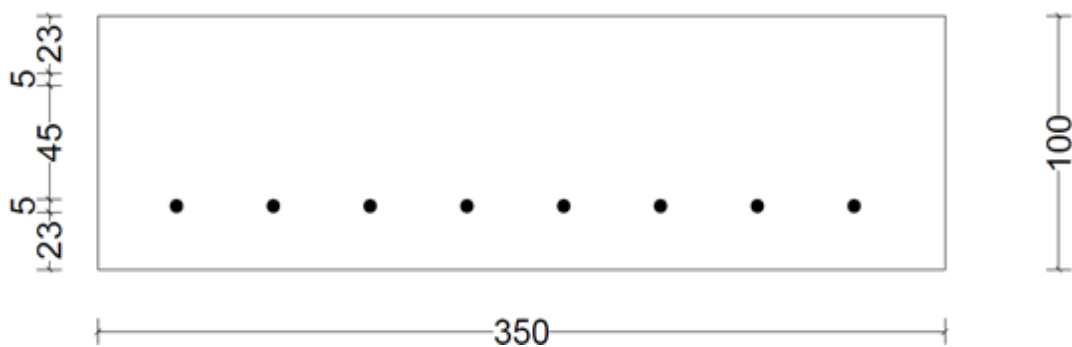


**Figure 42** – Simplified cross section of slab for analytic model (measure in mm).

In Table 12 is possible to see the values of the geometry property used for designing the cross-section.

**Table 12** - Values of the geometry property used for designing the cross-section of the slab.

Base of the cross-section	$B$	350 mm
Height of the cross-section	$H$	100 mm
Concrete cover	$c$	22.5 mm
Total tensile area of the reinforcement (8Ø5)	$A_s$	157 mm <sup>2</sup>

The constitutive law and the post-cracking behaviour of the fiber reinforced concrete are shown in Figure 43. The values necessary to model the constitutive law have been obtained from the experimental results. In particular, the data relating to the compression behaviour were obtained from the compression test described in chapter 3.2.1; the data relating to the post-cracking behaviour of the FRC were obtained following the guidelines described in chapter 2.2 and the results described in the section 3.3.3.

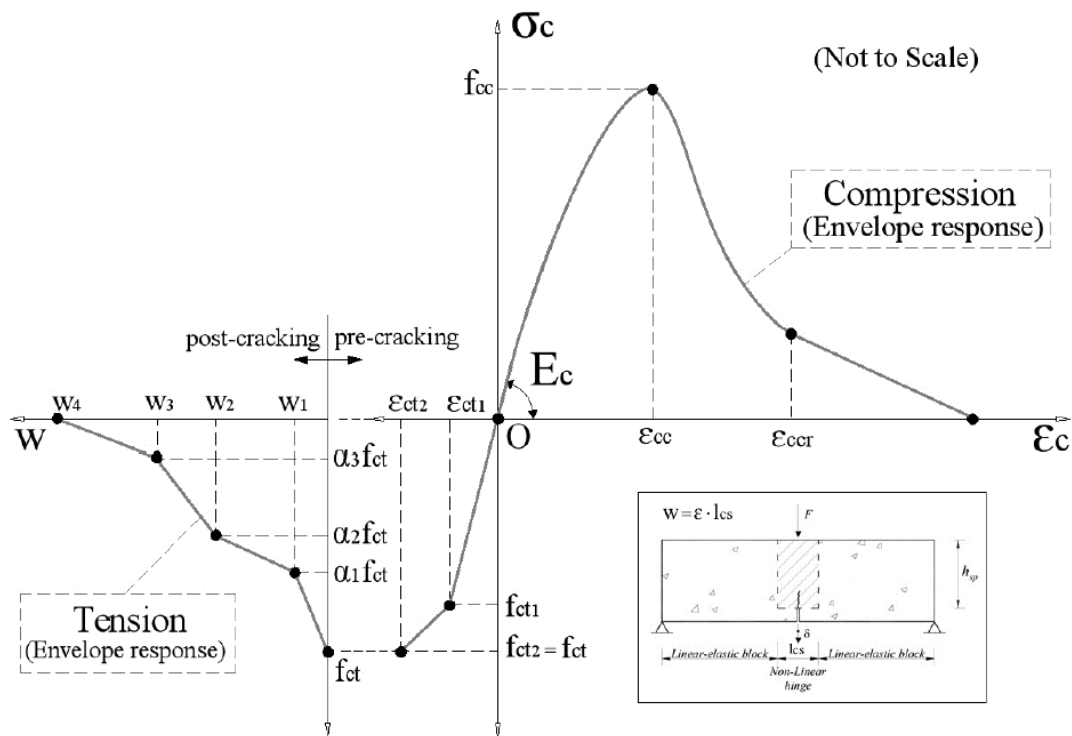


**Figure 43** – Model of the constitutive law and post-cracking behaviour of FRC.

In the following tables are shown the values utilized for realize the constitutive law of FRC. In particular in Table 13 the reference values for the compression behaviour are shown.

**Table 13** - Values for the compression behaviour of constitutive law of FRC.

Concrete initial Young's modulus	$E_c$	34870 <i>Mpa</i>
Concrete strain at compressive strength	$\varepsilon_{cc}$	2.7‰
Confined concrete compressive strength	$f_{cc}$	45.6 <i>Mpa</i>
Non-dimensional critical strain on the compression envelope	$\varepsilon_{ccr}$	2.9‰

After the value of non-dimensional critical strain on the compression envelope,  $\varepsilon_{ccr}$ , the law not collapse to 0, but continue linearly following the tangent at that point. In fact, this low value is to have a very low tangential value, to decay the curve slowly. This behaviour is justified by the fact that the reinforcement 3D-SRT creates an effect of confinement to the concrete.

Instead, in Table 14 the reference values for the tensile and post-cracking behaviour are instead shown.

**Table 14** - Values for the tensile and post-cracking behaviour of FRC.

Strain at the end of the 1st linear portion of the multilinear tensile envelope	$\varepsilon_{ct1}$	0.1‰
Stress at the end of the 1st linear portion of the multilinear tensile envelope	$f_{ct1}$	3,486 <i>Mpa</i>
Strain at the end of the 2nd linear portion of the multilinear tensile envelope	$\varepsilon_{ct2}$	0.15‰
Stress at the end of the 2nd linear portion of the multilinear tensile envelope	$f_{ct2}$	3,87 <i>Mpa</i>
Percentage of the tensile strength, for defining the 1st post-peak point	$\alpha_1$	0.93
1st post-peak point of the crack opening	$w_1$	0.01 <i>mm</i>
Percentage of the tensile strength, for defining the 2nd post-peak point	$\alpha_2$	0.69
2nd post-peak point of the crack opening	$w_2$	0.92 <i>mm</i>
Ultimate post-peak point of the crack opening	$w_4$	11.59 <i>mm</i>
Non-linear hinge length	$l_{cs}$	46.38 <i>mm</i>

The constitutive law of glass fiber reinforced polymer is linear elastic, as shown in Figure 44. The values necessary to model the constitutive law have been obtained from the experimental results, in particular, the data relating to the tensile behaviour were obtained from the tensile test described in chapter 3.2.2.

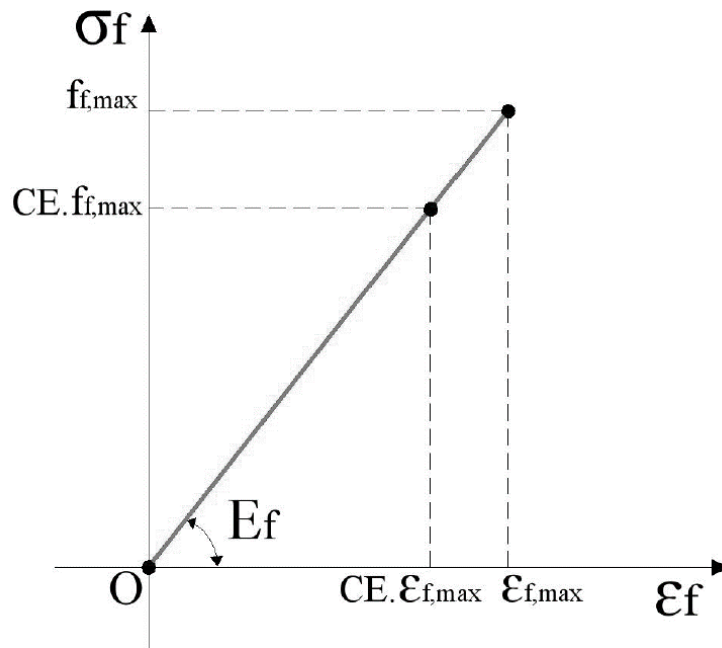


**Figure 44** – Model of the constitutive law of GFRP.

In the Table 15 are shown the values utilized for realize the constitutive law of GFRP.

**Table 15** - Values for the behaviour of GFRP.

Tensile strength	$f_{f,max}$	825.03 <i>Mpa</i>
Elasticity modulus	$E_f$	42520 <i>Mpa</i>
Rupture strain	$\epsilon_{f,max}$	1.94 %

All output data are presented in the form of a datasheet and graphs. It's possible to obtain the tension field in each layer the section; it's possible to obtain the graphics results of the trend of curvature, moment, neutral axis and crack width.

The main output data necessary for the analysis of the element are the following:

- The graphic trend of the top layer in compression, to view the maximum compression to which the concrete is subjected;
- The graphic trend of the GFRP bars in tension, to view their contribution within the section.
- The moment-curvature diagram. It's the most important, to see the maximum bending resistance the cross-section and to use its values as input data to be inserted in *DefDocros*.

#### 4.2.2. Analysis of the slab

In the present section is presented the methodology adopted in *DefDocros* to conduct analysis of a beam submitted to differ boundary conditions. The main purpose of this software is to provide the section load-deflection diagram to compare it with the results obtained experimentally.

The input data that the software needs are the following:

- The moment-curvature diagram of the cross-section of the element.
- The geometry of the beam and the boundary conditions.
- The increment of load in each step.

As described in the chapter 4.2.1, the curvature moment diagram is taken from the data obtained with *Docros*.

The slab is a simply supported beam as shown in Figure 45. For a greater accuracy of the results, the beams were divided into 57 nodes and 56 elements. Each element is 10 mm long except the two elements in the middle which are 5 mm long so as to have one node in the middle of the beam.

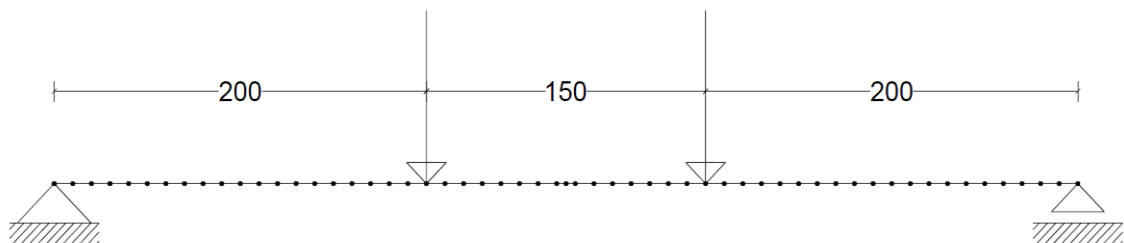


**Figure 45** – Static scheme of the beam subjected to 4PBT.

Once geometry and boundary conditions were set, a load increase of 1 kN was chosen for each force, therefore  $\Delta F = 2 \text{ kN}$  in total.

The procedure adopted by the finite element program for the evaluation of the displacement of the beam in each node is the following (Figure 46) [16]:

- Update the total load applied.
- Calculate the value of the moment in each node.

- Once the moment value is known, the tangential stiffness matrix can be obtained using the bending moment diagram.
- Obtained the tangential stiffness matrix it is possible to find the increase of displacement using the Eq. (4.68).

$$[\Delta u] = [K_T]^{-1}[\Delta F] \quad \text{Eq. (4.68)}$$

- Obtain the total displacement, adding the increase to the value of displacement of the previous step.

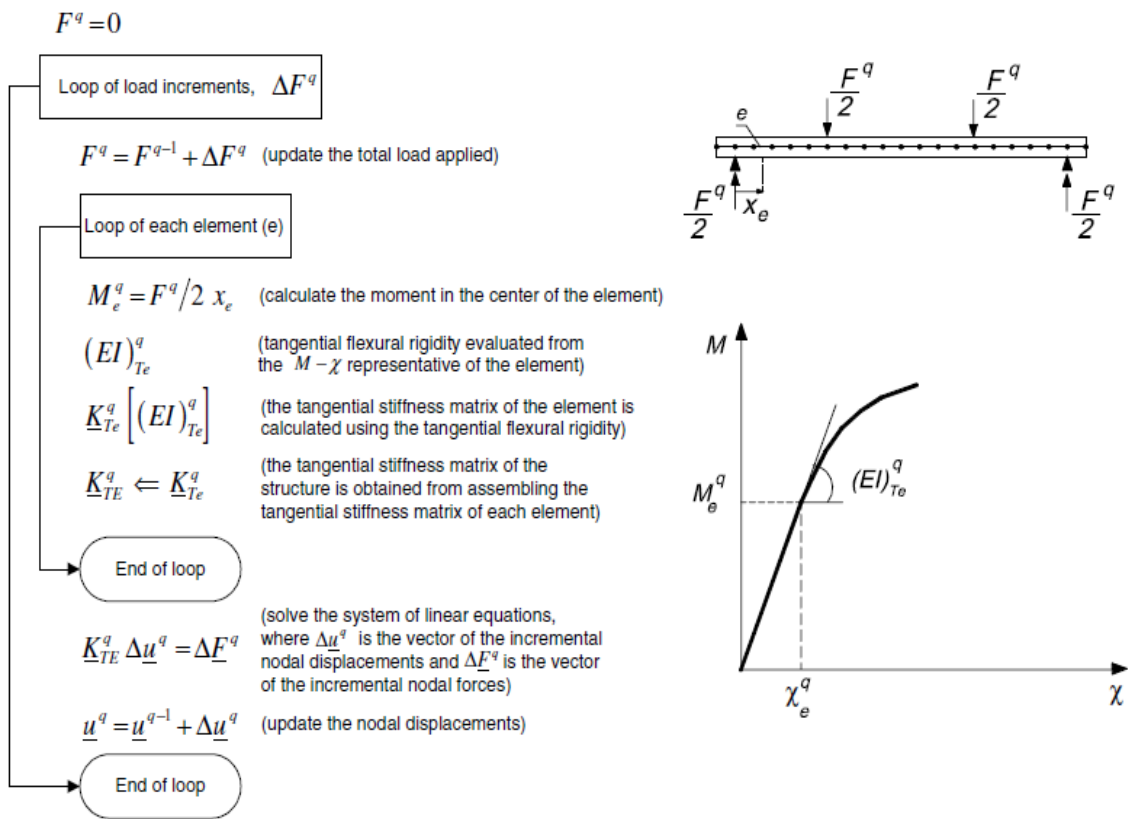


**Figure 46** - Numerical approach to simulate the deformational behaviour of structural elements. [16]

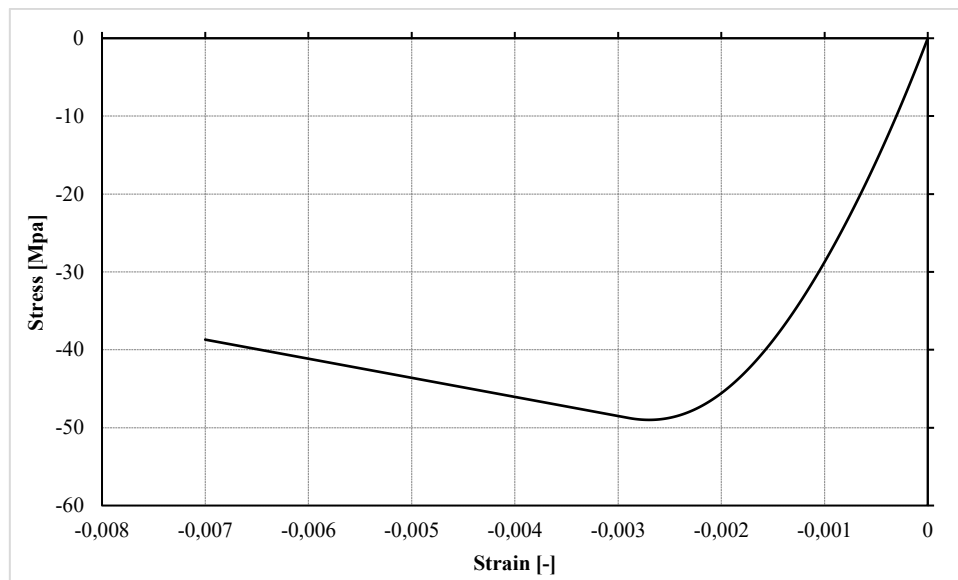
## 4.3. Numerical Simulation

### 4.3.1. Comparison between numerical model and experimental results

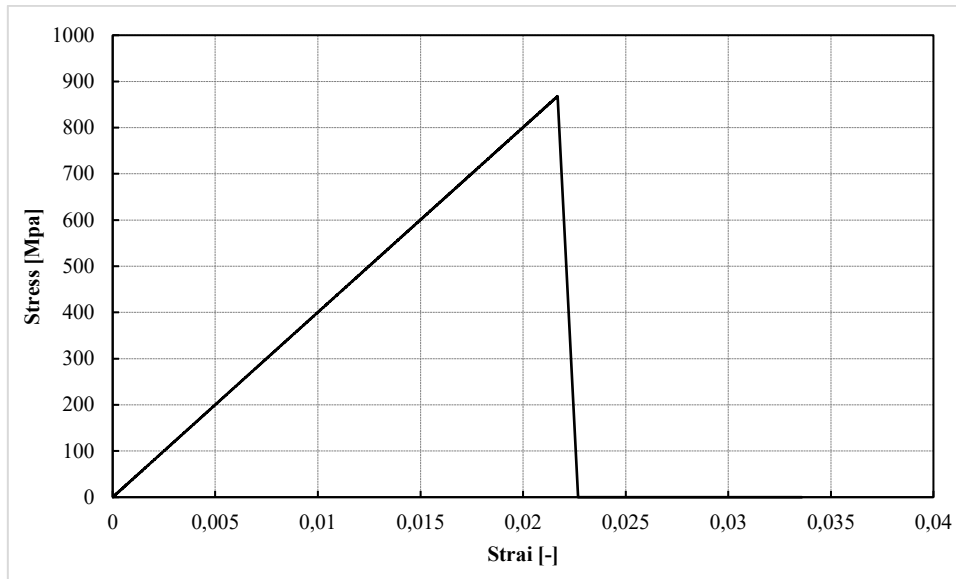
To calibrate and evaluate the performance of the developed model, the experimental tests performed and described in this chapter were simulated. Some nodes (numbers 11, 29 and 47) are positioned in the same place where the LVDTs are, so that the results obtained through the numerical model could be compared with the results obtained experimentally (Figure 22).

The results of the numerical simulation have been superimposed on the experimental results obtained in chapter 3.

To check if the numerical model works perfectly, the top layer in compression and the tension of the GFRP bars in the cross section were checked. The software is set to stop when the maximum compression deformation reaches 0.007. In Figure 47 and Figure 48 is possible to see the stress field of top layer and GFRP bars, respectively.

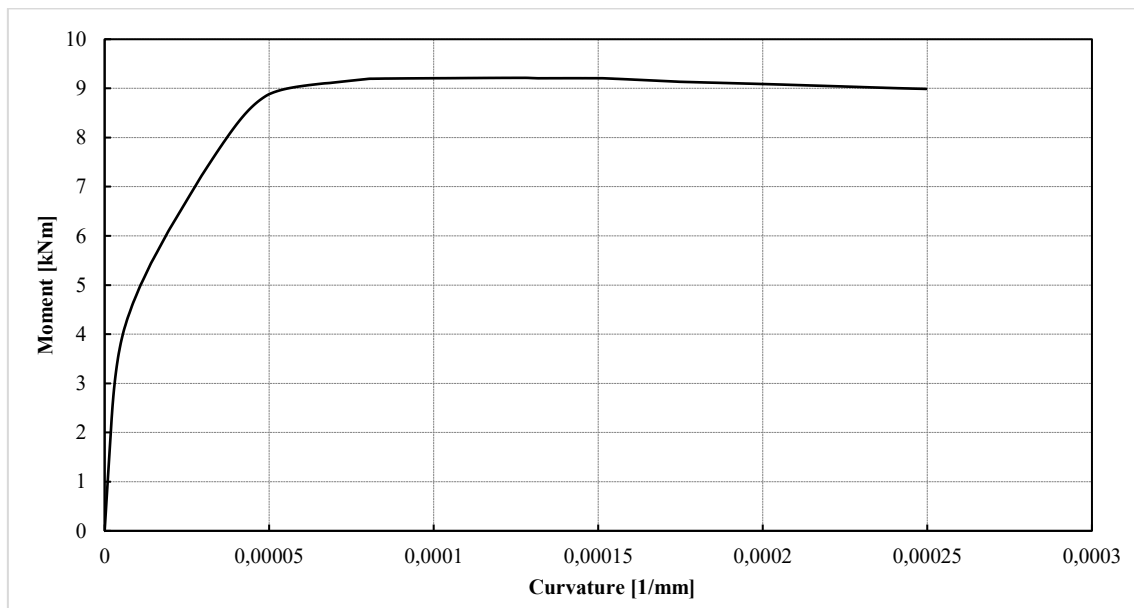


**Figure 47** – Numerical simulation of top layer of cross-section (compression negative).



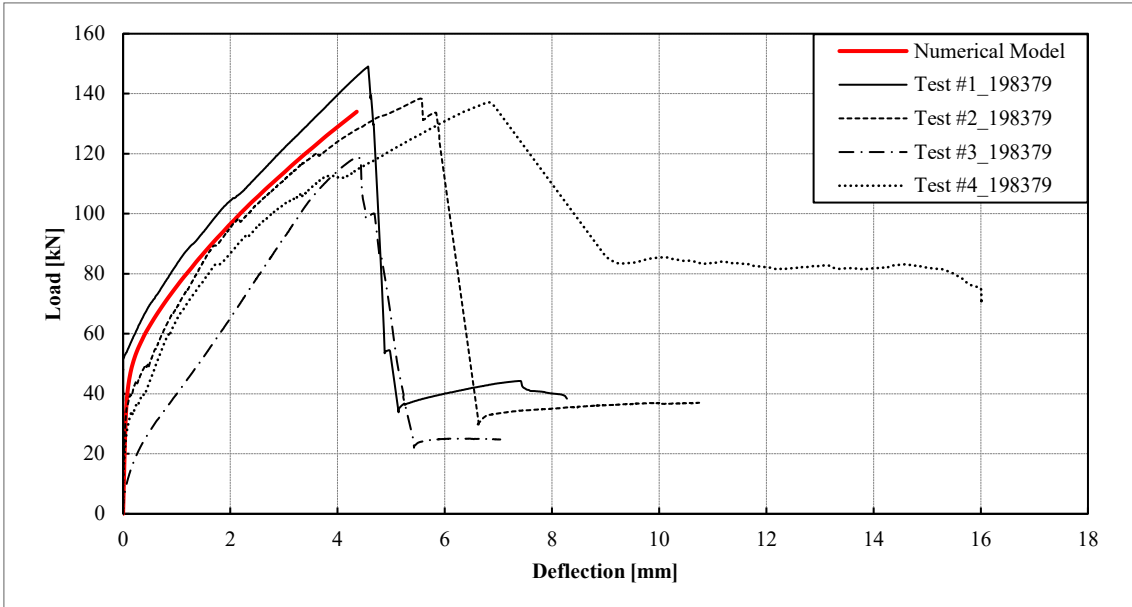
**Figure 48** - Numerical simulation of GFRP bars.

Figure 49 shows the moment of curvature diagram provided from the software.



**Figure 49** – Moment-Curvature diagram of the cross-section in the numerical model.

As described in the previous section, it is possible to obtain the load-deflection diagram. In the following figures the results of the numerical model are shown and compared with the results of the experimental test. Figure 50 refers to the half of the beam. While, Figure 51 and Figure 52 refer to LVDT 176621 and 19379 respectively.



**Figure 50** - Comparison of the numerical model with experimental results of the center beam.

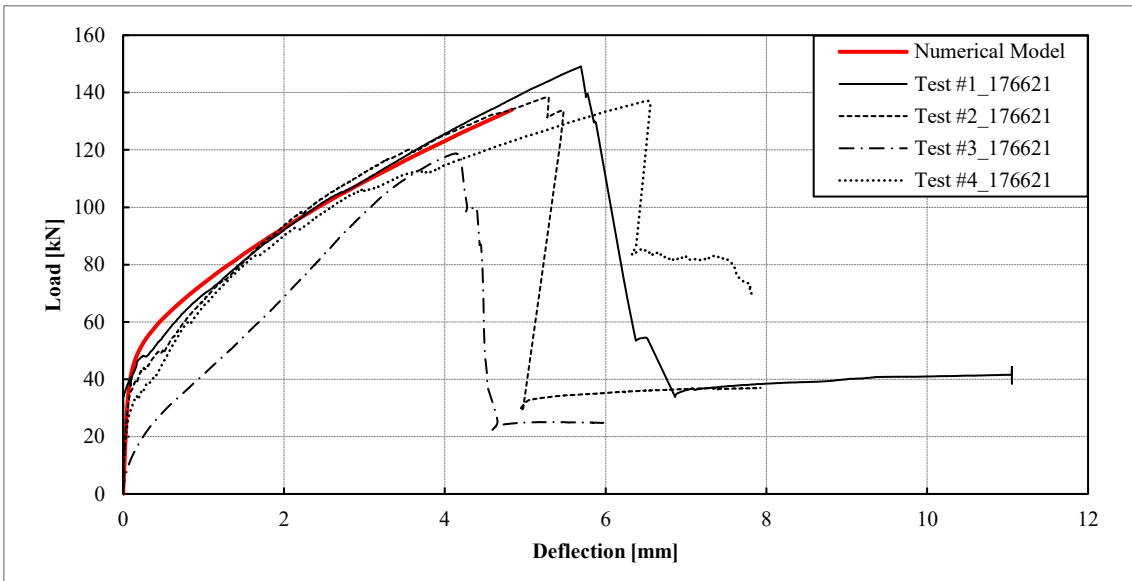


**Figure 51** - Comparison of the numerical model with experimental results of the LVDT 176621.

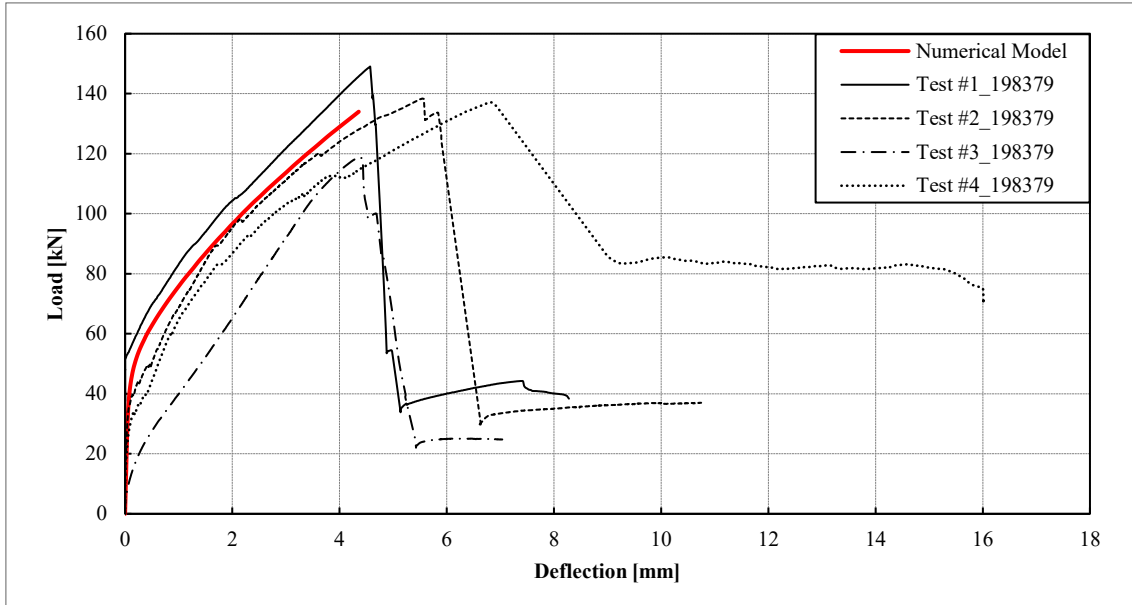


**Figure 52** - Comparison of the numerical model with experimental results of the LVDT 198379.

With these simulations, it was also intended to show the dependence of the various parameters that regulate the constitutive laws of materials, which means that their knowledge (and correct determination) is essential to simulate behaviour.

From this numerical simulation of the experimental tests, it can be verified that the model simulates the experimental response of the specimens quite rigorously.

In conclusion, it can be said that the model developed is a useful tool in analysis of materials with non-linear behaviour of beam elements. Even if only tests on fiber-reinforced concrete materials with GFRP reinforcement bars have been carried out and constitutive laws have been introduced to simulate this type of test, the proposed model is a versatile and generalist model. New constitutive laws can be easily introduced and therefore simulate, for example the behaviour of concrete elements or elements with metallic reinforcement.

### 4.3.2. Comparison between GFRP and steel reinforcement

Given the reliability of the numerical model, it was possible, by changing the constitutive law of the reinforcement, to create elements of fiber-reinforced concrete with steel bars.

Two different quantities of steel reinforcements were compared. The first element has approximately the same amount of tensile area,  $A_s$ , as the GFRP element described in chapter 4.3.1; the second one has the amount of area  $A_s$  necessary to obtain the same bending resistance as the GFRP bars.

In figure 53 the constitutive law adopted for the simulation of steel bars is shown. As can be seen, it is an elastic-plastic law with a first linear elastic response and then with a polyline that characterizes the plastic region.

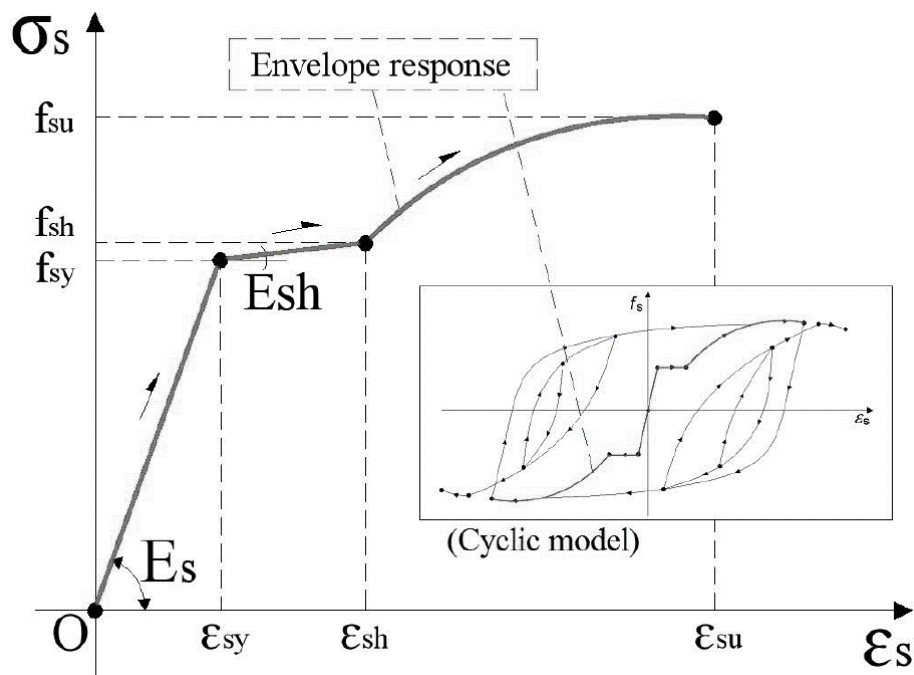


Figure 53 - Model of the constitutive law of steel.

The values used to represent the constitutive law of steel bars respect the parameters imposed by Eurocode 2 [7]. In the Table 16 are shown the values utilized for realize the constitutive law of steel bars.

**Table 16** - Values for the constitutive law of steel.

Elasticity modulus	$E_s$	210000 Mpa
Tangent modulus at strain hardening	$E_{sh}$	2500 Mpa
Yielding strain	$\varepsilon_{sy}$	2.38 ‰
Yielding stress	$f_{sy}$	500 Mpa
Hardening strain	$\varepsilon_{sh}$	10 ‰
Hardening stress	$f_{sh}$	519 Mpa
Strain at tensile strength	$\varepsilon_{su}$	5 ‰
Tensile strength	$f_{su}$	550 Mpa

The first case concerns the use of 5Ø6, in the second one 5Ø8 are used. Table 17 compares the tensile area of the model shown in Figure 42 and the area of the steel bars used for these models.

**Table 17** – Values of tensile area used for the numerical models.

<i>Reinforcement type</i>	<i>Quantity</i>	<i>Area</i>
<i>GFRP bars</i>	8Ø5	157 mm <sup>2</sup>
<i>First specimen with steel bars</i>	5Ø6	141 mm <sup>2</sup>
<i>Second specimen with steel bars</i>	5Ø8	251 mm <sup>2</sup>

Analysing the steel bar models with the software, we obtain the stress-strain diagrams shown in the figure 54.

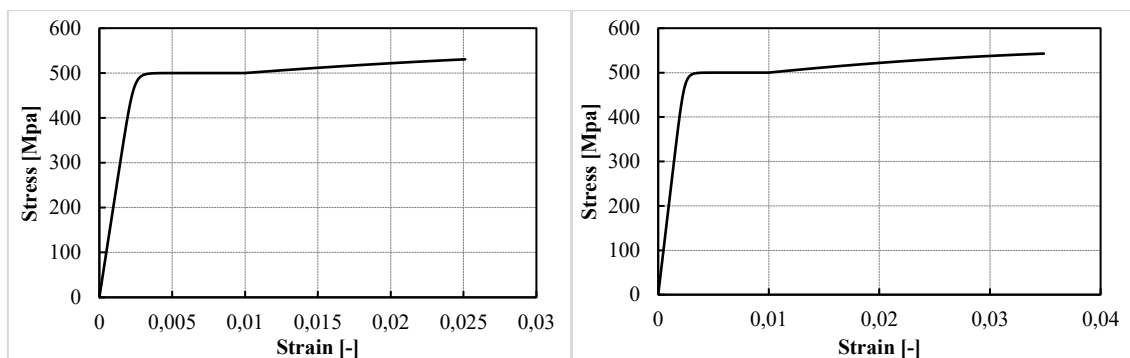
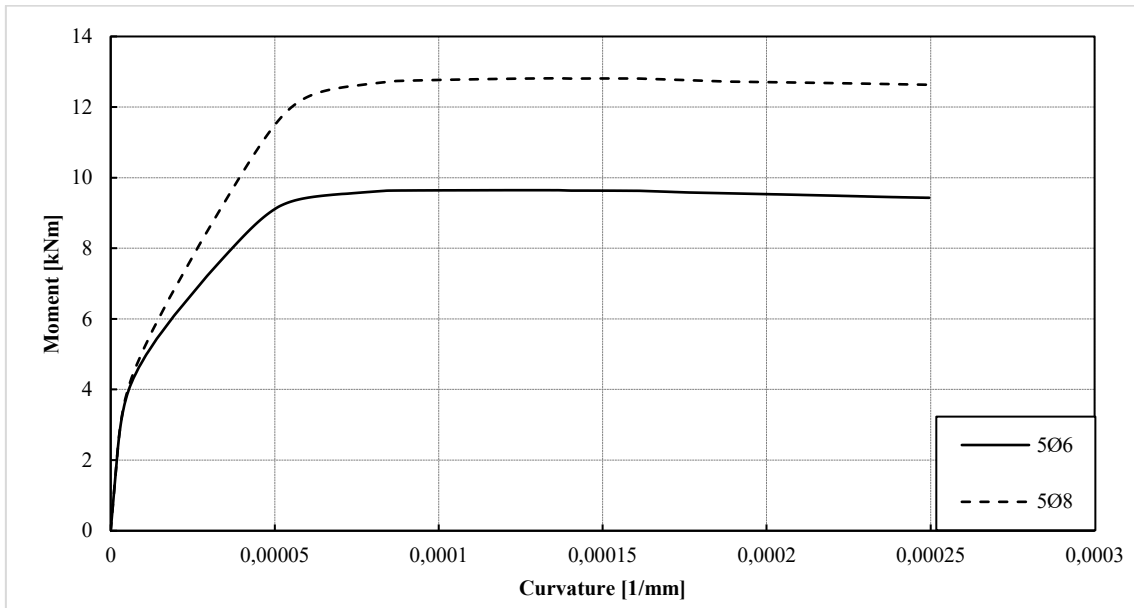


Figure 54 - Numerical simulation of steel bars: a) 5Ø6; b) 5Ø8.

In figures 55 the moment of curvature diagram of its specimens with steel reinforcement is shown.



**Figure 55** - Moment-Curvature diagram of the cross-section in the numerical model with steel bars.

Therefore, it is possible to obtain the load-deflection diagram. In the following figures the results of the numerical model are shown and compared with the results of the experimental test and the model that represent the specimen with 3D-SRT.

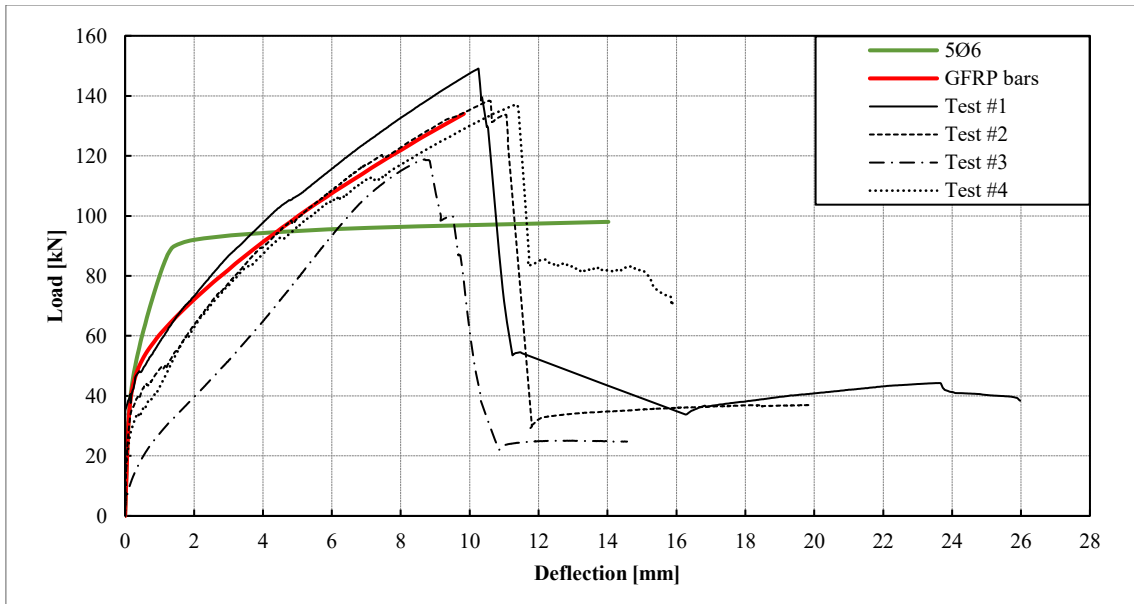


**Figure 56** - Comparison of the numerical models, GFRP bars and 5Ø6 steel reinforcement, with experimental results in the mid span of the beam.

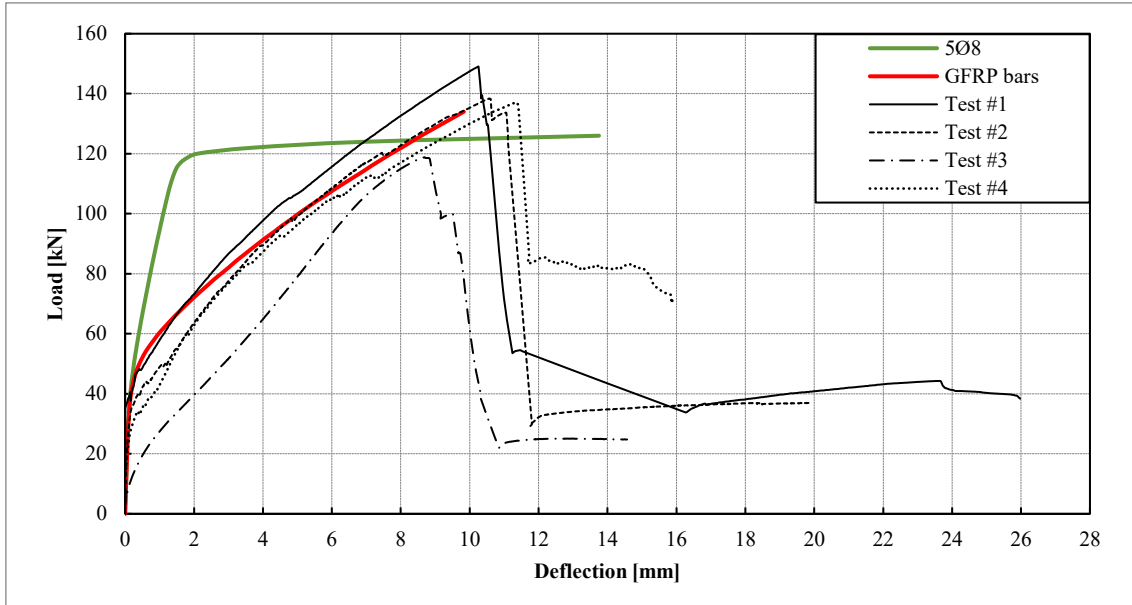


**Figure 57** - Comparison of the numerical models, GFRP bars and 5Ø8 steel reinforcement, with experimental results in the mid span of the beam.

From the results obtained, it can be seen that with the same quantity of tensile reinforcement, the GFRP bars offer greater resistance.

The behaviour of the bars in GFRP show better performance during the service limit states (SLS), guaranteeing the elastic behaviour under higher loads and displacements compared to elements with steel reinforcement.

A problem with GFRP bars is that they have a fragile collapse, which even if they compensate in part for the steel fibers in the concrete matrix, they require high safety coefficients at the ultimate limit states (ULS).

# Chapter 5

---

## 5. Conclusion

### 5.1. General Conclusion

The main goal of this study is to introduce a new generation material. A durable product for future buildings e constructions, made with FRC material reinforced with GFRP, in form of reinforcing bars or textile mesh for the construction of prefabricated elements.

During the experimental process, tests were carried out on the beam elements of fiber-reinforced concrete subject to bending. To characterize the materials were carried out uniaxial compression tests on cylindrical samples, bending tests under three load points with notched beams and tensile tests on GFRP bars.

The work developed was made up of an experimental component e by a numerical modelling component in which a code was developed computational for the simulation the behaviour of new generation material.

To simulate the non-linear behaviour of the material, a model based on the finite element method was developed. The model allows through constitutive laws appropriate of the intervening materials, to represent their nonlinear behaviour of the structures.

Comparing the numerical results with the results obtained experimentally, it is possible conclude that the developed model can evaluate the answer with good approximation of the tested beams.

## 5.2. Suggestions for future research

The work conducted in this thesis can be further developed, in fact, the following list of research topics is proposed:

- Evaluation of the bond behaviour between GFRP and FRC bars.
- Implement the analysis of shear behaviour of structures in FRC with 3D-SRT.
- Deeping in study and creation of numerical models that can evaluate the durability and resistance to chemical attacks of GFRP bars.
- Evaluation of the structural behaviour of prefabricated column elements in FRC with 3D-SRT
- Expansion of a 3D model, so that dynamic analysis can be performed.
- Assessment of the performance of frame type structures in FRC reinforced with 3D-SRT and steel bars with a static and dynamic analysis.
- Pushover analysis of frame type structures in FRC reinforced with 3D-SRT and steel bars.

# References

---

- [1] Soltanzadeh, F., J. A. O. Barros, and R. F. C. Santos, “*High performance fiber reinforced concrete for the shear reinforcement: Experimental and numerical research*”. *Construction and Building Materials*, 2015. **77**: pp. 94-109.
- [2] M. Brandt, “*Fibre reinforced cement-based (FRC) composites after over 40 years of development in building and civil engineering*”. *Compos. Struct.*, vol. 86, no. 1–3, pp. 3–9, Nov. 2008.
- [3] J. A. O. Barros, “*Comportamento do betão reforçado com fibras - análise experimental e simulação numérica /Behavior of fiber reinforced concrete - experimental and numerical analysis*”. PhD Thesis, Department of Civil Engineering, FEUP, Portugal, 1995.
- [4] J. A. O. Barros and J. Sena-Cruz, “*Fracture energy of steel fiber-reinforced concrete*”. *Mech. Compos. Mater. Struct.*, vol. 8, no. 1, pp. 29–45, 2001.
- [5] H. Mazaheripour, J. A. O. Barros, F. Soltanzadeh, and J. Sena-Cruz, “*Deflection and cracking behavior of SFRSCC beams reinforced with hybrid prestressed GFRP and steel reinforcements*”. *Eng. Struct.*, vol. 125, pp. 546–565, Oct. 2016.
- [6] T. D. S. Valente, J. A. O. Barros, and L. A. P. Lourenço, “*Advanced tools for design and analysis of fiber reinforced concrete structures*”. PhD Thesis, Department of Civil Engineering, University of Minho, Portugal, May 2019.
- [7] European Committee for Standardization, “*Eurocode 2: Design of concrete structures Part 1-1: General rules and rules for buildings*”, vol. NP EN 1992-1-1. 2010.
- [8] fib-federation internationale du beton, “*fib Model Code for Concrete Structures 2010*”. John Wiley & Sons, 2013.
- [9] M. di Prisco, G. Plizzari, and L. Vandewalle, “*Fibre reinforced concrete: new design perspectives*”. *Mater. Struct.*, vol. 42, no. 9, pp. 1261–1281, Nov. 2009.
- [10] European Committee for Standardization, “*Test method for metallic fibered concrete - Measuring the flexural tensile strength (limit of proportionality (LOP), residual)*”, vol. EN 14651. 2005.

- [11] M. Motavalli, C. Czaderski, A. Schumacher, D. Gsell, “*Fibre reinforced polymer composite materials for building and construction*”. Cambridge: Woodhead Publishing Limited; 2010. pp. 69-128.
- [12] RILEM TC 162-TDF, “*Recommendations of RILEM TC 162-TDF: Test and design methods for steel fibre reinforced concrete: bending test,*” Mater. Struct., vol. 35, no. 253, pp. 579–582, 2002.
- [13] Ventura Gouveia A., Barros J.A.O., “*Anàlise experimental e simulação numérica de elementos de barra de pórtico tridimensional de betão armado*”. Master thesis, University of Minho, 1999.
- [14] Barros, J.A.O., “*Modelos de análise de estruturas laminares e de compósitos laminados*”. Master thesis, University of Porto, 1989.
- [15] Oñate, E., “*Cálculo de estructuras por el metodo de elementos finitos. Análisis estático lineal*”, Centre Internaytonal of Numerics Methods in Engigneering, Setember 1995.
- [16] J.A.O. Barros, A.S. Fortes, “*Flexural strengthening of concrete beams with CFRP laminates bonded into slits*”. Cement & Concrete Composites, 2005. 27: pp. 471–480.